

THE DESIGN OF TWEEZER GENERATORS USING
MODIFIED CIRCULAR ADD-DROP MODULATOR

NARONGCHAI MOONGFANGKLANG

A THESIS SUBMITTED IN PARTIAL FULFILLMENT
OF THE REQUIREMENT FOR THE DEGREE OF
DOCTOR OF ENGINEERING IN ELECTRICAL ENGINEERING
FACULTY OF ENGINEERING
KING MONGKUT'S INSTITUTE OF TECHNOLOGY LADKRABANG

2014

KMITL-2014-EN-D-018-223

THE DESIGN OF TWEEZER GENERATORS USING
MODIFIED CIRCULAR ADD-DROP MODULATOR

NARONGCHAI MOONGFANGKLANG

A THESIS SUBMITTED IN PARTIAL FULFILLMENT
OF THE REQUIREMENT FOR THE DEGREE OF
DOCTOR OF ENGINEERING IN ELECTRICAL ENGINEERING
FACULTY OF ENGINEERING
KING MONGKUT'S INSTITUTE OF TECHNOLOGY LADKRABANG
2014
KMITL 2014-EN-D-018-223

COPYRIGHT 2014

FACULTY OF ENGINEERING

KING MONGKUT'S INSTITUTE OF TECHNOLOGY LADKRABANG

หัวข้อวิทยานิพนธ์	การออกแบบคิมจับแสงโดยใช้ตัวรวมสัญญาณวงแหวน ปรับแต่ง
นักศึกษา	นาย ณรงค์ชัย มุ่งแฝงกลาง
รหัสประจำตัว	49060057
ระดับการศึกษา	วิศวกรรมศาสตรดุษฎีบัณฑิต
สาขาวิชา	วิศวกรรมไฟฟ้า
พ.ศ.	2557
อาจารย์ที่ปรึกษาวิทยานิพนธ์	รศ. ดร. สมศักดิ์ มิตะถา

บทคัดย่อ

ในงานวิจัยนี้นำเสนอการออกแบบคิมจับเชิงแสงจำลองโดยใช้ตัวรวมสัญญาณวงแหวนรูปวงกลมปรับแต่งเพื่อยึดจับและอนุภาคด้วยอุปกรณ์ที่เรียกว่า “ตัวรวมสัญญาณวงแหวนรูปวงกลมปรับแต่ง (Modified Circular Add-Drop Modulator: MCADM)” จึงศึกษาฟังก์ชันการส่งผ่าน (Transfer Function) ของงานวิจัยเดิมและนำเสนอฟังก์ชันการส่งผ่านใหม่ที่ทำให้รูปสัญญาณใกล้เคียงกับความเป็นจริงมากขึ้น จากนั้นจะนำฟังก์ชันการส่งผ่านที่ได้มาทดลอง วิเคราะห์ผล เพื่อระบุค่าพารามิเตอร์ต่างๆ ที่เหมาะสมเพื่อออกแบบตัวรวมสัญญาณวงแหวนรูปวงกลมปรับแต่ง โดยยกตัวอย่างโจทย์เพื่อออกแบบตัวรวมสัญญาณคิมจับเชิงแสงจำลองที่สามารถนำพาอนุภาค 2 nm และมีความเร็วในการเคลื่อนที่ประมาณ 8 $\mu\text{m/s}$ ขั้นตอนถัดมาทำการออกแบบตัวรวมสัญญาณด้วยค่าพารามิเตอร์ต่างๆ ที่ระบุไว้แล้ว และทำการทดลองเพื่อยืนยันความสอดคล้องของผลที่ได้กับความต้องการของโจทย์ การวัดประสิทธิภาพจะประเมินจากผลลัพธ์ของการกำเนิดสัญญาณคิมจับเชิงแสงที่ออกจากตัวรวมสัญญาณซึ่งประกอบไปด้วยลักษณะของรูปคลื่นที่กำเนิดได้ (Wave form), ความลึกของรูปสัญญาณ (Depth of Well), ความกว้าง (Width of Well), แรงลัพธ์ (Net Force), ความจุของรูปสัญญาณ (Trapping Tools Capacity) และความเร็ว (Velocity) ที่ได้ โดยจะทำการเปรียบเทียบผลการทดลองที่ได้จากออกแบบตัวรวมสัญญาณวงแหวนรูปวงกลมปรับกับตัวรวมสัญญาณวงแหวนรูปสนามม้า (Racetrack Add-Drop Modulator: RADM) และตัวรวมสัญญาณวงแหวนรูปวงกลม (Circular Add-Drop Modulator: CADM) ซึ่งผลการทดลองที่ได้พบว่าการออกแบบตัวรวมสัญญาณที่นำเสนอมีประสิทธิภาพที่เหนือกว่าตัวรวมสัญญาณชนิดอื่น

Thesis Title	The Design of Tweezer Generators using Modified Circular Add-Drop Modulator
Student	Mr. Narongchai Moongfangklang
Student ID	49060057
Degree	Doctor of Engineering
Program	Electrical Engineering
Year	2014
Thesis Advisor	Assoc. Prof. Dr. Somsak Mitatha

ABSTRACT

This thesis proposes the design of tweezer generators using Modified Circular Add-Drop Modulator for particle trapping and manipulation. The transfer function of previous literature has been investigated and the new transfer function for describing the characteristics of tweezer is proposed. This transfer function is simulated, analyzed and optimized. Then the suitable parameters are specified. The design process starts with the constrained problem of 2 nm polystyrene is trapped and manipulated with the speed of $\approx 8 \mu\text{m/s}$. The next step is the design of tweezer and generator using MCADM based on the specified suitable parameters and then the test is undertaken to confirm the corresponding constrained problem. The performance is evaluated by studying tweezer signal properties including the output waveform, depth of well, width of well, net force, trapping tools capacity and velocity. In addition, these results are compared with Racetrack and Circular Add-Drop Modulators and the results demonstrate that our proposed design is more effective than other techniques.

ACKNOWLEDGEMENTS

บรรจกร้อยถ้อยถักสายอักษร	พนมกรบุญชูคุณอ่อนไพศาล
สามพระคุณหน่นนำมาเนิ่นนาน	ควรกราบกรานกตเวทีตา
น้อมประนมก้มกราบพระไตรรัตน์	อันจรัสทูนเทิดเหนือเกล้า
ปฏิบัติหลักประเสริฐเลิศปรัชญา	สูงส่งคุณธรรมค่าจิตใจ
กราบที่สรวงก้มลงตรงเบื้องบาท	อภิบาทพระคุณส่องงามพ่องไส
คุณพ่อแม่โอกาสประกาศไภล	พระยิ่งใหญ่จุดพลุสาฟ้าเคียงดิน
กราบที่สามไหว้ครูผู้ทรงศักดิ์	เป็นประจักษ์ความดีมีสิน
ท่านอบรมบ่มวิชาเป็นอาจิดน	ศิษย์ถวิลรำลึกนึกพระคุณ
ขอพระรัตนตรัยอันไพโรจน์	ปลื้มปราโมทย์จนใจคอยเกื้อหนุน
ให้ทุกท่านพร้งพร้อมในผลบุญ	เกียรติกลดลกายศปฺรากฎนาม

First of all, I would like to deeply thank Assoc. Prof. Dr. Somsak Mitatha, my Advisor and Chief of Hybrid Computing Research Laboratory (HCRL), Assoc. Prof. Preecha Yupapin a Chief of Advanced Research Center for Photonic Laboratory (ARCP) of King Mongkut's Institute of Technology Ladkrabang, and Prof. Dr. Kazuhiko Hamomoto of Tokai University, Japan my co-advisor, and Asst. Prof. Patcharee Muangnakin , for their helpful suggestions and constant supports during the whole work with this dissertation at King Mongkut's Institute of Technology Ladkrabang and Tokai University.

I am also thankful to my co-worker, Dr. Nathaporn Suwanpayak, Mr. Prateep Phatharacorn, Mr. Ratapol Siroroj, Mr. Chaiwat Sirawattananon, Mr. Wattanapong Suttapak, Mr. Sitti Rungtanom (RMUTT), Mr. Khanthanu Laungxaysana, Mr. Saysamon Soysouvanh and my dissertation committee for their insightful comments and helpful discussions which gave me a better perspective on my own results. I should also mention that my doctoral program in King Mongkut's Institute of Technology Ladkrabang and Tokai University was supported by Faculty Development Scholarships of Commission on Higher Education of Thailand with collaboration of AUN/Seed-Net. Finally, I would like to acknowledge the support of all of my beloved family and friends for all of their help.

Bangkok, Thailand

Narongchai Moongfangklang
December , 2014

CONTENTS

	Pages
บทคัดย่อ.....	I
ABSTRACT.....	II
ACKNOWLEDGEMENTS	III
CONTENTS.....	IV
LIST OF FIGURES.....	VII
LIST OF TABLES	XI
Chapter 1 Introduction	1
1.1 Motivation	1
1.2 Statement of Problem	2
1.3 Objectives.....	2
1.4 Contributions	2
1.5 Scope of Thesis.....	3
1.6 Organization	3
Chapter 2 Theoretical Background and Literature Reviews	5
2.1 Optical Tweezer Principle	5
2.2 Input Signals for Microparticle Trapping	9
2.3 Optical Modulation Techniques	12
2.4 Fabricated Microring Resonator Materials.....	13
2.5 Fabricated Microring Resonator sizes survey	13
2.6 Literature Reviews	14
2.7 Summary.....	38
Chapter 3 The Tweezer Generation using Modified Circular Add-Drop Modulator.....	39
3.1 The Studied Process of MCADM Design.....	39
3.2 The Proposed Mathematical Transfer Function	40
3.2.1 The Proposed Mathematical Transfer Function.....	40
3.3 Characteristics and Results Analysis of MCADM.....	45
3.3.1 Intensity Coupling Coefficient.....	45
3.3.2 Ring Radius Size	46
3.3.3 Fabricated Material.....	48
3.3.4 Center Wavelength.....	49

CONTENTS (Cont.)

	Pages
3.4 Constrained Problem and the Design of Tweezer and Generators using Modified Circular Add-Drop Modulator	50
3.4.1 Defining Constrain of Problem.....	51
3.4.2 The Design of Tweezer and Generators using Modified Circular Add-Drop Modulator.....	51
3.4.3 The Propose System	53
3.5 Summary.....	56
Chapter 4 Experimental Results and Discussion	57
4.1 The Primary Suitable Parameter Specification for RADM, CADM and MCADM Results.....	57
4.1.1 Racetrack Add-Drop Modulator (RADM)	59
4.1.2 Circular Add-Drop Modulator (CADM).....	67
4.1.3 Modified Circular Add-Drop Modulator (MCADM).....	75
4.1.4 The Suitable Parameters Specification for 3 Modulators	83
4.2 Experimental Results of the Proposed System.....	84
4.2.1 Intensity Coupling Coefficient.....	85
4.2.2 Materials	88
4.2.3 Ring Radius Size	90
4.2.4 Center Wavelength of Input Signal.....	93
4.2.5 Velocity.....	96
4.3 The Performance Comparison of 3 Modulators	96
4.3.1 Performance Comparison of Primary Suitable Parameters Specification	96
4.3.2 Discussion of Effected Parameters.....	103
4.3.3 Performance Comparison of Proposed and the Other System	104
4.4 Opti FDTD Simulation Results	105
4.4.1 Racetrack Add-Drop Modulator Simulation.....	106
4.4.2 Circular Add-Drop Modulator Simulation.....	107
4.4.3 Modified Circular Add-Drop Modulation Simulation	109
4.5 Sumarry of the Published Works [61, 62] and Thire Contribution to This Thesis	110
4.6 Summary.....	111

CONTENTS (Cont.)

	Pages
Chapter 5 Conclusion and Future Work.....	112
5.1 Conclusion.....	112
5.2 Future Work	113
REFERENCES.....	114
BIOGRAPHY.....	120

LIST OF FIGURES

Figures	Pages
2.1 The optical or optical tweezer generation [1].....	6
2.2 The molecular trapping mechanism, (a) Single-beam optical trapping force, (b) Doual-beam optical trapping force [17].....	6
2.3 The molecular properties	7
2.4 The optical tweezer properties	9
2.5 Two-dimensional intensity profile of a Gaussian beam	10
2.6 The geometric Bright Soliton.....	11
2.7 Four microring resonator and modulator devices [13-16].....	14
2.8 SEM image and transmission spectra of microring resonator, (a) SEM image of microring with radii of 5 μm , (b) SEM image of microring with radii of 10 μm , (c) Transmission spectra of ring radii of 5 μm , (d) Transmission spectra of ring radii of 10 μm [15].	15
2.9 The longitudinal of optical force and velocity, (a) Measurement velocity and optical force as a function of input power, (b) Transmission spectra of the microring resonator near a TM resonance mode and the cycling velocity of polystyrene beads [15].	16
2.10 The physical geometry of CADM [14].	16
2.11 The output characteristic signal at throughput and drop ports of CADM [14].....	16
2.12 The schematic model of CADM [14].	17
2.13 The physical geometry of RADM [15].	18
2.14 The schematic of optical manipulation of particle on RADM, (a) Schematic of optical manipulation of particle on RADM, (b) Optical micrograph of the optofluidic device [15].	19
2.15 The output at throughput and drop ports of RADM and optical micrograph of device with microparticle positions (a) Measured throughput and drop ports transmission spectra of device II (b) Optical micrograph of the device with particle positions (c) 0, (d) 50, (e) 60, (f) 187, (g) 254 and (h) 276 [15].....	19
2.16 The physical geometry of MCADM [16].	
2.17 Simulation results for Dark-Gaussian input, where $R_d=10 \mu\text{m}$, $R_R = R_L = 5 \mu\text{m}$, and the coupling coefficients of the ring resonator are $\kappa_1=0.5$, $\kappa_2=0.1$, $\kappa_3=0.35$, $\kappa_4=0.1$ [16].	21

LIST OF FIGURES (Cont.)

Figures	Pages
2.18 Simulation results for Dark-Gaussian input, where $R_d=10\ \mu\text{m}$, $R_R = R_L = 2\ \mu\text{m}$, and the coupling coefficients of the ring resonator are $\kappa_1=0.5$, $\kappa_2=0.1$, $\kappa_3=0.35$, $\kappa_4=0.1$ [16].	22
2.19 Physical geometry of a molecular buffer system (a) a PANDA ring resonator, (b) a wavelength router [43].	22
3.1 Attenuation versus wavelength and transmission windows [57]	49
3.2 The physical geometry of MCADM	52
3.3 The waveguide structure	53
3.4 The overview of system	53
3.5 The primary parameters specification system of RADM	54
3.6 The primary parameters specification system of CADM	55
3.7 The proposed system	56
4.1 The physical geometry of RADM	59
4.2 The comparison of the intensity coupling coefficient variations, when κ_1	60
4.3 The comparison of the intensity coupling coefficient variations when κ_1 and κ_2 are different of RADM	61
4.4 The comparison of fabricated materials effects of RADM	62
4.5 The comparison of add-drop ring radius effects of RADM	64
4.6 The comparison of wavelength effects of RADM	65
4.7 The comparison of velocity respect to the wavelength of RADM	67
4.8 The physical geometry of CADM	67
4.9 The comparison of the intensity coupling coefficient variations when κ_1 equal to κ_1 of CADM	69
4.10 The comparison of the intensity coupling coefficient variations when κ_1 and κ_1 are different of CADM	69
4.11 The comparison of fabricated material effects of CADM	71
4.12 The comparison of different add-drop ring radii of CADM	72
4.13 The comparison of t wavelength effects of CADM	74
4.14 The comparison of velocity with respect to the wavelength of CADM	75
4.15 The physical geometry of MCADM	76

LIST OF FIGURES (Cont.)

Figures	Pages
4.16 The comparison of the intensity coupling coefficient variations when κ_1 equals to κ_3 of MCADM.....	77
4.17 The comparison of the intensity coupling coefficient variations when κ_1 and κ_3 are different of MCADM	78
4.18 The comparison of fabricated material effects of MCADM	79
4.19 The comparison of different micro ring radii of MCADM	80
4.20 The comparison of t wavelength effects of MCADM	82
4.21 The comparison of velocity with respect to the wavelength of MCADM	83
Figure 4.22 The physical geometry of the proposed system	85
4.23 The comparison of the intensity coupling coefficient effects of RADM.....	86
4.24 The comparison of the intensity coupling coefficient effects of CADM	86
4.25 The comparison of the intensity coupling coefficient effects of MCADM.....	87
4.26 The comparison of the intensity coupling coefficient effects of 3 modulators ...	87
4.27 The comparison of the fabricated materials effects of RADM	88
4.28 The comparison of the fabricated materials effects of RADM	89
4.29 The comparison of the fabricated materials effects of RADM	90
4.30 The comparison of the fabricated materials effects of 3 modulators	90
4.31 The comparison of ring radius effects of RADM.....	91
4.32 The comparison of the ring radius effects of CADM	92
4.33 The comparison of the ring radius effects of MCADM.....	92
4.34 The comparison of the ring radius effects of 3 modulators	93
4.35 The comparison of the center wavelength of input signal effects of RADM.....	94
4.36 The comparison of the center wavelength of input signal effects of CADM.....	94
4.37 The comparison of the center wavelength of input signal effects of MCADM	95
4.38 The comparison of the center wavelength of input signal effects of 3 modulators.....	95
4.39 The velocity comparison between 3 modulators	96
4.40 The intensity coupling coefficients effects on depth of well.....	97
4.41 The intensity coupling coefficients effects on width of well.....	97
4.42 The intensity coupling coefficients effects on FSR.....	97

LIST OF FIGURES (Cont.)

Figures	Pages
4.43 The intensity coupling coefficients effects on velocity.....	98
4.44 The fabricated material effects on depth of well.....	98
4.45 The fabricated material effects on width of well.....	99
4.46 The fabricated material effects on FSR.....	99
4.47 The fabricated material effects on velocity.....	99
4.48 The ring radius sizes effects on depth of well.....	100
4.49 The ring radius sizes effects on width of well.....	100
4.50 The ring radius sizes effects on FSR.....	100
4.51 The ring radius sizes effects on velocity.....	101
4.52 The center wavelength of input signal effects on depth of well.....	101
4.53 The center wavelength of input signal effects on width of well.....	102
4.54 The center wavelength of input signal effects on FSR.....	102
4.55 The center wavelength of input signal effects on velocity.....	102
4.56 The compared parameters variations of 3 modulators.....	104
4.57 The Racetrack Add-Drop Modulator model.....	106
4.58 The output of electrical field at throughput port.....	106
4.59 The output of electrical field at throughput port using Matlab.....	106
4.60 The output of electrical field at drop port.....	107
4.61 The Circular Add-Drop Modulator model.....	107
4.62 The output of electrical field at throughput port.....	108
4.63 The output of electrical field at throughput port from Matlab.....	108
4.64 The output of electrical field at drop port.....	108
4.65 The Modified Circular Add-Drop Modulator model.....	109
4.66 The output of electrical field at throughput port.....	109
4.67 The output of electrical field at throughput port from Matlab.....	109
4.68 The output of electrical field at drop port.....	110

LIST OF TABLES

Tables	Pages
2.1 The properties of waveguide materials	13
2.2 The properties of waveguide materials	14
2.3 The measurement velocity of particle positions	19
2.4 The summary of other references	24
2.5 Compare the different functional	38
3.1 The effects of the intensity coupling coefficients on optical tweezer signal	46
3.2 The effects of the ring radius size on optical tweezer signal	47
3.3 The effects of the fabricated materials on optical tweezer signal	48
3.4 The effects of the input center wavelength on optical tweezer signal	49
3.5 The suitable parameter specification for MCADM in order to generate optical tweezer signals for polystyrene 2 nm and velocity $\approx 8 \mu\text{m/s}$	52
4.1 The parameters for primary suitable specification of 3 modulators simulation	58
4.2 The effects of the intensity coupling coefficient on optical output signal	61
4.3 The effects of fabricated materials on optical output signal	63
4.4 The effects of ring radius size on optical output signal	64
4.5 The effects of input center wavelength variation on output signal	66
4.6 The effects of the intensity coupling coefficient on optical output signal	70
4.7 The effects of fabricated materials on optical output signal	71
4.8 The effects of ring radius sizes on optical output signal	73
4.9 The effects of input center wavelength variation on optical output signal	74
4.10 The effects of the intensity coupling coefficient on the optical output signal	78
4.11 The effects of fabricated materials on optical output signal	79
4.12 The effects of ring radius size variations on optical output signal	81
4.13 The effects of the input center wavelength variations on optical output signal	82
4.14 The suitable parameters of 3 modulators	83
4.15 The parameter simulation of MCADM	84
4.16 The comparison of the center wavelength of input signal effects of 3 modulator devices	95
4.17 The comparison of primary suitable parameter specifications	103
4.18 The comparison of three modulators performance	105

Chapter 1

Introduction

1.1 Motivation

Nowadays, the optical tweezer has become a powerful tool for many application aspects such as biological [1], biophysics [2] and medical fields[3-4]. After optical tweezer was pioneered by Arthur Ashkin in 1970, the biologists used the optical tweezer as a tool for several purposes such as measuring the compliance of bacterial tails [5], the forces exerted by single motor proteins [6] and the stretching of single deoxyribonucleic acid (DNA) molecules [7]. Biophysics application includes measurement interaction of proteins [2], distinct membrane mechanical properties of human mesenchymal stem cells [8]. For the medical applications, optical tweezer is a very important tool for intracellular surgery [9-10], vitro fertilization [11-12], and targeted drug delivery system [3-4].

By the wide range of optical tweezer applications, the motivation of thesis originates from the literature of Shiyun Lin and his colleagues [13] which a silicon microring resonator is used to trap the 1.1 μm of polystyrene. The experimental output shows that the polystyrene particle is propelled around the microring resonator at hundreds micrometers per second. The second motivation literature is a Circular Add-Drop Modulator (CADM) of Dominik G. Rabus [14] which demonstrates the structure and the mathematical transfer function for describing the output of signal at throughput and drop ports of the modulator. The next motivation is the literature of Hong Cai and Andrew W. Poon [15] which uses Racetrack Add-Drop Modulator (CADM) in an integrated optofluidic chip for trap the 1 μm of polystyrene around its circumference. The velocity at on-off resonance of this research is evaluated by the cooperation of CCD camera for the capture particle position. The final literature is the optical vortices generated by Modified Circular Add-Drop Modulator (MCADM) or PANDA ring resonator proposes by Nattaporn Suwanpayak and her colleagues [16]. The experimental output shows that feeding the input signal is Gaussian and Dark Soliton to the input and the drop port of MCADM respectively. The modulator can generate the optical tweezer signal for molecular trapping and manipulation. The final review shows that there are some errors in mathematical transfer function [16] which affects the output signal. Therefore, this thesis focuses on the optical tweezer generation by MCADM for realistic output signal for molecular trapping and manipulation.

1.2 Statement of Problem

Although a variety of research [13-16] has reported on microring resonator applications, there is little information available on suitable parameters of microring modulators in order to generate tweezer signal for trapping tool manipulation. There are some errors in mathematical transfer function of previous research [16] which affects the output signal. Therefore, the improvement of realistic output signal for molecular trapping and manipulation is a necessity. For this thesis, the suitable parameter values are studied and investigated for molecular trapping and manipulation. After the process of suitable parameters value determination, those parameters are applied for finding velocity. The performance of this device is evaluated and compared with Racetrack Add-Drop Modulator (RADM) and Circular Add-Drop Modulator (CADM) using the output waveform, depth of well, width of well, net force, trapping tools capacity and velocity. In addition, this thesis proposes the design example of optical tweezer for molecular trapping and manipulation.

1.3 Objectives

1. Study and analyze the suitable parameters of microring modulators.
2. Simulate microring modulator system to specify the suitable parameters of tweezer generation for trapping tool applications.
3. Propose the design of optical tweezer generation for molecular trapping and manipulation.
4. Compare trapping tool performance of three type microring modulator.

1.4 Contributions

Normally, the optical tweezer can be generated by a laser that is strongly focused through lens with a very short focal length (most often a high numerical aperture [NA] microscope objective) in order to increase its intensity. Every photon of light with high intensity carries energy $h\nu$ (J) and momentum h/λ (kg.m/s), and it is straightforward to state that if the photon of light is absorbed by an object, the momentum will transfer from a light beam of power P (mW), lead to a reaction force F (pN) on the particle or molecular. The optical radiation pressure force is divided into scattering (F_{scatt}) and gradient forces (F_{grad}). The scattering force is the percussion result of photon and particle which is in the same direction with the incident of laser light. The gradient force is originated by a difference in pressure across a surface and the direction is perpendicular to the incident laser light. The stability of optical trapping or optical tweezer is occurring under the criterion of the gradient force which is higher than scattering force and the particle or molecule can

be manipulated by the condition of the net force (F_{net}) is greater than viscosity (F_{vis}) or friction force (F_{fric}). This thesis proposed the design of tweezer and generators using MCADM for particle trapping and manipulation. In the experiment, the laser light input signal is modeled by Gaussian signal and Dark Soliton signal. These signals are fed to the proposed systems at input and add port, respectively. Within a MCADM system, two signals are modulated by cross phase modulation in order to generate the optical tweezer for trapping the microparticle [17].

1.5 Scope of Thesis

The scope of this thesis is proposed to find the suitable parameter specification in order to generate tweezer signals for trapping tool applications by using optical Racetrack Add-Drop Modulator (RADM), optical Circular Add-Drop Modulator (CADM) and optical Modified Circular Add-Drop Modulator (MCADM). Design of tweezer and generators using MCADM and then to simulate for performance comparison of three microring modulators. The assessed performance parameters are output signal form (potential well/tweezer), depth of well, width of well, net force, trapping tools capacity and velocity. This thesis focuses on constrained problem of 2 nm polystyrene particle is trapped and manipulated with $\approx 8 \mu\text{m/s}$ of velocity. The center wavelength of input signal for particle trapping is 1550 nm. The force theory for support and describe the originated net force in Rayleigh regime ($X \ll 1$). The suitable parameters are the intensity coupling coefficient (κ_1) between the input and the throughput ports is 0.9, the intensity coupling coefficient between the center add-drop or the center microring and the left or right microring (κ_2, κ_4) are 0.35, the intensity coupling coefficient (κ_3) between the add and the drop ports is 0.1, the size of center ring radius (R_c or R_d) is assigned by radii equal 20 μm , the left and right ring radii (R_R or R_L) are 10 μm , The waveguide fabricated from InGaAsP for core and cladding is InP. The width and height of the waveguide are 0.7 μm and the length of bus waveguide from input port to the MCADM ring is 5 μm .

1.6 Organization

This thesis is organized as followings: Chapter 2 presents the optical tweezer principle, the inputs for microparticle trapping, optical modulation techniques, the fabricated microring resonator materials, the fabricated microring resonator sizes, and the literature review. The studied process of MCADM design, the proposed mathematical transfer function, the characteristics and the results analysis of MCADM, the constrained problem and the design of tweezer and generators using

MCADM are presented in Chapter 3. As one of the major contributions, Chapter 4 shows the experimental results and discussion. Finally, Chapter 5 proposes the optimized parameters for the proposed microring modulators and conclusion and provides recommendations for future research.

Chapter 2

Theoretical Background and Literature Reviews

For a better understanding, this chapter will provide the primitive theories which contribute to our proposed system. First, the optical tweezer principle is introduced. Then, the optical modulation technique is described. Especially, the cross-phase modulation is utilized for generating the tweezer form within the system. Consequently, the fabricated ring resonator material and fabricated ring radius size are explored. Finally, the molecular trapping and manipulation literatures using microring resonators are reviewed and summarized.

2.1 Optical Tweezer Principle

In 1619, Johannes Kepler discovered why comet tail points away from the sun because it is pushed by radiation pressure force of the sun. Two hundred and fifty-four years later, James Clerk Maxwell (1873) showed theoretically that light itself can exert optical force or “radiation pressure”. In the early in 1970, Arthur Ashkin pioneered the field of optical tweezer. Commonly, every light photon carries energy $h\nu$ and momentum h/λ , it is straightforward to state that if every photon light is absorbed by an object, the momentum transferred from a light beam of power P , leads to a radiation pressure or reaction force F on the particle or molecular as shown in Figure 2.1 and the equation of force given by

$$F = \frac{Qn_m P}{c} \quad (2.1)$$

where Q represents the fraction of power utilized to exert force, n_m is the index of refraction of the suspending medium, P is the incident laser power and c is the speed of light in the vacuum.

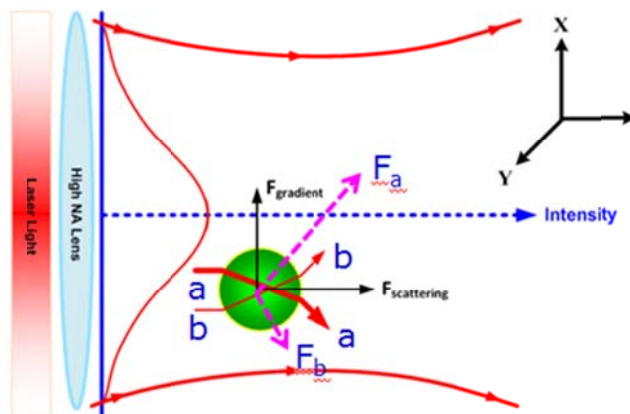


Figure 2.1 The optical or optical tweezer generation [1]

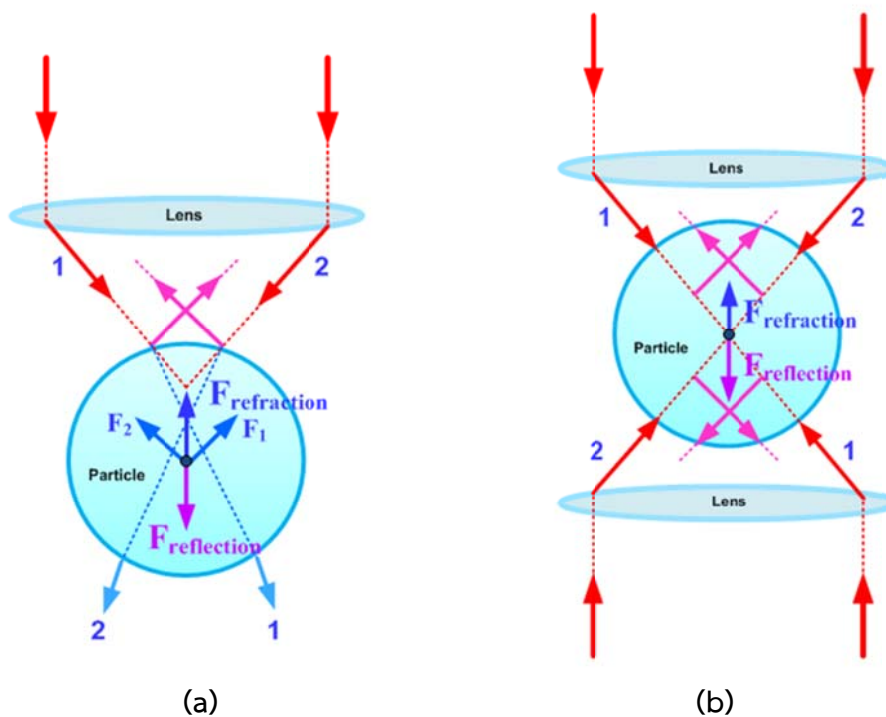


Figure 2.2 The molecular trapping mechanism, (a) Single-beam optical trapping force, (b) Dual-beam optical trapping force [17]

The molecular trapping mechanism is demonstrated by a single-beam of laser light subject to the assumption of 2 equal optical rays (1 and 2) of light are projected through a lens and affect the particle nearly focal length. With the condition of refractive index of particles, there is some radiation pressure force transmitted through the particle and produce refraction force, while the rest of the radiation pressure force is reflected in the direction as shown in the Figure 2.1 (a). The stability of particle trapping is occurred whenever the summation of refraction and reflection force is equal. Figure 2.1 (b) shows the molecular trapping mechanism of dual-beam

optical trapping force which is called “optical tweezer”. The trapping mechanism is similar with a single-beam optical trapping force.

After understanding the radiation pressure force origination and molecular trapping mechanism, the properties of a molecule that are suitable for trapping are necessary to realize. There are 3 properties of the molecule [1] which must be considered for optical trapping as presented in Figure 2.2. First, the size of molecule ranges from a few nanometers to hundred micrometers. Second, the ratio of refractive and reflective force needs to be balanced. The experimental results of Svoboda and Block [17] showed that the refractive indices of polystyrene ($n = 1.47$) and silica ($n = 1.57$) are suitable for applying in the experiment of optical trapping while $n = 1.57$ the magnitude of trapping force is decreasing. Lastly, property is the input power used for molecular trapping does not destroy the particle.

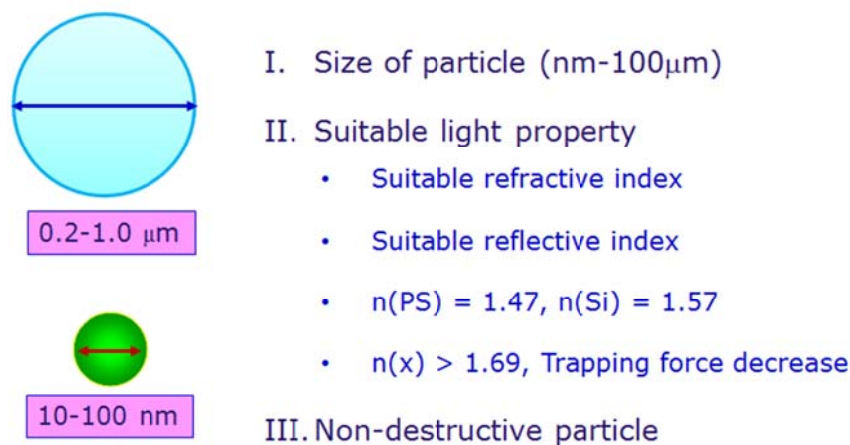


Figure 2.3 The molecular properties

Usually, the optical tweezer can be generated by a laser that is strongly focused through a lens with a very short focal length (most often a high numerical aperture [NA] microscope objective) in order to increase its intensity. The reaction force F from the laser source on the molecule can be divided into scattering (F_{scatt}) and gradient forces (F_{grad}). The scattering force is a result of percussion between photon and particle in the propagation direction of the incident laser light and proportional to the intensity, while the gradient force is originated by a difference in pressure across a surface in the perpendicular direction with the incident laser light. The stability of optical trapping occurs when the magnitude of gradient force is greater than scattering force ($F_{grad} > F_{scatt}$), while the particle velocity arises under the condition of the summation of force (F_{net}) between gradient and scattering force is higher than the viscosity (F_{vis}) or friction force (F_{fric}). The schematic of optical tweezer is shown in Figure 2.4 and the relation of forces are described by

$$F_{scatt} = \frac{I_0 \sigma n_m}{c} \quad (2.2)$$

$$\sigma = \frac{128}{3\lambda^4} \pi^5 a^6 \left(\frac{m^2 - 1}{m^2 + 2} \right)^2 \quad (2.3)$$

where I_0 is the intensity of the incident light, σ is the scattering cross section of the particle, n_m is the index of refraction of the medium, a is a particle radius, m is the ratio of the index of refraction of the particle to the index of the medium (n_p / n_m), and λ is the wavelength of the trapping laser.

$$F_{grad} = \frac{2\pi\alpha}{cn_m^2} \nabla I_0 \quad (2.4)$$

where

$$\alpha = n_m^2 a^3 \left(\frac{m^2 - 1}{m^2 + 2} \right)^2 \quad (2.5)$$

is the polarizability of the sphere. The gradient force is proportional to the intensity gradient, and points up the gradient when $m > 1$. On the other word, the summary property of optical tweezer can be categorized into 3 properties that are the depth of well, the width of well and the net force. The capability and stability of trapping is upon the ratio of magnitude between $F_{grad} > F_{scatt}$ and $F_{net} > F_{vis}$. The magnitude of force can be calculated by an optical force theory which identify by

$$X = \frac{D\pi n_m}{\lambda} \quad (2.6)$$

where X is identification coefficient and D is particle diameter. The optical force theory can be divided into 3 cases which are:

- I. $X \leq 1$ the force is calculated in the Rayleigh regime and the magnitude of force is in the range of femto to piconewtons.
- II. $1 \leq X < 100$ the force is calculated in the Mie regime and the magnitude of force is in the range of piconewtons.
- III. $X > 100$ the force is calculated in the Optics Ray regime and the magnitude of force is in the range of nanonewtons.

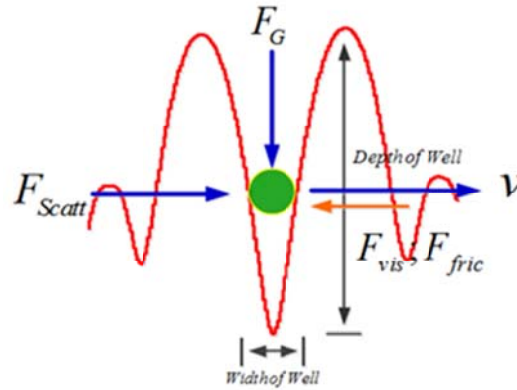


Figure 2.4 The optical tweezer properties

2.2 Input Signals for Microparticle Trapping

This section, the theory of input signals for generating tweezer waveform for trapping tool application is described. Usually, the laser light can be modeled into 3 kinds of signals: there are Gaussian, Bright and Dark Soliton, which can be explained as follows:

- **Gaussian Input Signal**

Typically, the bell curve which is well known as “Gaussian Signal [18]” is modeled of laser light to be used as an input of optical tweezer experiments and simulation. This thesis, the Gaussian beam is modeled for an input of MCADM. Figure 2.5 shows the two-dimensional intensity profile of a Gaussian with mean (μ) of the curve is ‘0’ and the standard deviation (σ) is ‘1’. The complex electric field of signal can be described by the paraxial Helmholtz equation as follows:

$$E(r, z) = E_0 \frac{w_0}{w(z)} \exp\left(\frac{-r^2}{w(z)^2} - ikz - ik \frac{r^2}{2R(z)} + i\zeta(z)\right), \quad (2.7)$$

where r is the radial distance from the center axis of the beam, z is the axial distance from the beam's narrowest point (the "waist"),

i is the imaginary unit ($i^2 = -1$),

$k = \frac{2\pi}{\lambda}$ is the wave number (rad/m), $E_0 = |E(0, 0)|$,

$w(z)$ is the radius at which the field amplitude and intensity drop to $1/e$ and $1/e^2$ of their axial values, respectively,

$w_0 = w(0)$, is the waist size,

$R(z)$ is the radius of curvature of the beam's wavefronts, and

$\zeta(z)$ is the Gouy phase shift, an extra contribution to the phase that is seen in Gaussian beams.

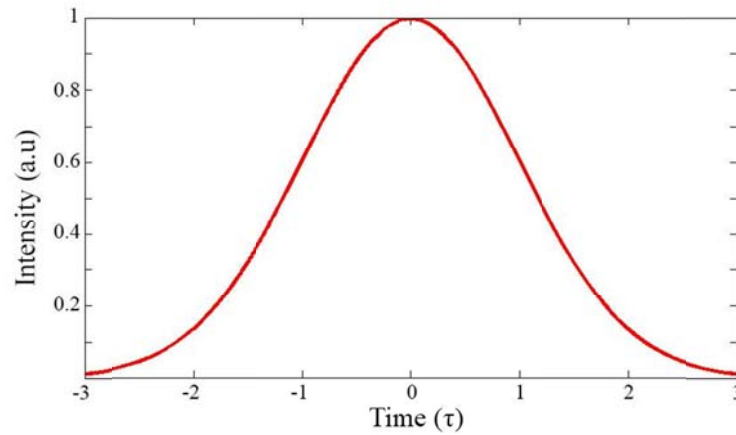


Figure 2.5 Two-dimensional intensity profile of a Gaussian beam

Additionally, the field has a time dependence factor $e^{j\omega t}$ that has been suppressed in the above expression. The corresponding time-averaged intensity (or irradiance) distribution is

$$I(r, z) = \frac{|E(r, z)|^2}{2\eta} = I_0 \left(\frac{w_0}{w(z)} \right)^2 \exp\left(\frac{-2r^2}{w^2(z)} \right), \quad (2.8)$$

where $I_0 = I(0, 0)$, is the intensity at the center of the beam at its waist. The constant η is the characteristic impedance of the medium in which the beam is propagating. For free space, $\eta = \eta_0 = \sqrt{(\mu_0 / \epsilon_0)} = 1 / (\epsilon_0 c) \approx 376.7 \Omega$.

- **Dark and Bright Soliton Signals**

“Solitons are the pulses with a certain balance of nonlinear and dispersive effects [19],” which is given the soliton definition by German solitonen. In general, the amplitude and spectral shape of a short optical soliton pulse is virtually constant during propagation in a transparent medium due to the Kerr effect and chromatic dispersion. In other word, under certain circumstances, the effects of Kerr nonlinearity and dispersion can exactly cancel each othe so that the amplitude and spectral shape of the pulses is preserved even over long propagation distances [20, 21] as shown in Figure 2.6. This soliton phenomenon was first observed in the context of water waves [20], but later also found in optical fibers [22].

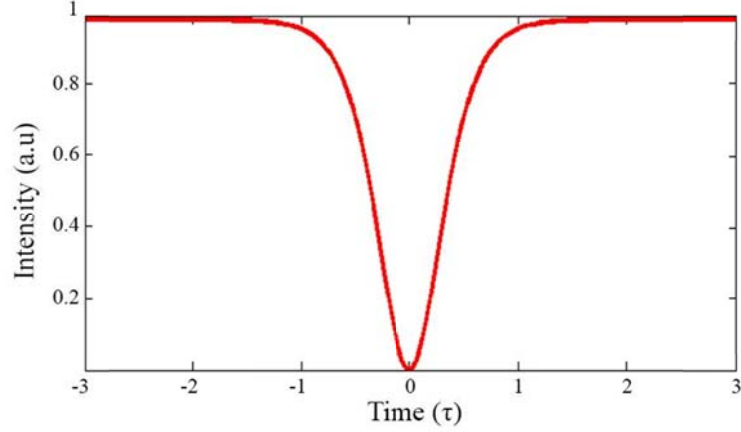


Figure 2.6 The geometric Bright Soliton

There are 2 kinds of solutions for system simulation, the first kind is Bright Soliton (E_B) and the second one is Dark Soliton (E_D). One of our simulation input is the Dark Soliton which fed into control (add) port of MCADM. The electrical field variation of Bright and Dark Soliton can be reduced and given by the following equations:

$$E_B(t) = A \operatorname{sech} \left[\frac{T}{T_0} \right] \exp \left[\left(\frac{z}{2L_D} \right) - i\phi(t) \right] \quad (2.9)$$

$$E_D(t) = A \tanh \left[\frac{T}{T_0} \right] \exp \left[\left(\frac{z}{2L_D} \right) - i\phi(t) \right] \quad (2.10)$$

in which A and z are the optical field amplitude and propagation distance, respectively. $\phi(t) = \phi_0 + \phi_{NL} = \phi_0 + \frac{2\pi n_2 L}{A_{eff} \lambda} |E_0(t)|^2$ is the random phase term related to the temporal coherence function of the input light, ϕ_0 is the linear phase shift, ϕ_{NL} is the nonlinear phase shift, n_2 is the nonlinear refractive index of waveguide material. The effective mode core area of the device is given by A_{eff} , $L = 2\pi R_{ad}$, R_{ad} is the radius of device, λ is the input wavelength light field. T is a soliton pulse propagation time in a frame moving at the group velocity, $T = t - \beta_1 * z$, where β_1 and β_2 are the coefficients of the linear and second-order terms of the Taylor expansion of the propagation constant. $L_D = T_0^2 / |\beta_2|$ is the dispersion length of the soliton pulse. T_0 in equation is a soliton pulse propagation time at initial input (or soliton pulse width), where t is the soliton phase shift time, and ω_0 is the frequency shift of the soliton. This solution describes a pulse that keeps its temporal width invariance as it propagates, and thus is called a “temporal soliton”. When a soliton peak intensity

($|\beta_2/\Gamma T_0^2|$) is given, then T_0 is known. For the soliton pulse in the microring device, a balance should be achieved between the dispersion length (L_D) and the nonlinear length ($L_{NL} = 1/\Gamma\phi_{NL}$), where $\Gamma = n_2 * k_n$, is the length scale over which dispersion or nonlinear effects makes the beam become wider or narrower. For a soliton pulse, there is a balance between dispersion and nonlinear lengths.

2.3 Optical Modulation Techniques

Self-Phase Modulation (SPM) [23] is once resulting from the optical Kerr effect. When ultra-short pulses of light transmit in a medium, it will induce a varying refractive index of the medium due to the optical Kerr effect. This variation in refractive index will produce a phase shift in the pulse, leading to a change of the pulse's frequency spectrum. From third order nonlinearity given effective refractive index (n_{eff}) of the medium upon the intensity described as

$$n_{eff} = n_0 + n_2 I(t) \quad (2.11)$$

where n_0 is the refractive index of the medium in the absence of light fields, n_2 is the nonlinear refractive index and $I(t)$ is the intensity of laser radiation with respect to time t . Then, the results of the nonlinear phase shift ($\phi(t)$) with pulse at a distance L is given by

$$\phi(t) = \frac{\omega}{c} \cdot n_2 I(t) L \quad (2.12)$$

where ω is the pump frequency and c is speed of light in vacuum. If consider the phase change per unit (γ_{SPM}) of optical power and length can be determined as

$$\gamma_{SPM} = \frac{2\pi n_2}{\lambda A_{eff}} \quad (2.13)$$

where λ is the center wavelength of the input signal and A_{eff} is an effective core area.

Cross-phase effect (XPM) [23, 24] is another nonlinear effect phenomenon where one wavelength of light can affect the phase of another wavelength by the optical Kerr effect. Normally, when two or more pulses of light (pulse with different

frequencies, polarizations or mode of structure) propagate simultaneously in a medium, the cross-phase modulation is always accompanied by SPM and occurs because the nonlinear refractive index depends not only on itself intensity beam but also on the intensity of the other propagating beams.

2.4 Fabricated Microring Resonator Materials

In order to fabrication or simulation the MCAMD device to generate optical tweezer signals for particle trapping and manipulation applications. Many factors must be aware such as fabrication method and cost, material, thermal effect, optical loss and so on. In the experiment, one factor that affects the performance of the propagation of signals in the waveguide is material, especially the refractive index and optical loss in the waveguide. The theory shows that the refractive index of the material affects the number of the resonant mode in microring, while the optical loss affects the capability of transition. Therefore, in this section, the summaries of popular fabricated materials from several survey literatures are proposed in tabular form in Table 2.1 which these values are applied in our experiment in Chapter 4.

Table 2.1 The properties of waveguide materials

Material	n_0	n_2 (cm^2/W)	λ_0 (nm)	Optical Loss(dB/cm)	Reference
InP	3.17	4.5×10^{-12}	1,550	< 0.1	[25-27]
InGaAsP	3.34	4.27×10^{-17}	1,550	< 0.1	[26-27]
AlGaAs	3.28	1.50×10^{-17}	$\approx 1,545$	< 0.1	[26], [28]
Ta ₂ O ₅	≈ 2.20	7.23×10^{-19}	1,550	1.8	[29], [32]
SiN	2.20	2.40×10^{-15}	1,550	2.1 ± 0.2	[30-31]
SiO ₂	1.53	2.40×10^{-16}	1,550	4	[26], [30-31]

2.5 Fabricated Microring Resonator sizes survey

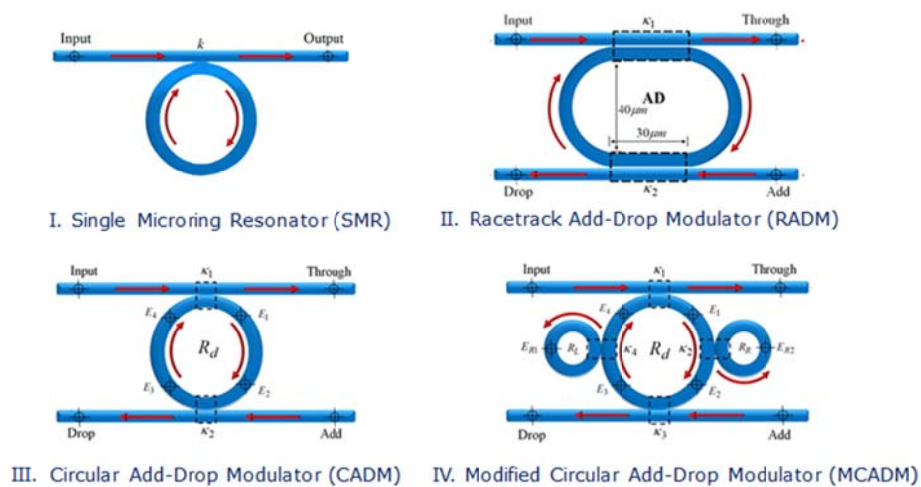
As mentioned in the previous section, ring radius size influences the amount of the resonant mode in the microring. Consequently, this section shows the survey ring radius size information from 2002 to 2013. For the past decade, the survey results have indicated that the advance technology allows the decrease ring resonator size from 100 μm to 1 μm as a summary survey in Table 2.2. The purpose of this survey is limiting the scope of the ring radius size parameter variance that effect to the optical tweezer output signal generated by proposed MCADM. This thesis varies the ring radius range between 10 to 20 μm according to Hong Cai and Andrew W. Poon [15].

Table 2.2 The properties of waveguide materials

Order	Publication Year	Ring Radius Size (μm)	Author	Reference
1	2002	10	V. Van et. al	[33]
2	2003	20-200	Z. Bian et. al	[34]
3	2004	5	T. Barwicz et. al	[35]
4	2005	5, 20	Y. Kokuban et. al	[36]
5	2006	8.004	T. Barwicz et. al	[37]
6	2006	60	A. Yalçın et. al	[38]
7	2008	1.5	Q. Xu et. al	[39]
8	2010	20	H. Cai et. al	[40]
9	2012	1, 5, 10	W. Bogaerts et. al	[41]
10	2013	80	P. Rabiei et. al	[42]

2.6 Literature Reviews

Generally, there are 4 microring devices used in the experiment and simulation for molecular trapping and manipulation. These device groups are composed of the single microring resonator (SMR) [13], Racetrack Add-Drop Modulator (RADM) [15], Circular Add-Drop Modulator (CADM) [14] and Modified Circular Add-Drop Modulator [16] as shown in Figure 2.7. This section reviews the literature concerned with our thesis.

**Figure 2.7** Four microring resonator and modulator devices [13-16]

The motivation of this thesis imitates the SRM device of Shiyun Lin and his colleagues [15] which planar silicon microring resonator is used to propel the 1.1 μm of polystyrene around the ring perimeter. The SMR with 5 and 10 μm and width 500 nm are fabricated on silicon on insulator (SOI) wafer with a 220 nm top Si layer using electron beam lithography and reactive ion etching. Laser sources with center wavelength (λ) 1,550 nm is fed into a ring resonator from a waveguide bus. The power input into waveguide are 9 and 4.5 mW for 5 and 10 μm respectively. The output results show the particle can be trapped and propelled around the ring at hundreds of micrometers per second and producing periodic revolutions at a few hertz. Moreover, this paper uses 3D-FDTD to simulate the results by input power 1 W. Then, they estimate the output power, net force, transmittance and velocity and compare with the measurement results. The microring structure and its results are demonstrated in Figures 2.8-2.9.

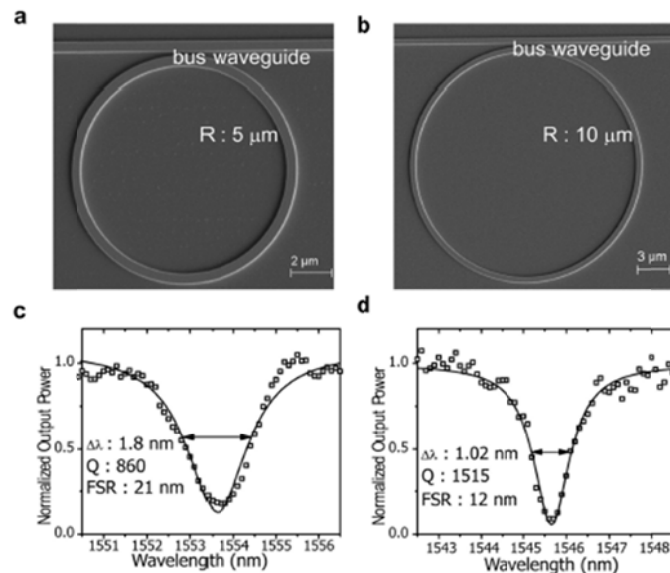


Figure 2.8 SEM image and transmission spectra of microring resonator, (a) SEM image of microring with radii of 5 μm , (b) SEM image of microring with radii of 10 μm , (c) Transmission spectra of ring radii of 5 μm , (d) Transmission spectra of ring radii of 10 μm [15].

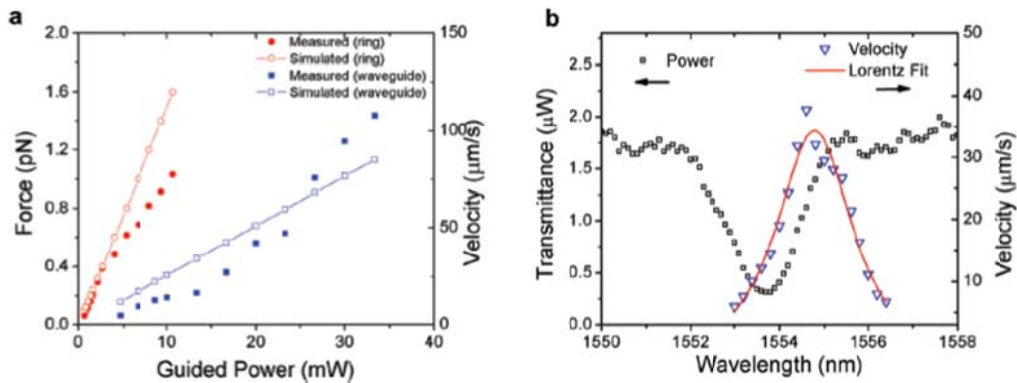


Figure 2.9 The longitudinal of optical force and velocity, (a) Measurement velocity and optical force as a function of input power, (b) Transmission spectra of the microring resonator near a TM resonance mode and the cycling velocity of polystyrene beads [15].

In 2002, Dominik G. Rabus [14] proposed the circular microring resonator (CADM) and their mathematical transfer function for describing the output signal at through and drop port. The physical geometry, output results and schematic model are shown in Figures 2.10-2.12.

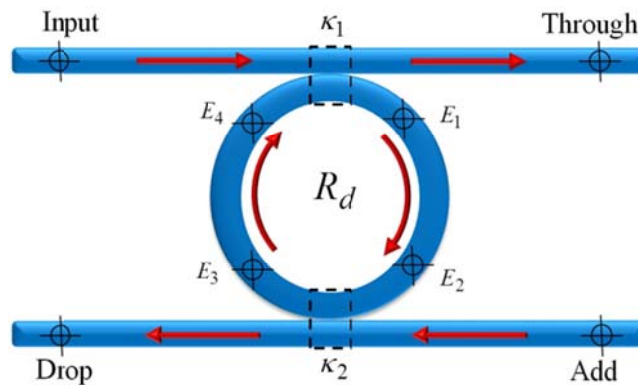


Figure 2.10 The physical geometry of CADM [14].

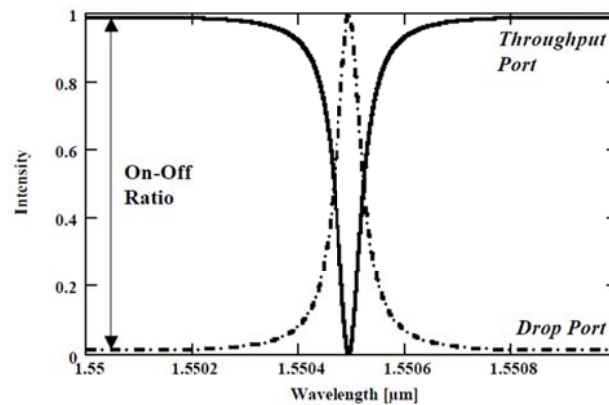


Figure 2.11 The output characteristic signal at throughput and drop ports of CADM [14].

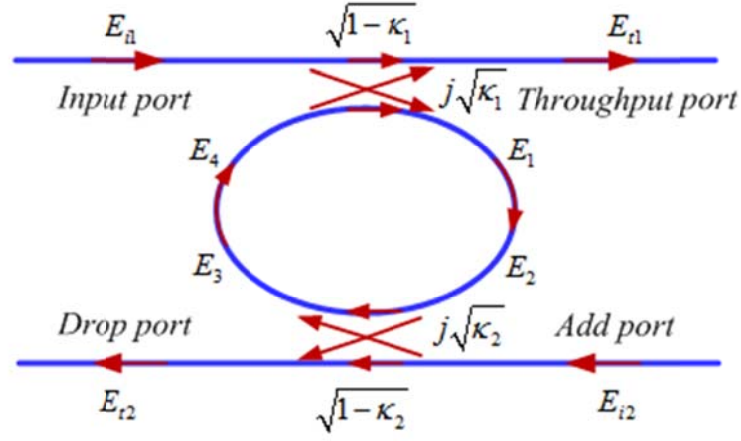


Figure 2.12 The schematic model of CADM [14].

The electrical fields at the position E_a , E_b , throughput (E_{t1}) and drop ports (E_{t2}) of this schematic model can be described as follows:

$$E_a = E_{t1} \cdot j \cdot \sqrt{\kappa_1} + E_b \cdot \sqrt{1 - \kappa_1} e^{(-\frac{\alpha L}{2} - jk_n L)} \quad (2.14)$$

$$E_b = E_a \cdot \sqrt{1 - \kappa_2} e^{(-\frac{\alpha L}{2} - jk_n \frac{L}{2})} \quad (2.15)$$

$$E_{t1} = E_b \cdot j \cdot \sqrt{\kappa_1} \cdot e^{(-\frac{\alpha L}{2} - jk_n L)} + E_{i1} \cdot \sqrt{1 - \kappa_1} \quad (2.16)$$

$$E_{t2} = E_a \cdot j \cdot \sqrt{\kappa_2} \cdot e^{(-\frac{\alpha L}{2} - jk_n \frac{L}{2})} \text{ at } E_{i2} = 0 \quad (2.17)$$

The electrical field transfer function at throughput and ports are

$$\frac{E_{t1}}{E_{i1}} = \frac{-\sqrt{1 - \kappa_2} \cdot e^{(-\frac{\alpha L}{2} - jk_n L)} + \sqrt{1 - \kappa_1}}{1 - \sqrt{1 - \kappa_1} \cdot \sqrt{1 - \kappa_2} \cdot e^{(-\frac{\alpha L}{2} - jk_n L)}} \quad (2.18)$$

$$\frac{E_{t2}}{E_{i1}} = \frac{-\sqrt{\kappa_1 \cdot \kappa_2} \cdot e^{(-\frac{\alpha L}{2} - jk_n \frac{L}{2})}}{1 - \sqrt{1 - \kappa_1} \cdot \sqrt{1 - \kappa_2} \cdot e^{(-\frac{\alpha L}{2} - jk_n L)}} \quad (2.19)$$

Given :

$$y_1 = \sqrt{1 - \kappa_1} \quad \text{and} \quad y_2 = \sqrt{1 - \kappa_2} \quad (2.20)$$

Therefore, the transfer function density intensity at throughput and drop ports with be relevant to the output signal in Figure 2.10 are

$$\frac{I_{t1}}{I_{i1}} = \left| \frac{E_{t1}}{E_{i1}} \right|^2 = 1 - \frac{(1-y_1^2)(1-y_2^2)x^2}{(1-y_1y_2x)^2 + 4y_1y_2x \sin^2\left(\frac{\phi}{2}\right)} \quad (2.21)$$

$$\frac{I_{t2}}{I_{i1}} = \left| \frac{E_{t2}}{E_{i1}} \right|^2 = \frac{(1-y_1^2)(1-y_2^2)x}{(1-y_1y_2x)^2 + 4y_1y_2x \sin^2\left(\frac{\phi}{2}\right)} \quad (2.22)$$

In the same year, Hong Cai and Andrew W. Poon [15] reported that the 1 μm sized polystyrene particles can be transported and manipulated on racetrack add-drop silicon nitride microring resonator (RADM) devices in an integrated optofluidic chip. The racetrack microring is comprised of two arcs with diameter 50 μm and coupling length 30 μm . The waveguide width and height are 0.4 and 0.7 μm and evanescent coupling gap spacing is approximate 0.35 μm . The microscope depth of focus is nearly 0.1 μm , input power from laser source is 120 mW at center wavelength 1,550 nm, with the insertion loss in the system around 16-20 dB. They use the CCD camera to capture the position of particle which travels on the mirroring and then calculate the velocity at different positions that summarize in Table 2.3. The physical geometry, schematic of optical manipulation of particle on RADM and the output results is shown in Figures 2.13-2.15.

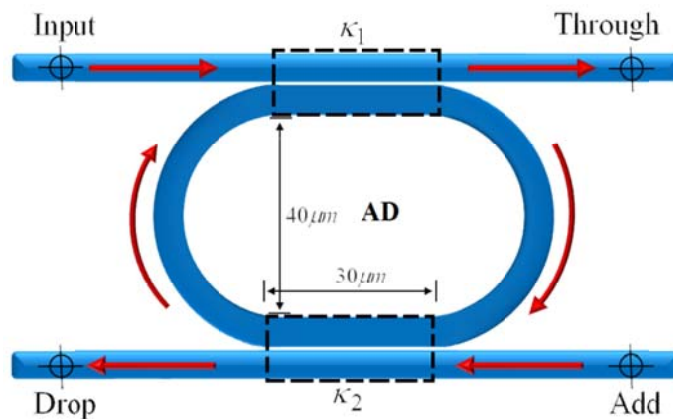


Figure 2.13 The physical geometry of RADM [15].

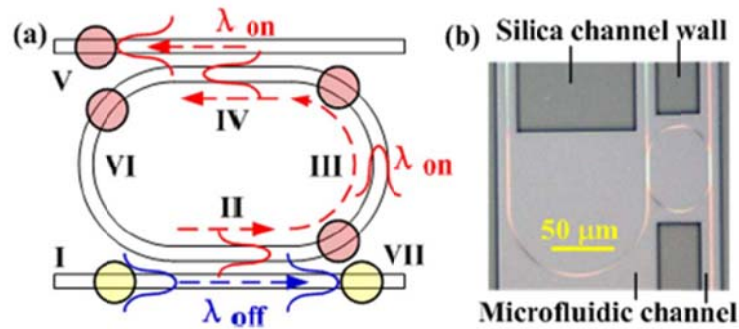


Figure 2.14 The schematic of optical manipulation of particle on RADM, (a) Schematic of optical manipulation of particle on RADM, (b) Optical micrograph of the optofluidic device [15].

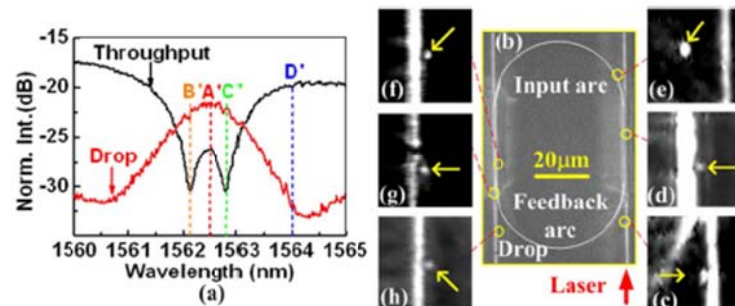


Figure 2.15 The output at throughput and drop ports of RADM and optical micrograph of device with microparticle positions (a) Measured throughput and drop ports transmission spectra of device II (b) Optical micrograph of the device with particle positions (c) 0, (d) 50, (e) 60, (f) 187, (g) 254 and (h) 276 [15].

Table 2.3 The measurement velocity of particle positions

Region	Velocity		
	On Resonance	Off Resonance	
1	$\lambda = 1,564 \text{ nm}$	$\lambda = 1,565.56 \text{ nm}$	$\lambda = 1,562.5 \text{ nm}$
2	-	-	-
3	$\approx 1 \mu\text{m/s}$	$\approx 3.7 \mu\text{m/s}$	$\approx 2.1 \mu\text{m/s}$
4	-	$\approx 2 \mu\text{m/s}$	$\approx 1.2 \mu\text{m/s}$
5	-	$\approx 1.5 \mu\text{m/s}$	$\approx 2.9 \mu\text{m/s}$
6	-	-	$\approx 1.3 \mu\text{m/s}$
7	-	$\approx 1.8 \mu\text{m/s}$	-
8	$\approx 1.4 \mu\text{m/s}$	-	-

Recently, the optical vortices (optical tweezer) generation using a PANDA or MCADM for drug trapping tool and delivery applications is proposed by Nattaporn Suwanpayak and her colleagues [16]. The optical vortices are generated by cross-phase modulation of Dark Soliton signal and Gaussian signal within the MCADM. The Dark Soliton signal is used as a functional to generate optical vortices while Gaussian signal used to control the amplitude of vortices signal. The physical geometry of MCADM and results are shown in Figures 2.16-2.18. In addition, they proposed the mathematical transfer function to describe the output vortices. The electrical field signal at the position of $E_1 - E_4$ can be described as the following:

$$E_1 = j\sqrt{\kappa_1 x_1} \cdot E_{i1} + j\sqrt{\kappa_1 x_1 y_1 y_2} \cdot E_{i2} \cdot E_L \cdot e^{\frac{\alpha L}{2} - jk_n \frac{L}{2}} \quad (2.23)$$

$$E_2 = E_R \cdot E_1 \cdot e^{\frac{\alpha L}{2} - jk_n \frac{L}{2}} \quad (2.24)$$

$$E_3 = jx_2 E_{i2} + x_2 y_2 E_R \cdot E_1 \cdot e^{\frac{\alpha L}{2} - jk_n \frac{L}{2}} \quad (2.25)$$

$$E_4 = j\sqrt{\kappa_3 x_2} \cdot E_L \cdot E_{i2} + x_2 y_2 E_R \cdot E_1 \cdot E_L \cdot e^{\frac{\alpha L}{2} - jk_n \frac{L}{2}} \quad (2.26)$$

where $x_1 = \sqrt{1 - \gamma_1}$, $x_2 = \sqrt{1 - \gamma_2}$, $y_1 = \sqrt{1 - \kappa_1}$ and $y_2 = \sqrt{1 - \kappa_2}$.

The electrical field at throughput port is

$$E_{i1} = AE_{i1} \cdot B \cdot E_{i2} \cdot e^{\frac{\alpha L}{2} - jk_n \frac{L}{2}} \cdot \left[\frac{CE_{i1} \left(e^{\frac{\alpha L}{2} - jk_n \frac{L}{2}} \right)^2 + DE_{i2} \left(e^{\frac{\alpha L}{2} - jk_n \frac{L}{2}} \right)^3}{1 - F \left(e^{\frac{\alpha L}{2} - jk_n \frac{L}{2}} \right)^2} \right] \quad (2.27)$$

where $A = \sqrt{(1 - \kappa_1)(1 - \gamma_2)}$, $B = \sqrt{(1 - \gamma_1)(1 - \gamma_2)\kappa_1(1 - \kappa_2)}E_L$,

$C = \kappa_1(1 - \gamma_1)\sqrt{(1 - \gamma_2)\kappa_2}E_R E_L$, $D = (1 - \gamma_1)(1 - \gamma_2)\sqrt{(1 - \kappa_1)(1 - \kappa_2)}E_R E_L^2$,

$F = (1 - \gamma_1)(1 - \gamma_2)\sqrt{(1 - \gamma_1)(1 - \gamma_2)(1 - \kappa_1)(1 - \kappa_2)}E_R E_L$,

The electrical field at drop port is expressed as

$$E_{t1} = \sqrt{(1-\gamma_2)(1-\kappa_2)}E_{i2} - \frac{\left[\begin{aligned} &\sqrt{(1-\gamma_1)(1-\gamma_2)\kappa_1\kappa_2}E_R E_{i1} e^{-\frac{\alpha L}{2} - jk_n \frac{L}{2}} \\ &+ X E_R E_L \left(e^{-\frac{\alpha L}{2} - jk_n \frac{L}{2}} \right)^2 \\ &1 - Y E_R E_L \left(e^{-\frac{\alpha L}{2} - jk_n \frac{L}{2}} \right)^2 \end{aligned} \right]}{\quad} \quad (2.28)$$

where $X = (1-\gamma_2)\sqrt{(1-\gamma_1)(1-\kappa_1)\kappa_2(1-\kappa_2)}$, $Y = \sqrt{(1-\gamma_1)(1-\gamma_2)(1-\kappa_1)(1-\kappa_2)}$

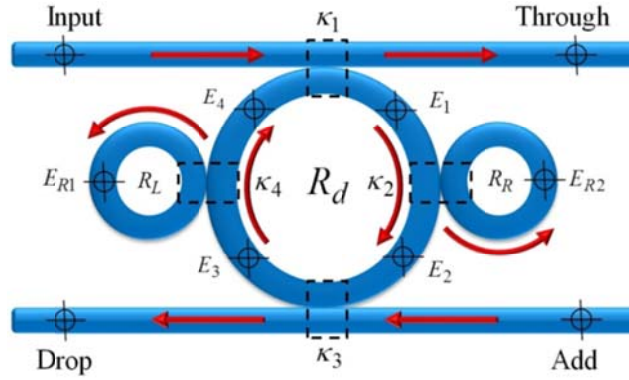


Figure 2.16 The physical geometry of MCADM [16].

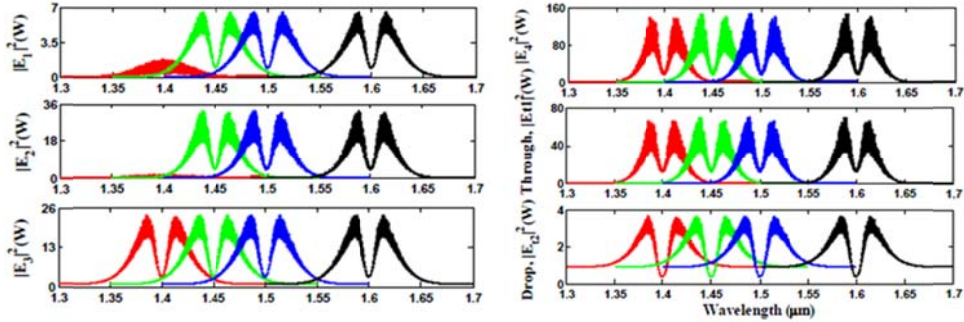


Figure 2.17 Simulation results for Dark-Gaussian input, where $R_d = 10 \mu\text{m}$, $R_R = R_L = 5 \mu\text{m}$, and the coupling coefficients of the ring resonator are $\kappa_1 = 0.5$, $\kappa_2 = 0.1$, $\kappa_3 = 0.35$, $\kappa_4 = 0.1$ [16].

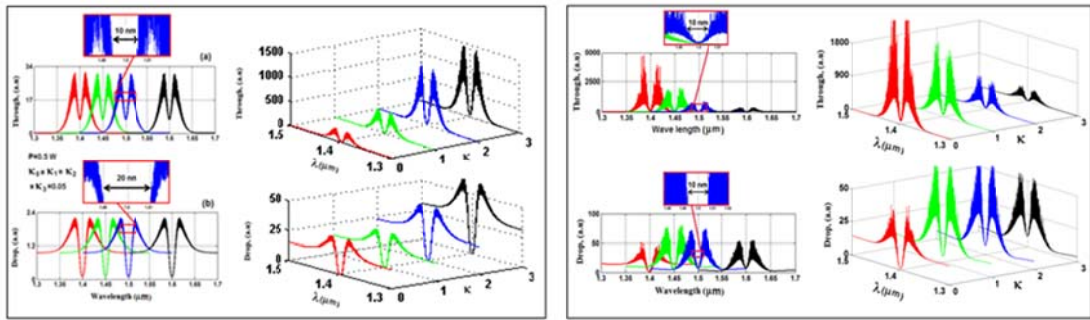


Figure 2.18 Simulation results for Dark-Gaussian input, where $R_d = 10 \mu\text{m}$, $R_R = R_L = 2 \mu\text{m}$, and the coupling coefficients of the ring resonator are $\kappa_1=0.5$, $\kappa_2=0.1$, $\kappa_3=0.35$, $\kappa_4=0.1$ [16].

In the same year, molecular buffer using PANDA ring resonator for drug delivery is proposed [43]. This research is a developed application from the previous work. The authors presented the idea to use optical vortices to trap molecule from storage buffer. The physical geometry of a molecule buffer system is shown in Figure 2.19.

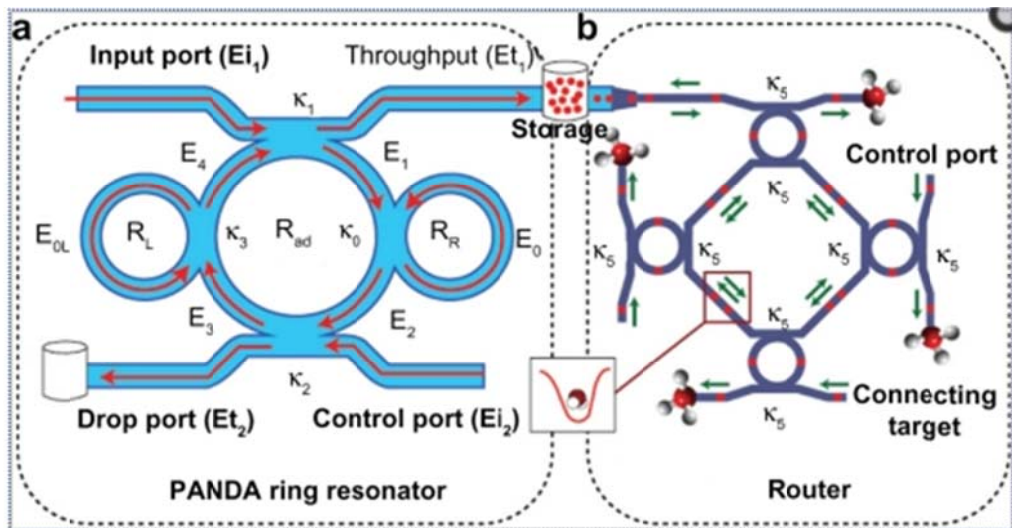


Figure 2.19 Physical geometry of a molecular buffer system (a) a PANDA ring resonator, (b) a wavelength router [43].

There are several studies about optical vortices and optical tweezers which show in Table 2.4; however, these studies are divided into 3 groups as follows:

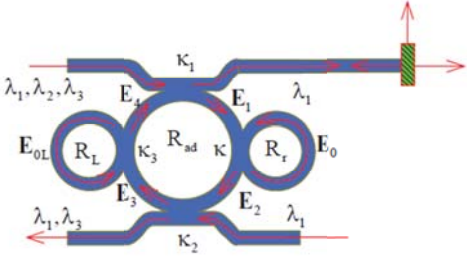
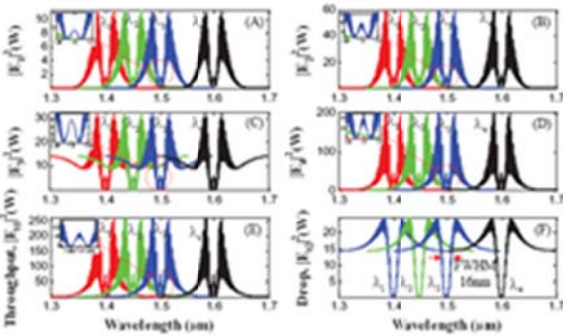
First group is the generation of optical input signal described in [14], [50] and [53]. In reference [14], the add/drop filter is used to explain the output signal at throughput and drop port of device. A doughnut-like laser beam [50] is generated using the resonator which consists of a toric mirror, a flat output coupler, and a w-axicon with a movable center axicon. This signal is similar to the origination of laser sources in TM01 mode. The last literature review of this group is solitons generation

using the cascade microring resonator system [53]. The narrow pulse width originated from the reduction size of cascade microring resonator.

The second is optical trapping tool (optical capsule, optical potential well or optical vortices, optical spin and optical tweezers) generation. The input signal of this group is Gaussian and Bright or Dark Solitons are fed into each device. The literature reviews are [13], [15-16], [44-46], [48], [51], [54] and [56-57]. The single microring resonator is used to trap 1.1 μm of polystyrene is presented in [13], then Hong Cai and Andrew W. Poon [15] use racetrack add-drop filter to trap 1 μm of polystyrene with the different positioned velocity. The optical capsules for molecular motor use [51] are generated by using the cascade system of single ring resonator and PANDA ring resonator. The input signals are dark and bright orthogonal solitons used to form tweezers capsules within the system and observed at the same time at the output ports. After that reference [16] use Dark Soliton and Gaussian pulse modulation within PANDA to generate tweezers signal. As the same with literature reviews [44-46], haft-PANDA and PANDA ring resonators are used to generate optical tweezers signal for trapping tool applications. The optical vortices generation using PANDA ring resonator is proposed in [54]. Multi optical trapping tool and multi tweezers using the cascade add-drop devices are proposed in [56-57]. The major advantage of cascade microring device is the increase of speed as seen from the frequency of output signals.

Third group is its application composed of [43], [47], [49], [52], [55] and [58]. In reference [43], the optical tweezers signal in [16] is applied for the molecular buffer system. Then reference [47] use PANDA ring resonator coating by gold to generate whispering gallery mode signal for atom or molecule trapping and the design of drug delivery system [49] using tweezers signal is proposed by the same authors. The design of microring resonator system for microsurgery use is proposed in [52]. By the advantage of optical tweezers, the microsurgery is possibility. System of a quantum-molecular transportation using the multi-optical tweezers is presented in [55]. The transporter is generated by a Dark Soliton which can be transmitted into an optical link. The last literature in this group is application of PANDA ring resonator [58] for drug trapping and delivery.

Table 2.4 The summary of other references

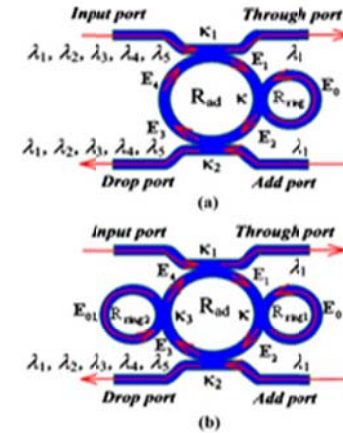
Title	Method	Parameters	Structure/Results
<p>1. Dynamic Optical Tweezers Generation using a PANDA Ring Resonator [44]</p>	<p>Optical tweezers are generated by Bright or Dark Soliton at input port and Gaussian signal at add port. The optical tweezers in the design system can be tuned and amplified by the magnitude of Gaussian signal. In application, the optical tweezers can be stored and Trapped light/atom. The commercial simulation program is Matlab.</p>	<ul style="list-style-type: none"> - $\kappa_0 = 0.1, \kappa_1 = 0.35,$ - $\kappa_2 = 0.1, \kappa_3 = 0.2$ - $\kappa_0 = 0.2, \kappa_1 = 0.35,$ - $\kappa_2 = 0.1, \kappa_3 = 0.1$ - $R_{ad} = 1 \mu m,$ - $R_R = 100 nm,$ - $R_L = 100 nm$ - Single pump input signal 	<p>1. Structure</p>  <p>2. Output</p>  <ul style="list-style-type: none"> - The tweezer signal result is generated and controlled, the well width of 16 nm at the 1.5 μm.

2. Multitweezer
 Generation Control
 with a Nanoring
 Resonator System
 [45]

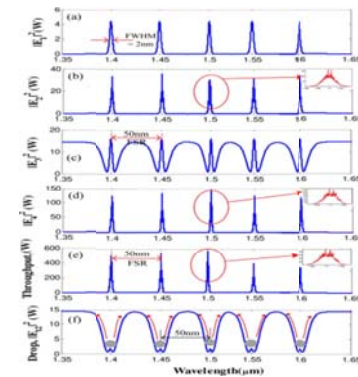
The tweezer signal is the multiplexed result of the dark soliton with bright or Gaussian signals, and then it can control, tune, and amplify within the system. The commercial simulation program is Matlab.

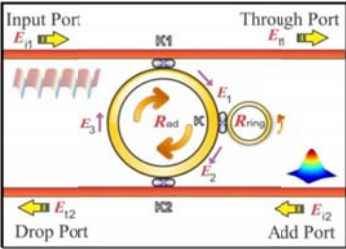
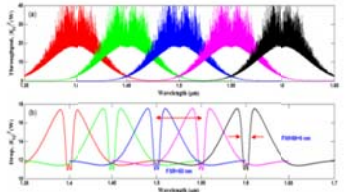
- The optical storage rings are embedded within the add/drop optical filter system, whereas the generated optical signals can be stored and amplified within the design system.
- The difference in time of the first two dynamic wells is 1ns

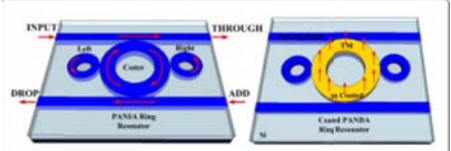
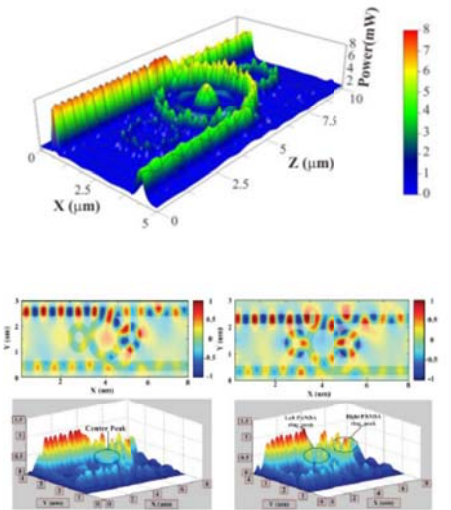
1. Structure

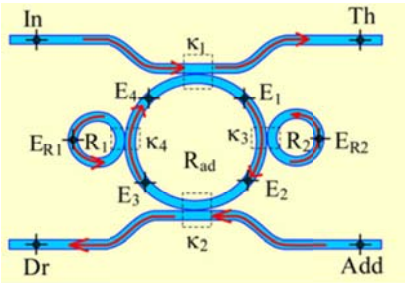
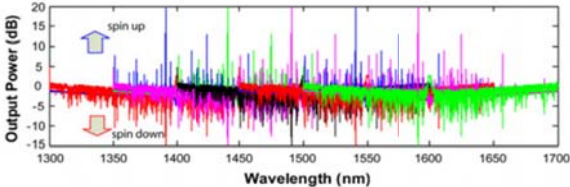
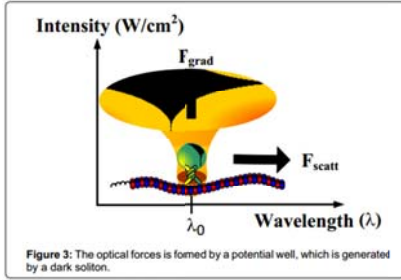


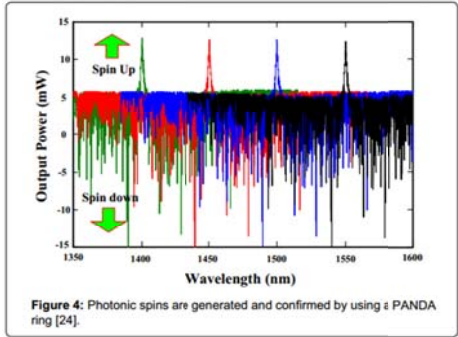
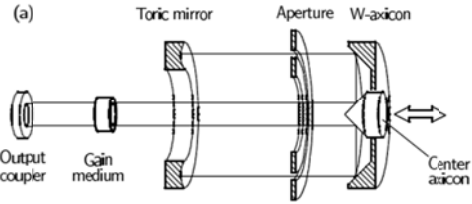
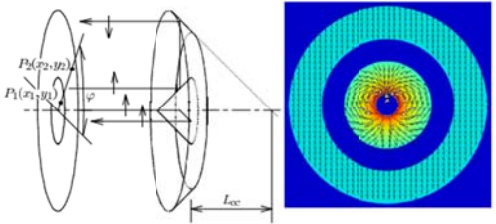
2. Output

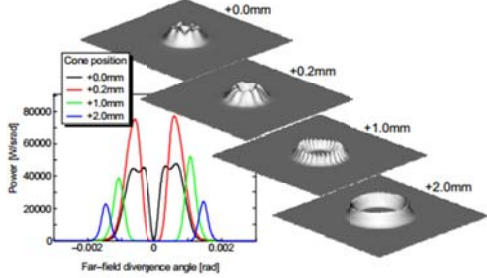
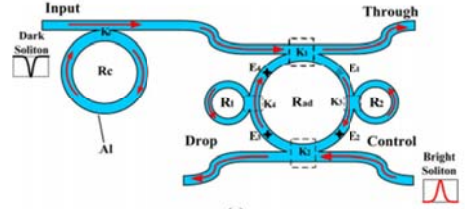
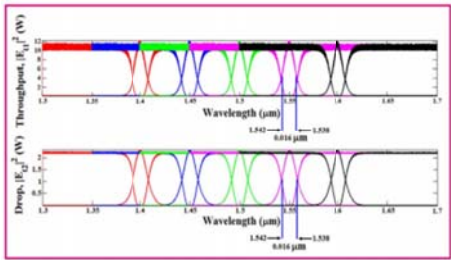


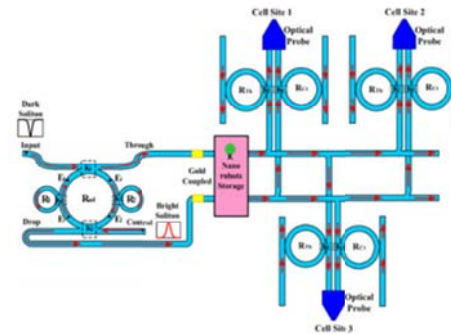
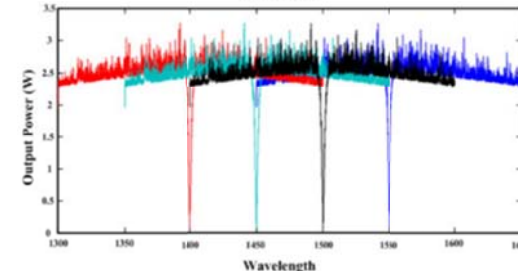
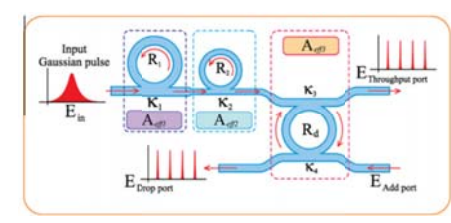
			<ul style="list-style-type: none"> - The advantages are that the dynamic well can be stored and the array of wells can be generated for multiple wells applications. The different in time of the first two dynamic wells of is 1ns.
<p>3. Generation of Nanoscale Optical Tweezers Used for Optical Communication Network [46]</p>	<p>The ultra-short nanometer (nm) optical tweezers are generated using the Half-Panda microring resonator (MRR). The dark soliton is an input pulse for generated tweezer signal. The commercial simulation program is Matlab.</p>	<ul style="list-style-type: none"> - $\kappa_0 = 0.35$, $\kappa_1 = 0.25$ - $R_{ad} = 15 \mu m$, $R_{Ring} = 10 nm$ - $\lambda_0 = 1.40, 1.45, 1.50, 1.55, 1.6 \mu m$ - Material is InGaAsP, $n_0 = 3.4$, $n_2 = 2.5 \times 10^{-17} cm^2 / W$ 	<p>1. Structure</p>  <p>2. Output</p>  <ul style="list-style-type: none"> - The optical tweezers in figure are originated the peaks have FWHM and FSR of 9 nm and 50 nm.
<p>4. Storing and Harvesting</p>	<p>Light pulses are Gaussian, bright or dark solutions that are fed</p>	<ul style="list-style-type: none"> - $\kappa_0 = 0.5$, $\kappa_1 = 0.5$, $\kappa_2 = 0.5$, $\kappa_3 = 0.5$ 	

<p>Atom/Molecule On-Chip: Challenges and Application [47]</p>	<p>into the PANDA system through different ports to generate whispering gallery mode result. The center microring is coated by gold. The commercial simulation program is Optiwave.</p>	<ul style="list-style-type: none"> - $A_{eff} = 0.3 \mu m^2$, - $n_{eff} = 3.14$ - $\gamma = 0.01$ - $\lambda_0 = 1550 nm$ - $R_{ad} = 1.565 \mu m$, - $R_R = R_L = 0.775 \mu m$ 	<p>1. Structure</p>  <p>Figure 1: A conventional PANDA ring planar wave guide was named and designed by Uomwech et al [7] and Gold coated PANDA ring resonator for TM polarized coupling device.</p> <p>2. Output</p> 
<p>5. Optical Spin Generated by a Soliton Pulse in</p>	<p>This paper presented an optical spin generation using Bright and Dark Soliton conversion</p>	<ul style="list-style-type: none"> - $\kappa_1 = \kappa_2 = 0.5$, - $\kappa_3 = \kappa_4 = 0.3$ - $A_{eff} = 0.25 \mu m^2$ 	

<p>an Add-Drop Filter for Optoelectronic and Spintronic Use [48]</p>	<p>behaviors within a PANDA ring resonator. Then the orthogonal solitons are formed and detected at the throughput and drop ports. Under the resonant condition, the Dark and Bright soliton pair's corresponding to the left-hand and right-hand rotating solitons are generated. When a soliton is absorbed by an object, an angular momentum of either + or - is transmitted to the object which originate spin optoelectronic spins.</p>	<ul style="list-style-type: none"> - $n_{eff} = 3.14$ - $\gamma = 0.01$ - $n_2 = 1.3 \times 10^{-13} \text{ cm}^2 / W$ - $\lambda_0 = 1.35, 1.45, 1.50, 1.55, 1.6 \mu m$ 	<p>1. Structure</p>  <p>2. Output</p> 
<p>6. Drug Delivery System Model using Optical Tweezer Spin Control [49]</p>	<p>Dark and bright solitons are input into the system. The orthogonal tweezer is formed within the system and detected simultaneously at the output ports. Under the resonant condition, the optical tweezers generated by dark and bright soliton pair corresponding to the left-hand and</p>	<ul style="list-style-type: none"> - $\kappa_1 : \kappa_2 = 50 : 50, 90 : 10, 10 : 90$ - $\kappa_c = 50 : 50, \kappa_2 = 0.5, \kappa_3 = 0.5$ - $\alpha = 0.1 \text{ dB} / \text{mm}$ - $n_{eff} = 3.14$ - $\gamma = 0.01$ - $\lambda_0 = 1450 \text{ nm}$ 	<p>1. Form of forces</p>  <p>Figure 3: The optical forces is formed by a potential well, which is generated by a dark soliton.</p>

	<p>right-hand rotating solitons. In application, the trapped molecules can be moved and rotated to the required destinations, which can be useful for healthcare applications, especially, in drug delivery, medical diagnosis and therapy. The commercial simulation program is Matlab.</p>	<p>- $R_{ad} = 30 \mu m$, $R_c = 20 \mu m$ $R_R = R_L = 2.5 \mu m$</p>	<p>2. Output</p>  <p>Figure 4: Photonic spins are generated and confirmed by using a PANDA ring [24].</p>
<p>7. Numerical Simulation for an Optical Resonator for Generation of a Doughnut-like Laser Beam [50]</p>	<p>This paper proposed a design of an optical resonator for generation of a doughnut-like laser beam. The resonator consists of a toric mirror, a flat output coupler, and a w-axicon with a movable center axicon. This laser beam is similar to originate of laser sources in TM01 mode.</p>	<p>Different parameter with microring resonator, hence could not compare these parameter.</p>	<p>1. Structure</p>  <p>2. Polarization scrambling of the w-axicon reflector</p> 

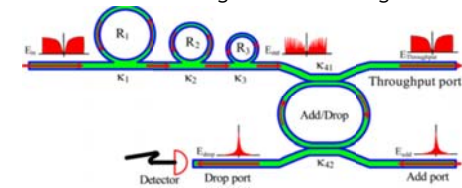
			<p>3. Output</p> 
<p>8. Optical Capsule and Tweezer Array for Molecular Motor Use [51]</p>	<p>Optical capsules and tweezers using a modified optical add-drop is proposed.</p> <p>By using dark and bright solitons, the orthogonal tweezer capsules are formed within the system and observed at the same time at the output ports.</p>	<ul style="list-style-type: none"> - $\kappa_1 : \kappa_2 = 50 : 50, 90 : 10, 10 : 90,$ - $\kappa_c = 50 : 50, \kappa_2 = 0.5, \kappa_3 = 0.5$ - $\alpha = 0.1 dB / mm$ - $n_{eff} = 3.14$ - $\gamma = 0.01$ - $\lambda_0 = 1450 nm$ - $R_{ad} = 30 \mu m,$ - $R_c = 20 \mu m$ - $R_R = R_L = 2.5 \mu m$ 	<p>1. Structure</p>  <p>2. Some output example</p> 
<p>9. Nanorobot Controlled by</p>	<p>This paper proposed the future technique of microsurgery using a</p>	<ul style="list-style-type: none"> - $\kappa_1 : \kappa_2 = 50 : 50, 90 : 10,$ 	

<p>Optical Tweezer Spin Microsurgical Use [52]</p>	<p>nanorobot controlled by light.</p> <p>An optical tweezer is generated by light pulse within a PANDA ring resonator, in which the tweezer spin is introduced by the gold coating material on the optical waveguide for nanorobot trapping and transportation.</p>	<p>10 : 90</p> <ul style="list-style-type: none"> - $\kappa_c = 50 : 50$ - $A_{eff} = 0.25 \mu m^2$ - $\alpha = 0.1 dB / mm$ - $n_{eff} = 3.14$ - $\gamma = 0.01$ - $\lambda_0 = 1450 nm$ - $R_{ad} = 30 \mu m$, $R_{th} = R_{ct} = 18 \mu m$ $R_1 = R_2 = 5 \mu m$ 	<p>1. Structure</p>  <p>2. Output example</p> 
<p>10. Mathematical applications [53]</p>	<p>This paper proposed the light simulation signal using microring resonator system. The design system consists of a nonlinear microring/nanoring resonator system incorporating an add/drop filter. The fabricated material used</p>	<ul style="list-style-type: none"> • Gaussian pulse - $\kappa : 0.55 - 0.90$ - $\alpha = 0.5 dB / mm$ - $n_0 = 3.34$, $n_2 = 2.2 \times 10^{-14} m^2 / W$ $A_{eff} = 0.5, 0.25 \mu m^2$ 	<p>1. Structure of Gaussian generator</p> 

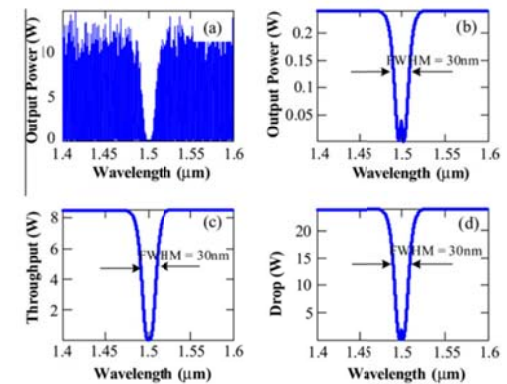
is InGaAsP/InP. Three different forms of input light pulses are Gaussian pulse, dark and bright soliton, whereas the suitable simulation parameters are input power, pulse width, ring radii and the material refractive indices. The commercial simulation program is Matlab.

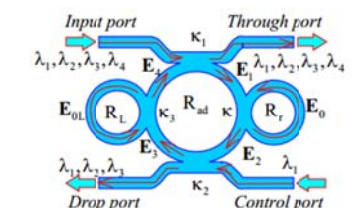
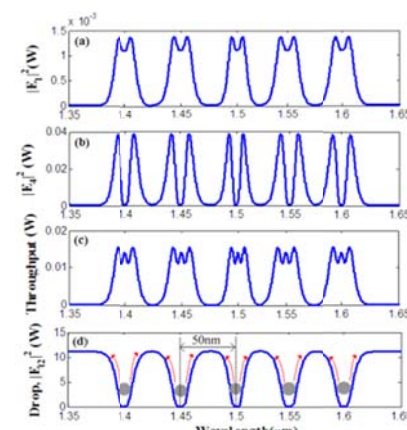
- $\lambda_0 = 400 - 1500 \text{ nm}$
- $R_{ad} = 25 \mu\text{m}$,
- $R_1 = 16 \mu\text{m}$,
- $R_2 = 5 \mu\text{m}$
- Dark Soliton
 - $\kappa : 0.05 - 0.90$
 - $\alpha = 0.5 \text{ dB/mm}$
 - $n_0 = 3.34$,
 - $n_2 = 2.2 \times 10^{-13} \text{ m}^2 / \text{W}$
- $A_{eff} = 0.5, 0.25, 0.1 \mu\text{m}^2$
- $\lambda_0 = 1500 \text{ nm}$
- $R_{ad} = 25 \mu\text{m}$,
- $R_1 = 10 \mu\text{m}$,
- $R_2 = 7 \mu\text{m}, R_2 = 5 \mu\text{m}$
- Bright Soliton
 - $\kappa : 0.10 - 0.90$,
 - $\alpha = 0.5 \text{ dB/mm}$
 - $n_0 = 3.34$,
 - $n_2 = 2.2 \times 10^{-13} \text{ m}^2 / \text{W}$

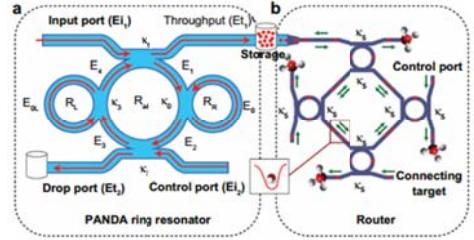
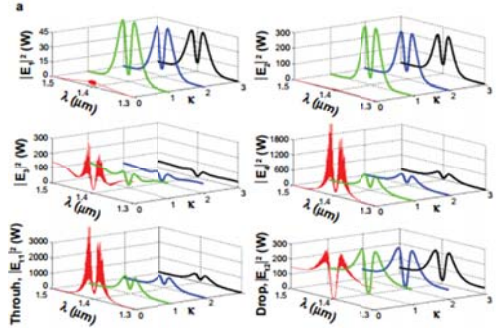
2. Structure of Dark-Bright Solitons generation

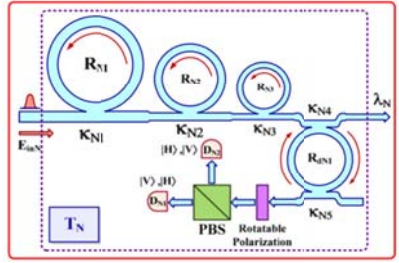
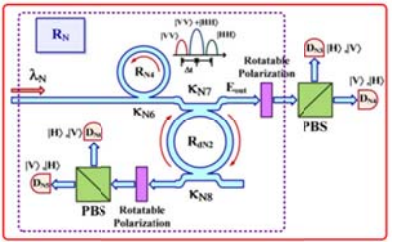
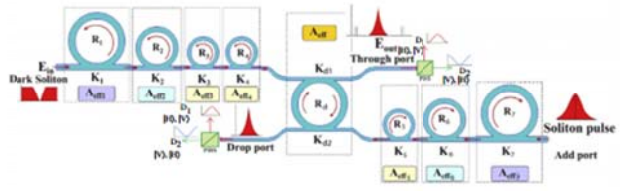


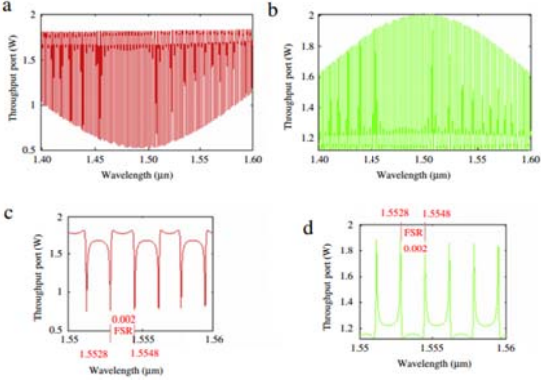
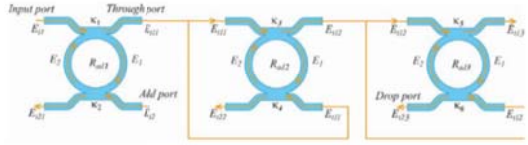
3. Some output example



		<ul style="list-style-type: none"> - $A_{eff} = 0.5, 0.25, 0.1 \mu m^2$ - $\lambda_0 = 1550 \text{ nm}$ - $R_{ad} = 20 \mu m$ - $R_1 = 15 \mu m$, - $R_2 = 10 \mu m$, - $R_3 = 5 \mu m$ 	
<p>11. Optical vortices generated by a PANDA ring resonator for drug trapping and delivery applications [54]</p>	<p>The optical vortices are generated by fed bright soliton at add port of a PANDA. The trapping force is formed by the combination between the gradient field and scattering photons. The commercial simulation program is Matlab.</p>	<ul style="list-style-type: none"> - $\kappa_0 = 0.1, \kappa_1 = 0.35$, - $\kappa_2 = 0.1, \kappa_3 = 0.2$ - $A_{eff} = 0.5, 0.25, 0.25 \mu m^2$ - $\lambda_0 = 1.40, 1.45, 1.50, 1.55, 1.60 \mu m$ - $R_{ad} = 10 \mu m$, - $R_R = R_L = 4 \mu m$ - Single pump input signal 	<p>1. Structure</p>  <p>2. Output</p> 

<p>12. Molecular buffer using a PANDA ring resonator for drug delivery use [43]</p>	<p>This paper proposed the design of molecular buffer for molecule storage and delivery using a PANDA ring resonator. Optical vortices are generated as the same way as optical tweezers. The required molecules are trapped and moved dynamically within the wavelength router network such as molecular buffer. This can be performed within the wavelength router before reaching the required destination. The advantage of the proposed system is that a transmitter and receiver can be formed within the same system, which is available for molecule storage and transportation. The commercial simulation program is Matlab.</p>	<ul style="list-style-type: none"> - $\kappa_0 = 0.5, \kappa_1 = 0.35,$ - $\kappa_2 = 0.1, \kappa_3 = 0.5$ - $A_{eff} = 0.5, 0.25 \mu m^2$ - $\lambda_0 = 1.50 \mu m$ - $P = 2W$ - <i>Pulse width = 35 fs</i> - $R_{ad} = 10, 30 \mu m,$ - $R_r = R_L = 50, 100 nm$ - Single pump input signal 	<p>1. Structure</p>  <p>2. Output</p> 
<p>13. Molecular transporter generation</p>	<p>This paper proposed the system of a quantum-molecular</p>	<ul style="list-style-type: none"> - $\gamma = 0.1,$ - $\alpha = 0.5 dB/mm$ 	

<p>for quantum-molecular transmission via an optical transmission line [55]</p>	<p>trans-portion using the multi-optical Tweezers. The generated transporter is formed by a dark soliton. It can be tuned and attenuated to a single photon by bright soliton control and transmitted into an optical link. The design system consists of a nonlinear microring/nanoring resonator system incorporating an add/drop filter and a quantum signal processor.</p>	<ul style="list-style-type: none"> - $n_0 = 3.34$, - $n_2 = 2.2 \times 10^{-13} \text{ m}^2 / W$ - $A_{eff} = 0.5, 0.25, 0.1 \mu\text{m}^2$ - $\lambda_0 = 1500 \text{ nm}$ - $R_{ad} = 20 \mu\text{m}$, - $R_1 = 10 \mu\text{m}$ $R_2 = 7 \mu\text{m}$, - $R_2 = 5 \mu\text{m}$ 	<p>1. Transmission Unit</p>  <p>2. Receiver Unit</p> 
<p>14. Multi-variable quantum tweezers generation using photon entanglement [56]</p>	<p>This paper presented the multi-quantum tweezers array generation using Dark-bright Solitons generation control within the multi-microring resonator system. By using the quantum processor, the entangle photon states of the tweezers can be</p>	<p>The multi-quantum tweezers can be controlled and tuned by varying the couple coefficient (κ) between 0.1 and 0.9, with ring resonator radii between 10 and 20 μm. The</p>	<p>1. Structure</p> 

	<p>formed, which is allowed to form the molecular quantum transmission.</p>	<p>parameters are</p> <ul style="list-style-type: none"> - $\kappa_1 = 0.9713$, - $\kappa_2 = 0.9723, \kappa_2 = 0.9768$ - $\kappa_3 = 0.9768$ - $\lambda_0 = 1.50 \mu m$ - $R_1 = 12 \mu m$, - $R_2 = 11.5 \mu m$, - $R_3 = R_4 = 10 \mu m$ - $R_d = 50 \mu m$, - $\kappa_{d1} = \kappa_{d2} = 0.5$ 	<p>2. Some output example</p> 
<p>15. Novel Multi Optical Trapping Tool Generation within Add/Drop Filter System Controlled by Light [57]</p>	<p>This paper presented optical trapping tool using add/drop filter system. Bright Soliton is fed to input port of add/drop filter and then multiplexing signals with different wavelengths are controlled and tuned similar to optical tweezers.</p>	<ul style="list-style-type: none"> - $\kappa_1 = 0.9$ - $\kappa_2 = 0.5$ - $\kappa_2 = 0.9$ - $\kappa_3 = 0.38$ - $\kappa_5 = 0.9$ - $\kappa_6 = 0.38$ - $R_{ad1} = 300 \mu m$ - $R_{ad2} = 300 \mu m$ - $R_{ad3} = 300 \mu m$ 	<p>1. Structure</p> 

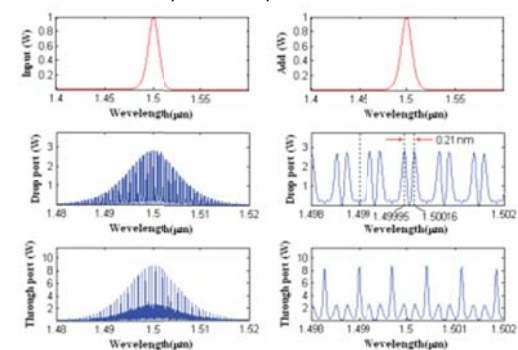
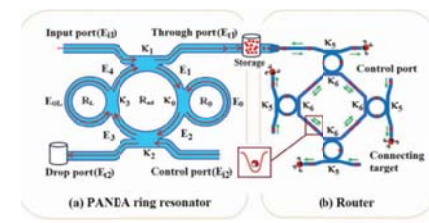
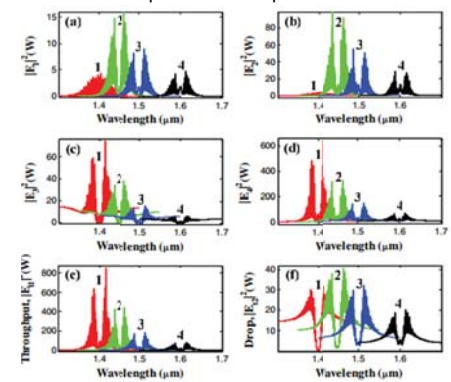
			<p>2. Some example output</p> 
<p>16. Drug Trapping and Delivery Using a PANDA Ring Resonator [58]</p>	<p>This paper proposed drug delivery system by using a PANDA ring resonator to form and transmit and receive the microscopic volume by controlling some suitable ring parameters.</p>	<ul style="list-style-type: none"> - $\kappa_1 = 0.1, \kappa_2 = 0.35,$ - $\kappa_2 = 0.1, \kappa_3 = 0.2$ - $\lambda_0 = 1.40, 1.45, 1.50, 1.55, 1.60 \mu\text{m}$ - $R_{ad} = 1 \mu\text{m},$ - $R_R = 100 \text{ nm},$ - $R_L = 100 \text{ nm}$ 	<p>1. Structure</p>  <p>2. Some output example</p> 

Table 2.5 Compare the different functional

Feature	Reference Number																		
	13	14	15	16	44	45	46	47	48	49	50	51	52	53	54	55	56	57	58
Fabrication (F) or Simulation (S)	F	S	F	S	S	S	S	S	S	S	S	S	S	S	S	S	S	S	S
Transfer function	x	✓	x	✓	✓	-	✓	x	x	x	x	x	x	✓	✓	✓	✓	✓	✓
Evaluated suitable parameters Process	x	✓	x	x	x	-	x	x	x	x	x	x	x	x	x	x	x	x	x
Depth of well	✓	x	✓	✓	x	-	x	x	x	x	x	x	x	x	x	x	x	x	x
Width of well	✓	x	✓	✓	✓	-	x	x	x	x	x	x	x	x	x	x	x	x	✓
Force calculation or measurement	✓	x	x	x	x	-	x	x	x	x	x	x	x	x	x	x	x	x	x
Velocity calculation or measurement	✓	x	✓	x	x	-	x	x	x	x	x	x	x	x	x	x	x	x	x

From the Table 2.5, although many researches about optical tweezers generation, the suitable parameters in specification process which investigates the effects on output signals have rarely been discussed. The investigated parameters are the refractive index of material, the intensity coupling coefficients, the ring radius size and the center wavelength of input signal. Moreover, for the optical output (tweezers) properties such as the depth of well, the width of well, the force calculation or measurement and the velocity calculation or measurements lack explained information. Therefore, this thesis proposes the design of tweezer generators using MCADM and then simulates the effects of investigated parameters to specify the suitable trapping parameters. After that, the forces and velocity are evaluated. Finally, the optical tweezers properties are evaluated.

2.7 Summary

For the overall understanding of the proposed system from the beginning to end of the tweezer generation process, the basic theory of optical tweezer is required. By the Gaussian and Dark Soliton, signals are inputs to microring resonators device and are modulated within device by cross-phase modulation technique explained by the proposed mathematical transfer function in chapter 3.

Chapter 3

The Design of Tweezer Generators using Modified Circular Add-Drop Modulator

This chapter is divided into 4 sections comprised of the MCADM design process, the proposed mathematical transfer function for describing the optical tweezer signals at throughput and drop ports, the characteristics and results analysis, which explains and shows the results of transfer function testing by four parameters: intensity coupling coefficient, ring radius size, material and center wavelength. Finally, constraint of the problem and the design of tweezer and generators using MCADM is proposed.

3.1 The Studied Process of MCADM Design

In order to design the MCADM for molecular trapping and manipulation the knowledge about optical tweezer theory [1, 17] that is mentioned in section 2.1 essential to understand the interaction between forces and the trapped particle. The radiation pressure force (F) from laser light can be divided into gradient (F_{grad}) and scattering force (F_{scatt}). The scattering force is a result of percussion between photon and particle in the propagation direction of the incident laser light and proportional to the intensity. The gradient force is originated by a difference in pressure across a surface in a perpendicular direction with the incident laser light. The stability of optical trapping occurs when the magnitude of gradient force is greater than scattering force ($F_{grad} > F_{scatt}$), while the particle velocity arises under the condition of the summation of force (F_{net}) between gradient and scattering force is higher than the viscosity (F_{vis}) or friction force (F_{fric}). The next issue is the molecular properties [17], and the suitable light properties and size are important for force calculation. Within the criterion in Equation (2.6), this thesis focuses on the Rayleigh regime ($X \ll 1$). In other word, the size of the particle is smaller than the center wavelength of the input signal. Usually, the polystyrene particle [15] is used to test and measurement the results because of its advantages of varying size of particle, suitable light property ($n_p = 1.47$) and available. Finally, the very important issue for describing the characteristics of the optical tweezer signal (output waveform, depth of well, width of well, net force, carrier capacity and velocity) is a realistic mathematical transfer function proposed in section 3.2. The MCADM design process can be summarized as follows:

- I. Study MCADM properties that affect the optical tweezer characteristics such as output waveform, width of well, depth of well, net force, carrier capacity of trapping tool and velocity.
- II. Study and improve mathematical transfer function to explain the realistic characteristic of optical tweezer in (I) and use this transfer function to test the resulting effect.
- III. Define constraints of problem for solving such as the molecular size and velocity.
- IV. Choose the suitable parameters of MCADM which correspond with constraints of problem in (III) and testing results in (II).
- V. Propose the system with the suitable parameters and validation by our simulation results in Chapter 4.

3.2 The Proposed Mathematical Transfer Function

There are 4 parameters that affect optical tweezer characteristics which consist of the intensity coupling coefficient (κ_1, κ_3), ring radius size (R_{ad}, R_R, R_L), fabricated material and center wavelength (λ_0) of the input signal. The effected optical tweezer characteristics are output waveform, width of well, depth of well, net force, carrier capacity of trapping tool and velocity. This section presents new mathematical transfer function. The optical tweezer characteristics are analyzed and proposed.

3.2.1 The Proposed Mathematical Transfer Function

According to our investigation of MCADM of previous work [16], it found that there are some errors in transfer function used to describe the characteristics of the optical tweezer signal at the throughput and drop ports. On the Equations (2.23) to (2.26) which describe the characteristic of light field (electrical field) at the positions $E_1 - E_4$ in figure 2.16, and it is found that they disregard to consider the term of signal which the light coupling into the small left R_L and right R_R microring resonator. Those equations use only the term of $e^{-\frac{\alpha}{2} \frac{L}{2} - jk_n \frac{L}{2}}$ that means only the signal of center perimeter (R_{ad}) is calculated for tweezer signal generations. By this reason, this thesis proposes the new mathematical transfer function to explain the realistic optical tweezer signal at throughput and drop ports. Given E_{i1} and E_{i2} are an input into input and add ports of MCADM respectively. When the input light pulse pass through the first coupler of the MCADM system, the transmitted and circulated components can be written as

$$E_{t1} = \sqrt{1 - \gamma_1} \left[\sqrt{1 - \kappa_1} E_{i1} + j\sqrt{\kappa_1} E_4 e^{\frac{-\alpha L_{ad}}{2.4} - jk_n \frac{L_{ad}}{4}} \right] \quad (3.1)$$

$$E_1 = \sqrt{1-\gamma_1} \left[\sqrt{1-\kappa_1} E_4 e^{\frac{-\alpha.L_{ad}-jk_n.L_{ad}}{2.2}} + j\sqrt{\kappa_1} E_{i1} e^{\frac{-\alpha.L_{ad}-jk_n.L_{ad}}{2.4}} \right] \quad (3.2)$$

$$E_2 = \sqrt{1-\gamma_3} \left(\sqrt{1-K_3} \cdot E_1 + j\sqrt{K_3} \cdot E_{R2} \right) \quad (3.3)$$

where κ_1 and γ_1 are the intensity coupling coefficient and the fractional coupler intensity loss of the add-drop optical filter, respectively. α is the attenuation coefficient, $k_n = 2\pi/\lambda$ is the wave propagation number, λ is the input wavelength light field and $L = 2\pi R_{ad}$, R_{ad} is the radius of add-drop (center ring radius) device.

For the second coupler of the MCADM system can be described as

$$E_{i2} = \sqrt{1-\gamma_2} \left[\sqrt{1-\kappa_2} E_{i2} + j\sqrt{\kappa_2} E_2 e^{\frac{-\alpha.L_{ad}-jk_n.L_{ad}}{2.4}} \right] \quad (3.4)$$

$$E_3 = \sqrt{1-\gamma_2} \left[\sqrt{1-\kappa_2} E_2 e^{\frac{-\alpha.L_{ad}-jk_n.L_{ad}}{2.2}} + j\sqrt{\kappa_2} E_{i2} e^{\frac{-\alpha.L_{ad}-jk_n.L_{ad}}{2.4}} \right] \quad (3.5)$$

$$E_4 = \sqrt{1-\gamma_4} \left(\sqrt{1-\kappa_4} E_3 + j\sqrt{\kappa_4} E_{R1} \right) \quad (3.6)$$

where κ_2 is the intensity coupling coefficient, γ_2 is the fractional coupler intensity loss. The circulated light fields, E_{R1} and E_{R2} are the light field circulated components of the microring radii, R_L and R_R which coupled into the left and right sides of the MCADM system respectively. The light field transmitted and circulated components in the right microring, R_r , are given by

$$E_{R1} = \frac{j(\sqrt{1-r_2} \cdot \sqrt{k_2}) E_1}{(1-\sqrt{1-r_2})(\sqrt{1-k_2} e^{\frac{-\alpha}{2} L_R - jk_n L_R})} \quad (3.7)$$

$$E_{R2} = E_{R21} e^{\frac{-\alpha}{2} L_R - jk_n L_R} \quad (3.8)$$

$$E_{R21} = \sqrt{1-\gamma_3} \left[\sqrt{1-\kappa_3} E_{R2} + j\sqrt{\kappa_3} E_1 \right] \quad (3.9)$$

where κ_3 and γ_3 are the intensity coupling coefficient and the fractional coupler intensity loss of the right microring, respectively. α is the attenuation

coefficient, $k_n = 2\pi/\lambda$ is the wave propagation number, λ is the input wavelength light field and $L_2 = 2\pi R_r$, R_r is the radius of right microring.

From Equations (3.8) to (3.9), the circulated roundtrip light fields of the right microring radii, R_r , are given in Equations (3.10) and (3.11) respectively.

$$E_{R21} = \frac{j\sqrt{1-\gamma_3}\sqrt{\kappa_3}E_1}{1-\sqrt{1-\gamma_3}\sqrt{1-\kappa_3}e^{-\frac{\alpha}{2}L_R-jk_nL_R}} \quad (3.10)$$

$$E_{R2} = \frac{j\sqrt{1-\gamma_3}\sqrt{\kappa_3}E_1e^{-\frac{\alpha}{2}L_R-jk_nL_R}}{1-\sqrt{1-\gamma_3}\sqrt{1-\kappa_3}e^{-\frac{\alpha}{2}L_R-jk_nL_R}} \quad (3.11)$$

Thus, the output circulated light field of E_{R2} , for the right microring is given by

$$E_2 = E_1 \left\{ \frac{\sqrt{(1-\gamma_3)(1-\kappa_3)} - (1-\gamma_3)(1-\kappa_3)e^{-\frac{\alpha}{2}L_R-jk_nL_R} - (1-\gamma_3)(\kappa_3)e^{-\frac{\alpha}{2}L_R-jk_nL_R}}{1-\sqrt{(1-\gamma_3)(1-\kappa_3)}e^{-\frac{\alpha}{2}L_R-jk_nL_R}} \right\} \quad (3.12)$$

Similarly, the output circulated light field of E_{R1} , for the left microring at the left side of the MCADM system is given by

$$E_4 = E_3 \left\{ \frac{\sqrt{(1-\gamma_4)(1-\kappa_4)} - (1-\gamma_4)(1-\kappa_4)e^{-\frac{\alpha}{2}L_L-jk_nL_L} - (1-\gamma_4)(\kappa_4)e^{-\frac{\alpha}{2}L_L-jk_nL_L}}{1-\sqrt{(1-\gamma_4)(1-\kappa_4)}e^{-\frac{\alpha}{2}L_L-jk_nL_L}} \right\} \quad (3.13)$$

where κ_4 is the intensity coupling coefficient, γ_4 is the fractional coupler intensity loss, α is the attenuation coefficient, $k_n = 2\pi/\lambda$ is the wave propagation number, λ is the input wavelength light field and $L_L = 2\pi R_L$, R_L is the radius of left microring.

From Equations (3.1) to (3.13), the circulated light fields, E_1 , E_3 and E_4 are defined as Equations (3.14) to (3.18) by the constant parameters which are given as:

$$x_1 = \sqrt{I-\gamma_1} \quad , \quad y_1 = \sqrt{I-\kappa_1} \quad , \quad z_1 = \sqrt{\kappa_1}$$

$$x_2 = \sqrt{I-\gamma_2} \quad , \quad y_2 = \sqrt{I-\kappa_2} \quad , \quad z_2 = \sqrt{\kappa_2}$$

$$x_3 = \sqrt{I-\gamma_3} \quad , \quad y_3 = \sqrt{I-\kappa_3} \quad , \quad z_3 = \sqrt{\kappa_3}$$

$$x_4 = \sqrt{I - \gamma_4} \quad , \quad y_4 = \sqrt{I - \kappa_4} \quad , \quad z_4 = \sqrt{\kappa_4}$$

$$P_1 = e^{-\frac{a}{2}L_R - jk_n L_R} \quad , \quad P_2 = e^{-\frac{a}{2}L_L - jk_n L_L} \quad , \quad L_R = 2pR_R \quad , \quad L_L = 2pR_L$$

$$A = (x_1 z_1 P L_8 - x_1 z_1 x_2 y_2 P_1 P L_8 - x_1 z_1 x_4 y_4 P_2 P L_8 + x_1 z_1 x_2 y_2 x_4 y_4 P_1 P_2 P L_8)$$

$$B = (x_1 y_1 x_3 z_3 x_4 y_4 P L_4 P L_8 - x_1 y_1 x_2 y_2 x_3 z_3 x_4 y_4 P_1 P L_4 P L_8 - x_1 y_1 x_3 z_3 x_4^2 y_4^2 P_2 P L_4 P L_8 \\ + x_1 y_1 x_2 y_2 x_3 z_3 x_4^2 y_4^2 P_1 P_2 P L_8 P L_4 - x_1 y_1 x_3 z_3 x_4^2 z_4^2 P_2 P L_4 P L_8 + x_1 y_1 x_2 y_2 x_3 z_3 x_4^2 z_4^2 P_1 P_2 P L_4 P L_8)$$

$$C = \left[\begin{array}{l} x_1 y_1 x_2 y_2 x_3 y_3 x_4 y_4 (P L_4)^2 - x_1 y_1 x_2^2 y_2^2 x_3 y_3 x_4 y_4 P_1 (P L_4)^2 - x_1 y_1 x_2^2 z_2^2 x_3 y_3 x_4 y_4 P_1 (P L_4)^2 \\ - x_1 y_1 x_2 y_2 x_3 y_3 x_4^2 y_4^2 P_2 (P L_4)^2 + x_1 y_1 x_2^2 y_2^2 x_3 y_3 x_4^2 y_4^2 P_1 P_2 (P L_4)^2 \\ + x_1 y_1 x_2^2 z_2^2 x_3 y_3 x_4^2 y_4^2 P_1 P_2 (P L_4)^2 - x_1 y_1 x_2 y_2 x_3 y_3 x_4^2 z_4^2 P_2 (P L_4)^2 \\ + x_1 y_1 x_2^2 y_2^2 x_3 y_3 x_4^2 z_4^2 P_1 P_2 (P L_4)^2 + x_1 y_1 x_2^2 z_2^2 x_3 y_3 x_4^2 z_4^2 P_1 P_2 (P L_4)^2 \end{array} \right]$$

$$F = I - x_2 y_2 P_1 - x_4 y_4 P_2 + x_2 y_2 x_4 y_4 P_1 P_2 \quad , \quad G = x_1 y_1 - x_1 x_4 y_1 y_4 P_2$$

$$H = j \left[\begin{array}{l} x_1 x_2 x_3 x_4 y_2 y_3 y_4 z_1 \cdot P L_4 P L_8 - x_4^2 y_4^2 x_1 x_2 x_3 y_2 y_3 z_1 \cdot P_2 P L_4 P L_8 - x_4^2 z_4^2 x_1 x_2 x_3 y_2 y_3 z_1 \cdot P_2 P L_4 P L_8 \\ - x_2^2 y_2^2 x_1 x_3 x_4 y_3 y_4 z_1 \cdot P_1 P L_4 P L_8 + x_2^2 x_4^2 y_2^2 y_4^2 x_1 x_3 y_3 z_1 \cdot P_1 P_2 P L_4 P L_8 \\ + x_2^2 x_4^2 y_2^2 z_4^2 x_1 x_3 y_3 z_1 \cdot P_1 P_2 \cdot P L_4 P L_8 - x_2^2 z_2^2 x_1 x_4 x_3 y_3 y_4 z_1 \cdot P_1 P L_4 P L_8 \\ + x_2^2 x_4^2 z_2^2 y_4^2 x_1 x_3 y_3 z_1 \cdot P_1 P_2 P L_4 P L_8 + x_2^2 x_4^2 z_2^2 z_4^2 x_1 x_3 y_3 z_1 \cdot P_1 P_2 P L_4 P L_8 \end{array} \right]$$

$$I = (-) \left[\begin{array}{l} x_1 x_3 x_4 y_4 z_1 z_3 P L_8^2 - x_4^2 y_4^2 x_1 x_3 z_1 z_3 P_2 P L_8^2 - x_4^2 z_4^2 x_1 x_3 z_1 z_3 P_2 P L_8^2 \\ - x_1 x_2 x_3 x_4 z_1 z_3 y_2 y_4 P_1 P L_8^2 + x_4^2 y_4^2 x_1 x_2 x_3 y_2 z_1 z_3 P_1 P_2 P L_8^2 \\ + x_4^2 z_4^2 x_1 x_2 x_3 y_2 z_1 z_3 P_1 P_2 P L_8^2 \end{array} \right]$$

$$J = I - x_4 y_4 P_2 \quad , \quad K = x_3 y_3 (I - x_2 y_2 P_1) \quad , \quad L = x_2 x_3 y_2 z_3 P L_8 - x_2^2 y_2^2 x_3 z_3 P_1 P L_8 - x_2^2 z_2^2 x_3 z_3 P_1 P L_8$$

$$M = (I - x_2 y_2 P_1)$$

$$E_1 = j \left(\frac{A \cdot E_{i_1} + B \cdot E_{i_2}}{F - C} \right) \quad (3.14)$$

$$E_2 = \left[\frac{x_2 y_2 - x_2^2 y_2^2 P_1 - x_2^2 z_2^2 P_1}{I - x_2 y_2 P_1} \right] E_1 \quad (3.15)$$

$$E_3 = \left[\frac{(x_2 y_2 x_3 y_3 P L_4 - x_2^2 y_2^2 x_3 y_3 P L_4 P_1 - x_2^2 z_2^2 x_3 y_3 P L_4 P_1) E_1 + j(x_3 z_3 P L_8 - x_2 y_2 x_3 z_3 P L_8 P_1) E_{i_2}}{I - x_2 y_2 P_1} \right] E_{i_2} \quad (3.16)$$

$$E_4 = \left[\frac{x_4 y_4 - x_4^2 y_4^2 P_2 - x_4^2 z_4^2 P_2}{I - x_4 y_4 P_2} \right] E_3 \quad (3.17)$$

Thus, from Equations (3.1), (3.3), (3.14)-(3.17), the output optical field of the through port (E_{t1}) is expressed by

$$E_{th} = \left[\frac{G.F^2 - G.F.C - A.H.J}{F^2 . J - C.F.J} \right] E_{i_1} + \left[\frac{(F.I - B.H - C.I)}{F.(F - C)} \right] E_{i_2} \quad (3.18)$$

The power output of the through port (P_{t1}) is written by

$$P_{t1} = (E_{t1}) \cdot (E_{t1})^* = \left| x_1 y_1 E_{i_1} + \left(j x_1 x_2 y_2 \sqrt{\kappa_1} E_{R2} E_{R1} E_1 - x_1 x_2 \sqrt{\kappa_1 \kappa_2} E_{R1} E_{i_2} \right) e^{-\frac{\alpha L_{ad}}{4} - j k_n \frac{L_{ad}}{4}} \right|^2 \quad (3.19)$$

Similarly, from Equations (3.3), (3.4), (3.14)-(3.17), the output optical field of the drop port (E_{t2}) is given by

$$E_{drop} = \frac{K \left(F - C - \frac{BL}{K} \right) E_{i_2} - L.A.E_{i_1}}{M (F - C)} \quad (3.20)$$

The power output of the drop port (P_{t2}) is expressed by

$$P_{t2} = (E_{t2}) \cdot (E_{t2})^* = \left| x_2 y_2 E_{i_2} + j x_2 \sqrt{\kappa_2} E_{R2} E_1 e^{-\frac{\alpha L_{ad}}{4} - j k_n \frac{L_{ad}}{4}} \right|^2 \quad (3.21)$$

In order to retrieve the required signals, the author proposes to use an MCADM device with the appropriate parameters. This is given in the following details. The optical circuits of a MCADM for the through port and drop port can be given by Equations (3.19) and (3.21) respectively. The chaotic noise cancellation can be managed by using the specific parameters of a MCADM device, and the required signals can be retrieved by the specific users. κ_1 and κ_2 are the coupling coefficients of a MCADM device, $k_n = 2\pi / \lambda$ is the wave propagation number for in a vacuum, and the waveguide (ring resonator) loss is $\alpha = 5 \times 10^{-5}$ dB/mm. The fractional coupler intensity loss is $\gamma = 0.01$. In the case of a MCADM device, the nonlinear refractive

index is neglected. By adding term of light coupling in to the small right R_R , it affects the electrical field signal of E_2 in Equation (3.12) while and left R_L microring resonator affects the electrical field signal of E_4 in Equation (3.13). Then the effect will extend to the electrical signal of throughput (E_{th}) and drop (E_d) ports in Equations (3.17) and (3.19). Finally, by adding two terms will produce the finely tweezer signals at throughput (P_{t1}) and drop (P_{t2}) ports in Equations (3.18) and (3.20). The adding term of light coupling R_R and R_L affects both increasing and decreasing in all electrical signals (E_2, E_4, E_{th}, E_d) upon the additive or subtractive interference of microring resonator. If the ring radius sizes are increasing, then the numbers of resonant mode within ring are increasing. Consequently, the width of well of the output signal is decreasing. If the ring radius size is decreasing, the width of well is increasing.

3.3 Characteristics and Results Analysis of MCADM

After improving mathematical transfer function for describing the optical tweezer characteristics, the next issue is the parameter test for studying the effect of output waveform signal. This section will use the parameters analyzed in section 3.2 for test these effects. The investigated parameters are intensity coupling coefficient (κ_1, κ_3), ring radius size (R_{ad}, R_R, R_L), fabricated material and center wavelength (λ_0) of the input signal. The effected characteristics results are depth of well, width of well, free spectral range (FSR) and velocity.

3.3.1 Intensity Coupling Coefficient

The intensity coupling coefficient or kappa (κ_1, κ_3) is the ratio of coupling light signal into the microring to form and generate additive and subtractive interference (on-off resonance) within each microring. For the reason of systematic balance, the intensity coupling coefficient of κ_2, κ_4 is assigned to 0.35. In addition, the nonlinear property of MCADM allows the cross-phase modulation between Gaussian and Dark Soliton signals that produce the optical tweezer output at throughput and drop ports. Typically, the ratio of the intensity coupling coefficient varies from 0 to 1 while the other parameters are fixed. The objective of the study is the investigation of intensity coupling coefficient, which affects optical tweezer results at throughput and drop ports. The effected results can be summarized in Table 3.1. The blue highlight in Tables 3.1-3.4 demonstrates the suitable parameter value for a constrained problem.

Table 3.1 The effects of the intensity coupling coefficients on optical tweezer signal

Intensity Coupling Coefficient		Depth of well (dB)	Width of well (nm)	FSR (nm)	Velocity ($\mu\text{m/s}$)
κ_1	κ_3				
0.55	0.45	0.50	2	12	220.5
0.60	0.40	0.62	2	12	182.1
0.65	0.35	0.76	2	12	145.5
0.70	0.30	0.94	2	12	111.1
0.75	0.25	1.17	2	12	79.49
0.80	0.20	1.49	2	12	51.15
0.85	0.15	1.96	2	12	27.06
0.90	0.10	2.88	2	12	8.794
0.95	0.05	8.16	0.3	12	0.033

The results in Table 3.1 show that the variation of κ_1 and κ_3 are related to the depth of well (magnitude of gradient force) and the velocity will decrease proportion to the increasing of κ_1 . About the width of well and FSR, they are almost constant. The blue highlight in Table 3.1 demonstrates the suitable parameter value for a 2 nm polystyrene particle which is trapped and manipulated with $\approx 8 \mu\text{m/s}$ of velocity.

3.3.2 Ring Radius Size

Normally, ring radius of MCADM is designed upon free spectral range (FSR) or mode of resonance in the microring which the total FSR can be described as

$$FSR_{total} = N_c FSR_c = N_R FSR_R = N_L FSR_L \quad (3.1)$$

where N_i the numbers of resonance mode, subscript c is represented central microring, subscript R is represented right mirroring, subscript L is represent left microring, FSR can be determined by the relationship of group velocity (n_g), speed of light (c) and waveguide length (L) as

$$FSR = \frac{c}{n_g L} \quad (3.2)$$

Substitution Equation (3.2) into Equation (3.1), so that

$$N_c \frac{c}{n_g L_c} = N_R \frac{c}{n_g L_R} = N_L \frac{c}{n_g L_L} \quad (3.3)$$

Therefore, the number of resonance mode corresponds with

$$\frac{N_c}{N_R} = \frac{L_c}{L_R} = \frac{R_c}{R_R} = \frac{R_c}{R_L} \quad (3.4)$$

where R_i is a radius of microring, subscript $i=c$ is represented center microring, subscript $i=L$ is represent left microring and subscript $i=R$ is represented right microring. From the Equations (3.1) to (3.4) indicated that FSR is proportional with the ring radius size while the numbers of resonance mode is a direct variation in ring radius size. The objective of the study is the investigation of the ring radius size, which affect optical tweezer results at throughput and drop ports. Usually, the ring radius sizes are varying from 2 to 20 μm while the other parameters are fixed. The fabricated ring radius size is explored from several researches in section 2.5 (Table 2.2). The effected results can be summarized in Table 3.2.

Table 3.2 The effects of the ring radius size on optical tweezer signal

Ring Radius Size		Depth of well (dB)	Width of well (nm)	FSR (nm)	Velocity ($\mu\text{m/s}$)
R_{ad}	$R_R = R_L$				
2	1	2.36	12	41	12.11
4	2	2.49	6	58	11.74
6	3	2.51	5	38	12.22
8	4	2.43	3	28	13.27
10	5	2.57	3	23	12.23
12	6	2.53	3	18	12.52
14	7	2.56	3	17	12.23
16	8	2.71	2	15	10.64
18	9	2.54	2	13	12.24
20	10	2.88	2	12	8.794

From Table 3.2, it shows that the increased variation of ring radius size is directly proportional to the increase in depth of well, while the width of well and

FSR is proportional to the increase of ring radius which relates to the analysis of Equations (3.1) to (3.4). The increasing of ring radius size is insignificant for velocity. For the blue highlight in Table 3.2 demonstrates the suitable parameter value for a 2 nm polystyrene particle is trapped and manipulated with $\approx 8 \mu\text{m/s}$ of velocity.

3.3.3 Fabricated Material

The effective index (n_{eff}) of material is effect with nonlinear properties of fabricated waveguide and also effect to MCADM fabrication. One of nonlinear properties is the effective index which depends on the intensity with respect to the time. The effective index of material can be described as

$$n_{eff} = n_0 + n_2 I \quad (3.5)$$

Where n_0 is the linear refractive index of materials, n_2 represents the nonlinear refractive index of material and I is the intensity. In additional, the numbers of the resonance mode (N) is directly proportional with the effective index of material.

$$N = \frac{2\pi r n_{eff}}{\lambda} \quad (3.6)$$

Where r is a ring radius size and λ is the center wavelength of the input. The fabricated microring resonator is explored during a past decade as shown in section 2.4 (Table 2.1). The popular materials for microring resonator fabrication are varying from InGaAsP, AlGaAs, Ta₂O₅, SiN and SiO₂ while the other parameters are fixed. The objective of the study is the investigation of the fabricated material which affects optical tweezer results at throughput and drop ports. The effected results can be summarized in Table 3.3.

Table 3.3 The effects of the fabricated materials on optical tweezer signal

Fabricated Material	Depth of well (dB)	Width of well (nm)	FSR (nm)	Velocity($\mu\text{m/s}$)
InGaAsP	2.88	2	12	8.794
AlGaAs	2.49	1	12	12.69
Ta ₂ O ₅	2.50	1	17	12.75
SiN	2.50	1	17	12.74
SiO ₂	2.41	3	25	13.2

From the results in Table 3.3 and mathematical analyses in Equation (3.6) by using the information of material properties in Table 2.1, it indicated that increasing of the depth of well is a directly proportional to the refractive index of material while FSR and velocity are decreasing. For the blue highlight in Table 3.3, it demonstrates that the suitable parameter value for a 2 nm polystyrene particle is trapped and manipulated with $\approx 8 \mu\text{m/s}$ of velocity.

3.3.4 Center Wavelength

From the mathematical transfer function analysis, the center wavelength of the input signal is affected by the optical tweezer characteristics. According to the Equation (3.6), it indicates that the number of the resonance mode (N) is proportional to the input center wavelength (λ). Therefore, the objective of the study is the variation of input center wavelengths which affects optical tweezer results at throughput and drop ports. Commonly, the input center wavelength (λ) is varying from 700 to 1,700 nm that is corresponding with the frequency range in optical communication [42], the other parameters are fixed. The effected results can be summarized in Table 3.4.

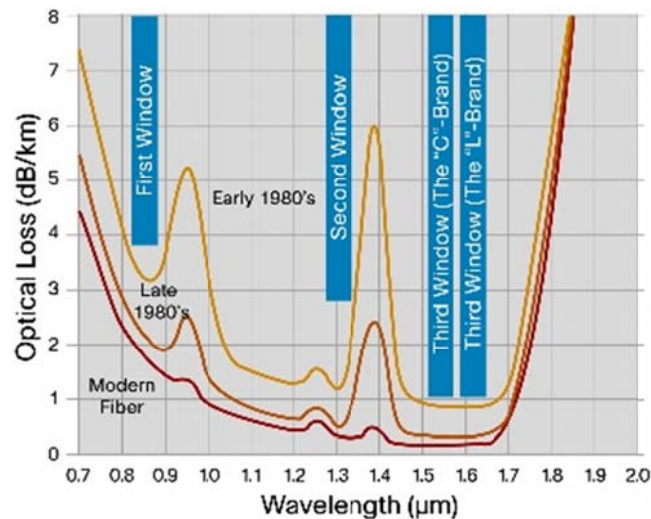


Figure 3.1 Attenuation versus wavelength and transmission windows [57]

Table 3.4 The effects of the input center wavelength on optical tweezer signal.

Input Center Wavelength(nm)	Depth of well (dB)	Width of well (nm)	FSR (nm)	Velocity($\mu\text{m/s}$)
750	2.96	0.3	2.7	8.23
850	2.88	0.3	3.5	8.975
900	2.89	0.5	3.9	8.829
1250	2.66	1	7	10.9

Table 3.4 (Cont.)

Input Center Wavelength(nm)	Depth of well (dB)	Width of well (nm)	FSR (nm)	Velocity($\mu\text{m/s}$)
1300	2.99	1	9	7.839
1450	2.75	1	10	10.24
1500	2.54	1	10	12.15
1550	2.88	2	12	8.794
1600	2.57	2	12	11.99
1700	2.95	1	14	8.087

The results in Table 3.4 and mathematical analysis from Equation (3.6) illustrate that width of well and FSR is directly proportional with the changing of center wavelength of the input signal. Moreover, the blue highlight in Tables 3.4 demonstrates the suitable parameter value for a 2 nm polystyrene particle which is trapped and manipulated with $\approx 8 \mu\text{m/s}$ of velocity.

3.4 Constrained Problem and the Design of Tweezer and Generators using Modified Circular Add-Drop Modulator

Normally, the design of tweezer and generators using MCADM is divided into 6 steps as follows:

- I. The definition of explicit constrained problems such as the size of particle, center wavelength of input signals and required velocity for particle trapping.
- II. The knowledge of the mathematical transfer function of the device is used to explain the characteristics or properties of tweezers signal.
- III. The analytical framework studies the mathematical transfer function with effect to the desire tweezers properties output, which is corresponding to the explicit domain of constrained problem.
- IV. All effected parameters from (III) for generating optical tweezers properties are tested and chosen the suitable parameter results for the corrected our desire output. The use of those suitable parameters is used for designing device MCADM.
- V. The designed MCADM is simulated or fabricated in order to confirm the optical tweezers properties.
- VI. The designed device in (V) is simulated to confirm the purpose of constrained problem or optical tweezer properties.

3.4.1 Defining Constraint of Problem

Our thesis focuses on the nanoparticle trapping and manipulation which the size of trapped particle is smaller than the wavelength of input signals and force is described and calculated by Rayleigh regime ($X \ll 1$) in section 2.1. This Rayleigh regime unit of force is in the range of piconewtons. The aim of this section will give some examples of constraint of problem definition for applying to the trapping tool application. There are many issues that must be realized for trapping tool application, the first conscious to increase the efficiency of optical tweezer for particle or molecular trapping is the obviously constrain of problem definition. The second is size of particles and center wavelength of input signals for particle trapping that relates to the calculated force regime. Third is the light property of a particle (refractive index) which must be suitable for trapping. The next issue is the required trapping velocity and the final issue is the suitable parameters of a trapping device which derives from analytical mathematical transfer function and its results in section 3.3. For the convenience, the popular neutral particle of polystyrene 2 nm is used for simulating our system with the trapping velocity $\approx 8 \mu\text{m/s}$ as constrained problem.

3.4.2 The Design of Tweezer and Generators using Modified Circular Add-Drop Modulator

- The suitable Parameters Specification

For constrained problem in section 3.4.2 in which the particle size is 2 nm and the require velocity is $\approx 8 \mu\text{m/s}$ and characteristic analysis results in section 3.3 that show the effected results of parameter change. All of table compares the variation of parameters with respect to depth of the well, width of well, FSR and velocity. In fact, the depth of well is related to the magnitude of gradient force while width of well shows the space for carrying the nanoparticle of polystyrene 2 nm size. FSR value is proportional to the carrying capacity of trapping tool and finally velocity must be realized for our need. In Tables 3.1 to 3.4 the blue highlighted rows are the suitable parameters for constrain of the problem. In conclusion of suitable parameters are summarized in Table 3.5.

Table 3.5 The suitable parameter specification for MCADM in order to generate optical tweezer signals for polystyrene 2 nm and velocity $\approx 8 \mu\text{m/s}$

Feature	Depth of well (dB)	Width of well (nm)	FSR (nm)	Velocity($\mu\text{m/s}$)
$\kappa_1 = 0.9$ $\kappa_3 = 0.1$ $\kappa_2 = \kappa_4 = 0.35$	2.88	2	12	8.794
$R_c \text{ or } R_d = 20 \mu\text{m}$ $R_R = R_L = 10 \mu\text{m}$	2.88	2	12	8.794
<i>InGaAsP</i>	2.88	2	12	8.794
$\lambda \text{ or } \lambda_0 = 1550 \text{nm}$	2.88	2	12	8.794

- The Design of Tweezer and Generators using Modified Circular Add-Drop Modulator

According to Table 3.5, the MCADM designed by the parameters are the intensity coupling coefficient (κ_1) between input and throughput ports is 0.9, the intensity coupling coefficients between center add-drop or center microring and left or right microring (κ_2, κ_4) are 0.35, the intensity coupling coefficient (κ_3) between add and drop ports is 0.1, the size of center ring radii ($R_c \text{ or } R_d$) is assigned by radii equals $20 \mu\text{m}$, the left and right ring radii ($R_R \text{ or } R_L$) are $10 \mu\text{m}$, the length of two straight bus waveguides that dovetailed center microring are $60 \mu\text{m}$, the material chosen for our requirement is InGaAsP and finally, the input center wavelength (λ_0) is 1550 nm. The physical geometry of MCADM is depicted in Figure 3.2 and the waveguide structure is shown in Figure 3.3.

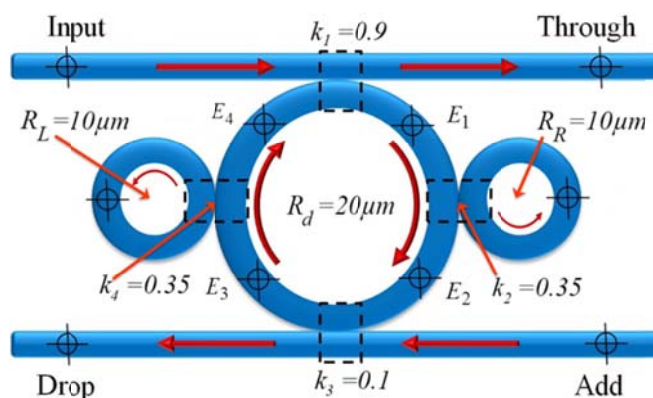


Figure 3.2 The physical geometry of MCADM

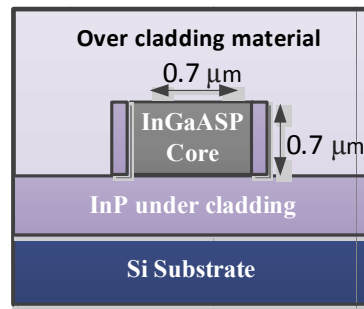


Figure 3.3 The waveguide structure

3.4.3 The Propose System

The overview of a system which is shown in Figure 3.4 consists of 4 parts: there are input, processing, output and molecular trapping applications. The input part is divided into 2 simulated tests; the first test is to input the Gaussian into processing part of the suitable parameter specification of RADM and CADM. The second test is the Gaussian and Dark Soliton inputs are fed to the processing to test and validate of our proposed suitable parameter values in Table 3.5. In the processing part, there are three modulator devices that are tested and compared the performance. The first modulator device is RADM which is the model following the literature review of Hong Cai and Andrew W. Poon. The second modulator is the model according to the literature of Dominik G. Rabus and finally, the proposed device is the model the same as the literature of Nattaporn Suwanpayak. The third part is output signal or optical potential or optical tweezer signal which evaluates the tweezer properties by the output waveform, depth of well, width of well, net force, capacity of trapping tool and velocity. In the final part is the molecular trapping application which beyond of our study.

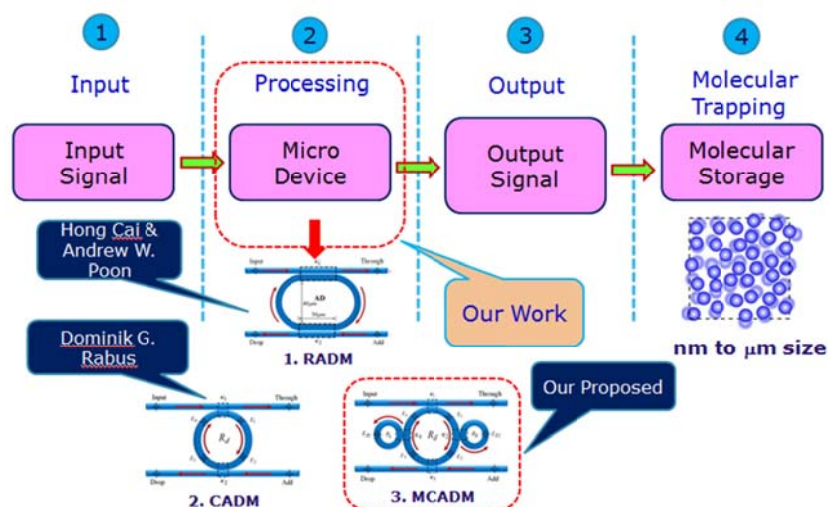


Figure 3.4 The overview of system

- **Primary Suitable Parameters Specification for RADM, CADM and MCADM**

The primary suitable parameter specification for RADM and CADM in Figure 3.5 is a process to find the most suitable parameters for testing and comparing the performance of two modulators with the proposed device. This system is divided into 3 parts there are input, processing and output as the same describing in Figure 3.4. To generate the Gaussian signal to the modulator, the input module consists of the classical tunable CW laser source, Erbium-Doped Fiber Amplifier (EDFA), Optical Collimator and temperature controller for controlling thermal effect of laser source and EDFA. Typically, the high-power laser radiation was provided by the Coherent Mira laser system in which an optical parametric oscillator (OPO) is responsible for converting the mode locked laser pulses coming out from a tunable Ti:sapphire laser from 800 nm to some wavelengths between 1,500 nm and 1,600 nm. Gaussian-like pulses having a FWHM of 2 ps can be found at the OPO output, with an average output power of 300 mW at a repetition rate of 35.6 MHz [56, 57]. In our case, the tunable laser source provides continuous Gaussian-like pulses having a FWHM of 35 fs whose power level ranges from 0 to 10 mW. If the duty cycle of pump laser was low, an EDFA is used to amplify the probe. Then the amplified CW was coupled from a single-mode fiber to free space through a collimator which a Gaussian signal can be generated and sampling into 20,000 samples before fed into the input port of MCADM. In processing part, four parameters are comprised of intensity coupling coefficient, ring radius size, material and input center wavelength are investigated. Finally, when the processing produces the output signal, then it is evaluated the tweezer properties by the output waveform, depth of well, width of well, net force, capacity of trapping tool and velocity.

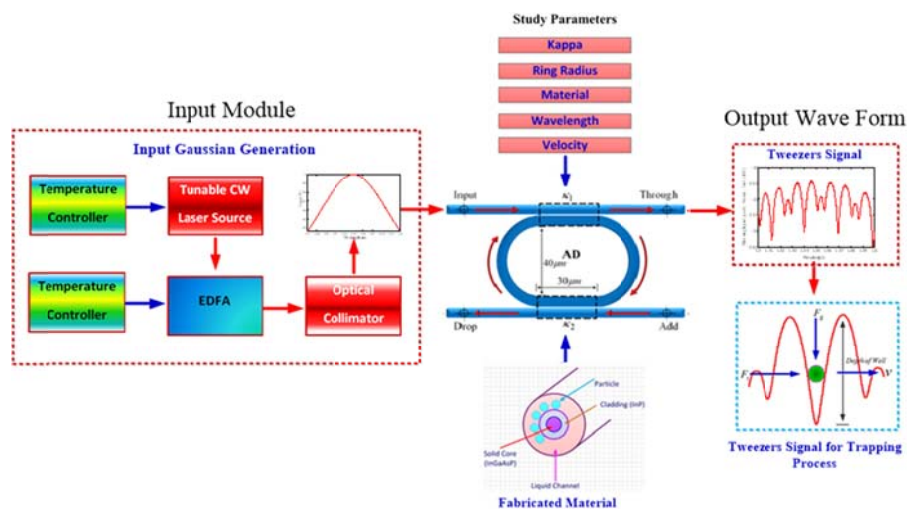


Figure 3.5 The primary parameters specification system of RADM

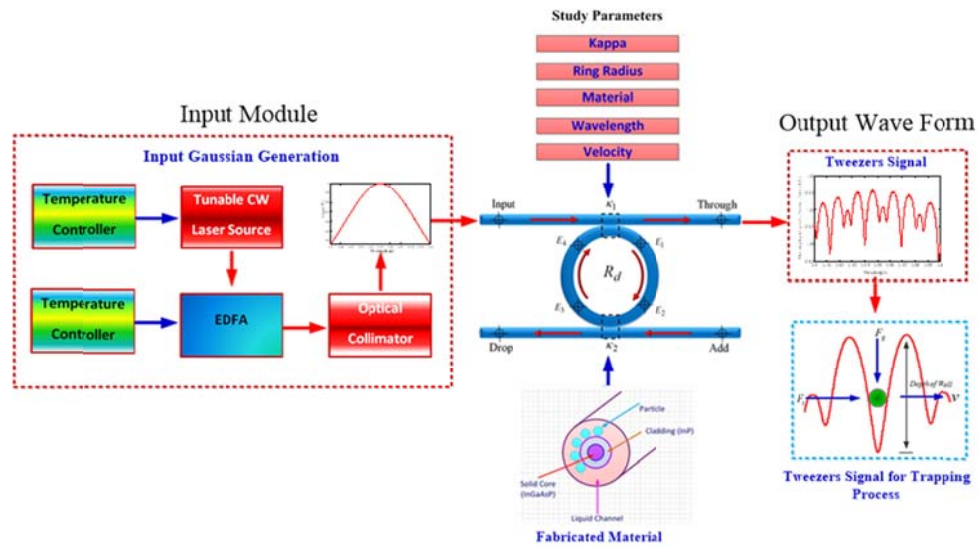


Figure 3.6 The primary parameters specification system of CADM

- **The Proposed System**

After finishing our design in section 3.4.2 and suitable parameter specification for RADM and CADM, the suitable parameter values of MCADM, RADM and CADM is simulated in the same environment in order to evaluate the performance of 3 modulators in the term of the output waveform, depth of well, width of well, net force, capacity of trapping tool and velocity. The proposed system in Figure 3.6 can be divided into 3 parts analogous to the primary parameter specification system. Recently, the new commercial instrument of the laser source is introduced in the name of “Fiber Laser”. In fact, the fiber laser is a laser in which the active gain medium is an optical fiber doped with rare-earth elements such as erbium, ytterbium, neodymium, dysprosium, praseodymium, and thulium. They are related to doped fiber amplifiers, which provide light amplification without lasing. Fiber nonlinearities, such as stimulated Raman scattering or four-wave mixing can also provide gain and thus serve as gain media for a fiber laser. Therefore, in case of two input system overview of tweezer generations as shown in Figure 3.6, this fiber laser is replaced the classical laser source that depicted as above system. Since the component inside fiber laser is comprised of EDFA, hence; the input module in the part of Gaussian signal generation does not need EDFA as above configuration. In the part of Dark Soliton generation, fiber laser source is used to originated and doped the Bright Soliton signal, then beam splitter is used to separate Bright and Dark Soliton which phase difference is $\frac{\pi}{2}$. Then, the detector is applied to determine the Bright Soliton, if one detector can detect Bright Soliton and at that time the other part of beam splitter is Dark Solution, which fed to collimator and generated Dark

Soliton Signal for fed to a MCADM in finally. The other parts of overview system are the same manners with the primary parameter specification system. The key idea of tweezer generation using Gaussian and Dark Soliton is compensated dispersion of output signal which occur from Gaussian dispersion by the merit of constant amplitude of Dark Soliton.

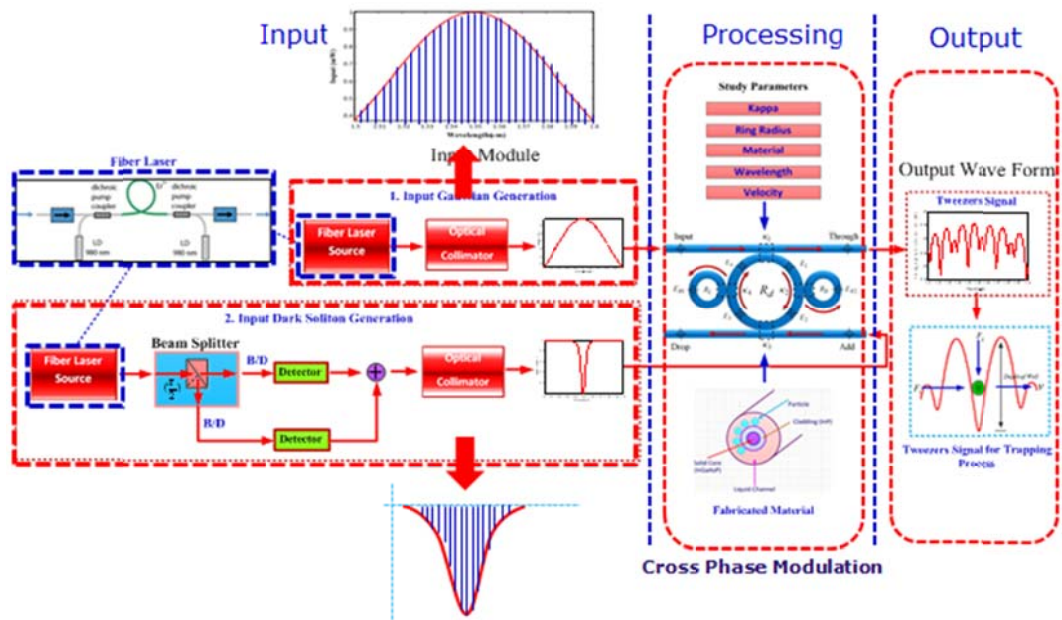


Figure 3.7 The proposed system

3.5 Summary

The responsible characteristic output results of three modulator devices are explained by mathematical transfer function of throughput and drop ports as demonstrated in section 2.6 and 3.2. The characteristic and result analysis of MCADM is demonstrated in section 3.3. The design of tweezers and generator using MCADM is presented in the last section. Moreover, the schematic of the primary parameter specification and proposed system which is shown in the last section is prepared the good understanding in experimental results and discussion in the next chapter.

Chapter 4

Experimental Results and Discussion

In this chapter, the simulation of primary suitable parameter specification for RADM, CADM and MCADM Results is proposed. The efficiency of devices is evaluated by output signal form, depth of well, width of well, FSR and velocity. Afterward, the experimental results of the proposed designed system tested by the suitable parameters of each modulator is reported. The investigated parameters are comprised of materials, intensity coupling coefficient, ring radius, center wavelength of the input signal. Then the velocity is examined to solve the constrained problems. The next section presents the performance comparisons among 3 modulators while the fourth presents the Opti-FDTD simulation results compared with the possibility of the proposed system using the other commercial program. The final section discusses the findings of the present research in relation with previous studied.

4.1 The Primary Suitable Parameter Specification for RADM, CADM and MCADM Results

Generally, the Gaussian pulse is used for simulation and experiment in most research. Therefore, the purpose of this experiment is to find the suitable parameters of RADM and CADM in order to use these parameters in simulation and comparison of the efficiency with the proposed system in the next section. Although the suitable parameters of MCADM are specified by mathematical transfer function in Chapter 3 (section 3.4 and 3.5), the experiment for validation suitable parameters for MCADM is essential. The primary suitable parameter specification experiment is divided into 3 subsections followed by modulator types. In each type, the suitable parameters are intensity coupling coefficient (κ), ring radius size (R_{ad}, R_R, R_L), material properties (n_0, n_2) and center wavelength (λ_0) of the input signals. The lower and upper bound values of each parameter are shown in Table 4.1.

Table 4.1 The parameters for primary suitable specification of 3 modulators simulation

Parameter	Symbol	RADM	CADM	MCADM
Gaussian pulse (a.u)	-	1	1	1
The effective core area of modulator (μm^2)	A_{eff}	0.49	0.49	0.49
Intensity attenuation loss (dB/mm)	α	5×10^{-5}	5×10^{-5}	5×10^{-5}
Intensity insertion loss	γ	0.01	0.01	0.01
Center ring radius (μm)	R_{ad}	2 - 20	2 - 20	2 - 20
Right ring radius (μm)	R_R	-	-	1 - 10
left ring radius (μm)	R_L	-	-	1 - 10
Intensity coupling coefficient of device	κ_1	0 - 1	0 - 1	0 - 1
	κ_2	-	-	0.35
	κ_3	0 - 1	0 - 1	0 - 1
	κ_4	-	-	0.35
Linear refractive index of materials	$n_0(\text{InGaAsP})$	3.34	3.34	3.34
	$n_0(\text{AlGaAs})$	3.28	3.28	3.28
	$n_0(\text{Ta}_2\text{O}_5)$	≈ 2.20	≈ 2.20	≈ 2.20
	$n_0(\text{SiN})$	2.20	2.20	2.20
	$n_0(\text{SiO}_2)$	1.53	1.53	1.53
Nonlinear refractive index of materials	$n_2(\text{InGaAsP})$	4.27×10^{-17}	4.27×10^{-17}	4.27×10^{-17}
	$n_2(\text{AlGaAs})$	1.50×10^{-17}	1.50×10^{-17}	1.50×10^{-17}
	$n_2(\text{Ta}_2\text{O}_5)$	7.23×10^{-19}	7.23×10^{-19}	7.23×10^{-19}
	$n_2(\text{SiN})$	2.40×10^{-15}	2.40×10^{-15}	2.40×10^{-15}
	$n_2(\text{SiO}_2)$	2.40×10^{-16}	2.40×10^{-16}	2.40×10^{-16}
Center wavelength of input signal (nm)	λ_0	700 - 1700	700 - 1700	700 - 1700

4.1.1 Racetrack Add-Drop Modulator (RADM)

Figure 4.1 shows the physical geometry of RADM comprised of two arcs with diameter of $40\ \mu\text{m}$ and coupling length of $30\ \mu\text{m}$ as mentioned in [15]. To study the responsible characteristic, the laser light is modelled in the form of Gaussian like pulse signal and then this signal is fed into the device at the input port to find the suitable parameters of RADM for molecular trapping and manipulation. The suitable parameters are evaluated based on the simulation results and output signal properties such as output waveform of signal, depth of well, width of well, FSR and velocity. The investigated parameters are comprised of the intensity coupling coefficient (κ), the ring radius size (R_{ad}), the material properties (n_0, n_2) and the center wavelength (λ_0) of the input signals. The lower and upper ranges of each parameter are shown in the 3rd column of Table 4.1.

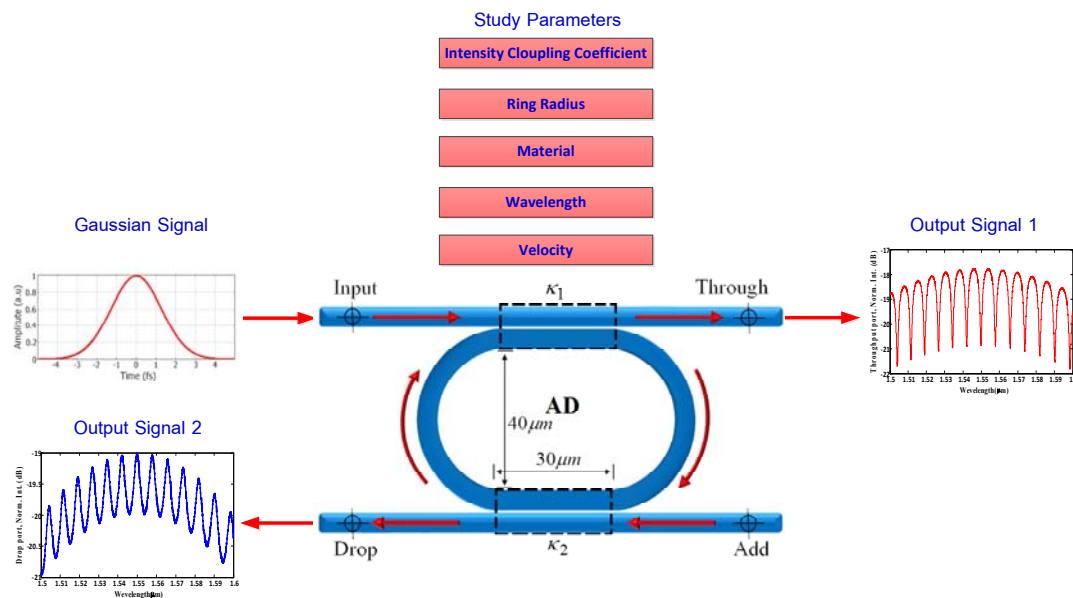


Figure 4.1 The physical geometry of RADM

● Intensity Coupling Coefficient

This section reports the results 2 tests. In the first test, κ_1 is equal to κ_2 and they vary proportionally. In the second test, κ_1 and κ_2 are different and they vary at the inversed proportion. The lower bound of κ is 0 and the upper bound is 1 and the variation interval of the intensity coupling coefficient is 0.05. The other parameters such as material ($n_0(\text{InGaAsP}), n_2(\text{InGaAsP})$), ring radius ($R_{ad} = 20\ \mu\text{m}$), and wavelength ($\lambda_0 = 1550\ \text{nm}$) are fixed, while the intensity coupling coefficient varies. Then, the variation effects of the intensity coupling coefficient (κ) on the output signal properties have been investigated.

Figure 4.2 shows the simulation results of the intensity coupling coefficient under the condition that κ_1 is equal to κ_2 ; meanwhile, Figure 4.3 shows the simulation results of the intensity coupling coefficient under the condition that κ_1 and κ_2 have different values. The red line represents the output signal at the throughput port and the blue line represents the output signal at the drop port. When comparing the results in Figure 4.2 and 4.3, it has been observed that the direct proportional increase of κ_1 and κ_2 is insignificant. Hence, Table 4.2 summarizes only the results when κ_1 and κ_2 are different.

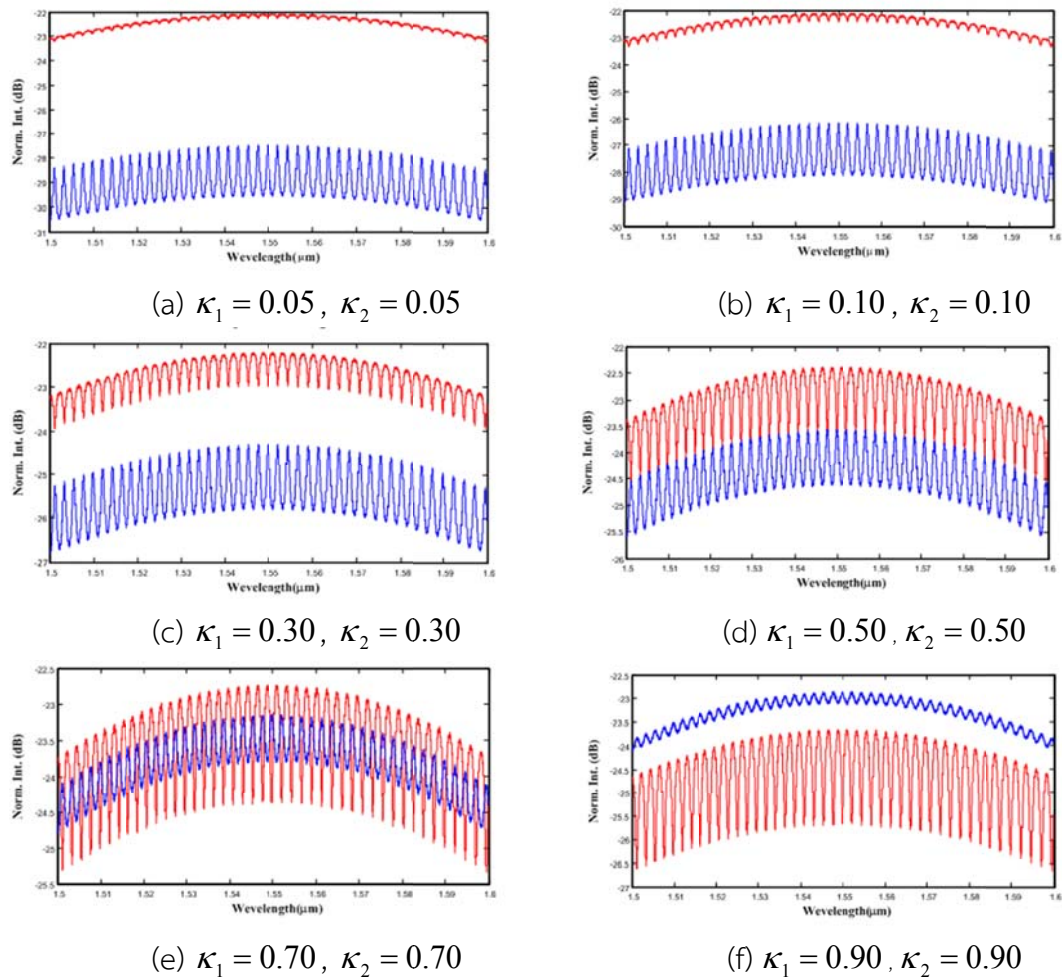


Figure 4.2 The comparison of the intensity coupling coefficient variations, when κ_1 equal to κ_2 of RADM

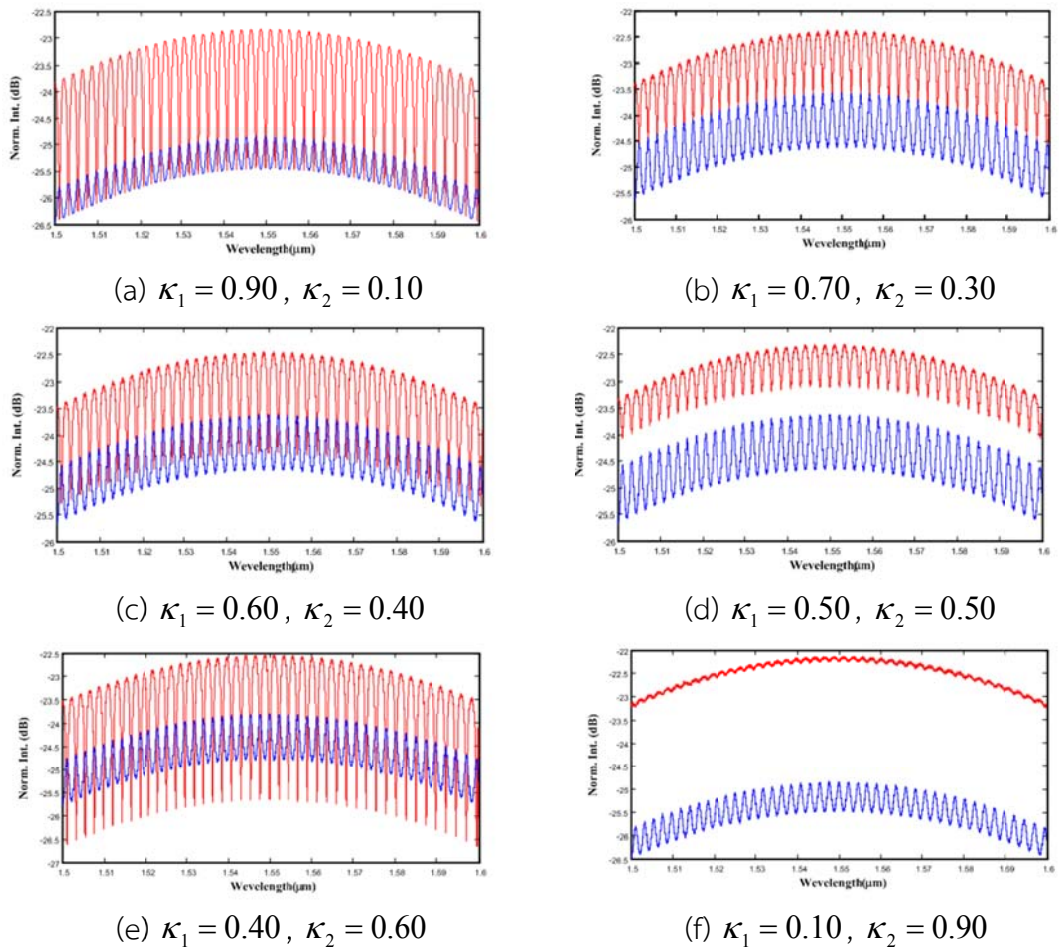


Figure 4.3 The comparison of the intensity coupling coefficient variations when κ_1 and κ_2 are different of RADM

Table 4.2 The effects of the intensity coupling coefficient on optical output signal

Intensity Coupling Coefficient		Depth of well (dB)	Width of well (nm)	FSR (nm)	Velocity($\mu\text{m}/\text{s}$)
κ_1	κ_3				
0.1	0.9	0.06	2.00	2	27.43
0.2	0.8	0.12	1.30	2	24.73
0.3	0.7	0.22	0.75	2	21.54
0.4	0.6	0.39	0.71	2	17.91
0.5	0.5	0.60	0.62	2	13.92
0.6	0.4	0.94	0.53	2	9.594
0.7	0.3	1.56	0.41	2	4.973
0.8	0.2	6.25	0.05	2	0.042
0.9	0.1	1.32	0.53	2	5.458

The increase of the intensity coupling coefficient is direct proportional to the increase of the depth of well or the magnitude of gradient force. RADM's width of well and velocity decrease, except when the intensity coefficient equals to 0.9.

● Materials

To study the effects of materials used to fabricated the waveguide, the parameters such as intensity coupling coefficients, ring radius, wavelength are fixed; on the other hand, the materials for fabricating microring resonator are varied. The fabricated material's properties are presented in Table 2.1 and summarized in Table 4.1. They are used for 3 modulators simulation. The intensity coupling coefficients are assigned as the followings: $\kappa_1 = 0.7$, $\kappa_2 = 0.3$, ring radius (R_{ad}) = $20 \mu m$, and the center wavelength of Gaussian input signal (λ_0) = $1550 nm$. Figure 4.4 shows the simulation results of different materials and the summary of material effects on the output properties is given in Table 4.3.

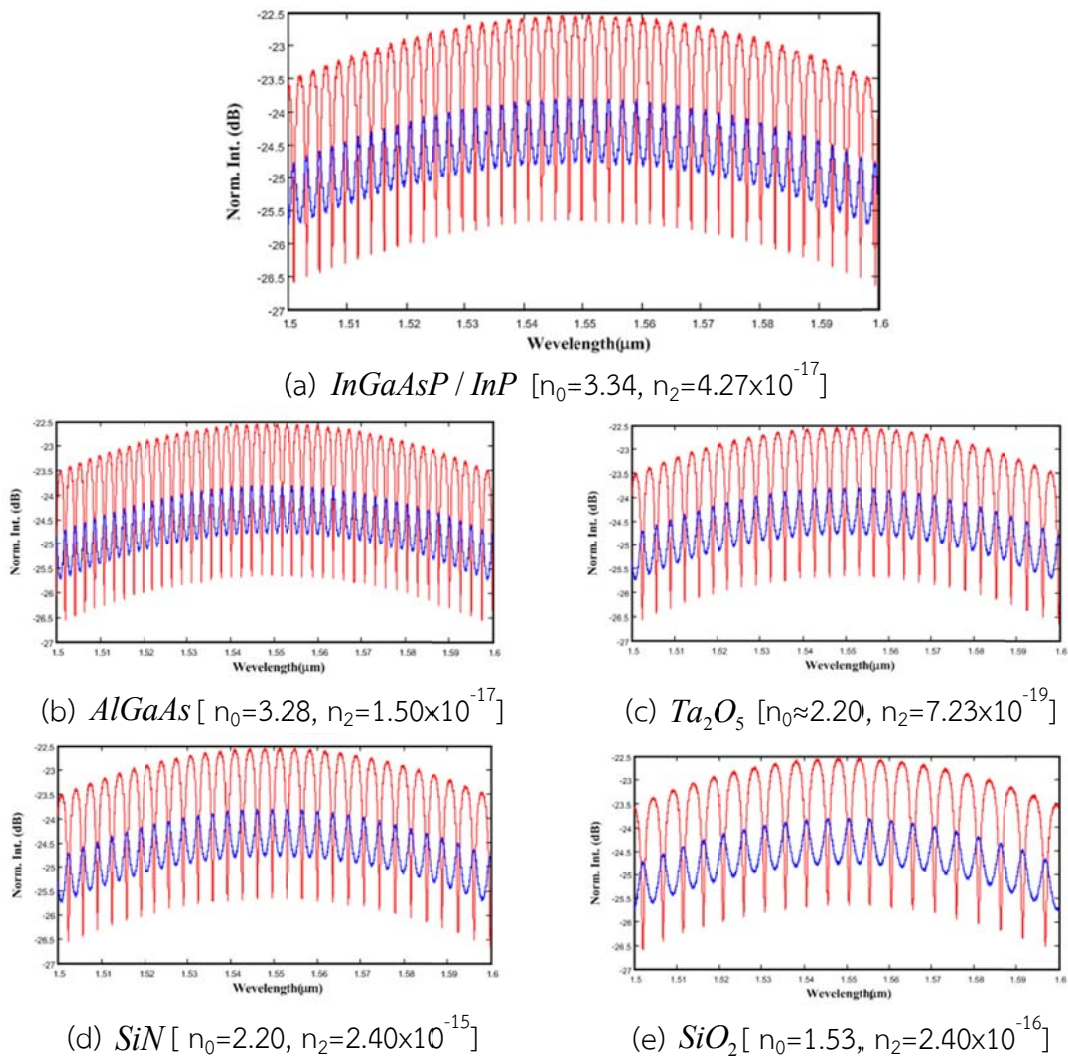


Figure 4.4 The comparison of fabricated materials effects of RADM

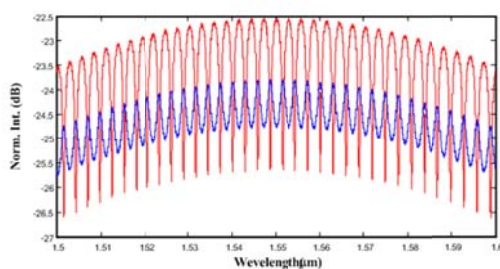
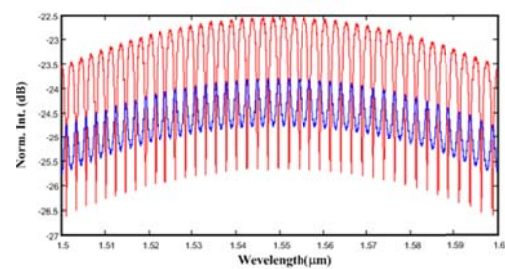
Table 4.3 The effects of fabricated materials on optical output signal

Fabricated Material	Depth of well (dB)	Width of well (nm)	FSR (nm)	Velocity ($\mu\text{m/s}$)
InGaAsP	1.55	0.4	2.3	4.973
AlGaAs	1.54	0.3	2.3	4.974
Ta2O5	1.55	0.6	3.6	4.973
SiN	1.56	0.7	3.5	4.973
SiO2	1.56	4.9	0.9	4.973

The increase of refractive index of materials is proportion to the decrease of FSR of devices. The width of well increases while the depth of the well and the velocity is insignificant.

● Ring Radius

The the study examines the effects of ring radius (R) variations on the output signal properties. The R_{ad} of RADM varies from 2 to 20 μm , and the other parameters such as the intensity coupling coefficients ($\kappa_1 = 0.7, \kappa_2 = 0.3$), materials ($n_0(\text{InGaAsP}), n_2(\text{InGaAsP})$), and wavelength ($\lambda_0 = 1550 \text{ nm}$) are fixed. The fabricated ring radius sizes range from 1.5 to 200 μm [45-60]. However, this research utilizes the largest upper bound of ring radius variation (20 μm) and the smallest lower bound (2 μm) to fabricate microring radius as suggested by [15]. Figure 4.5 shows the simulation results of the ring radius variations, while the effects of ring radius sizes can be summarized in Table 4.4.

(a) $R_{ad} = 10 \mu\text{m}$ (b) $R_{ad} = 12 \mu\text{m}$

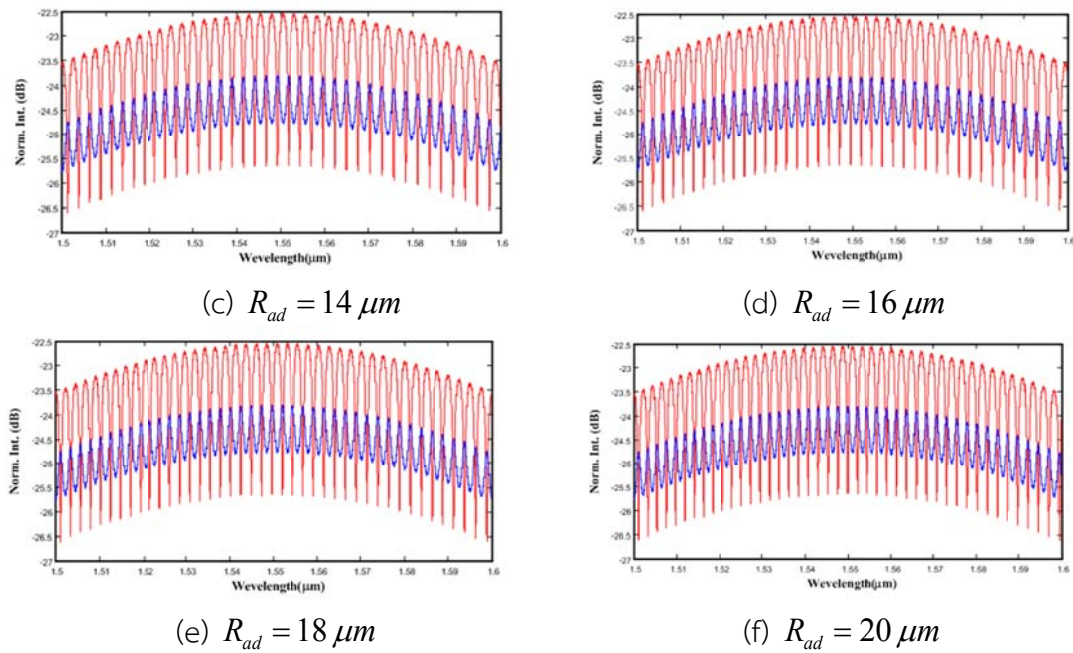


Figure 4.5 The comparison of add-drop ring radius effects of RADM

Table 4.4 The effects of ring radius size on optical output signal

Ring Radius Size (μm)		Depth of well (dB)	Width of well (nm)	FSR (nm)	Velocity ($\mu m/s$)
R_{ad}	$R_R = R_L$				
4	-	1.55	0.6	3.0	5.085
6	-	1.55	0.6	3.0	4.965
8	-	1.55	0.5	3.0	4.966
10	-	1.55	0.4	2.9	4.966
12	-	1.56	0.5	2.6	5.306
14	-	1.56	0.4	2.5	4.967
16	-	1.56	0.3	2.5	4.948
18	-	1.56	0.4	2.4	5.092
20	-	1.55	0.4	2.3	4.969

In this table, the increase of ring radius size affects to the decrease of FSR. The depth of well and velocity of RADM are insignificant while the width of well is ambiguous.

- Center Wavelength of Input Signal

The objective of the experiment is to study the effects of center wavelength variation on the output signal properties. Normally, the lasers deployed in optical communications typically operate at or around $0.850 \mu\text{m}$ in the first window, $1.310 \mu\text{m}$ in the second window, and $1.550 \mu\text{m}$ in the third window as shown in Figure 3.1. Therefore, the center wavelengths (λ_0) of the input signals are varied from 0.700 to $1.700 \mu\text{m}$. The coupled waveguides and the microring waveguide are made from InGaAsP/InP. The intensity coupling coefficients are assigned as the followings: $\kappa_1 = 0.7$, $\kappa_2 = 0.3$, and ring radius (R_{ad}) = $20 \mu\text{m}$. Figure 4.6 shows the results of the center wavelength input signal changes and the effects of input signal's center wavelength on the output properties are given in Table 4.5.

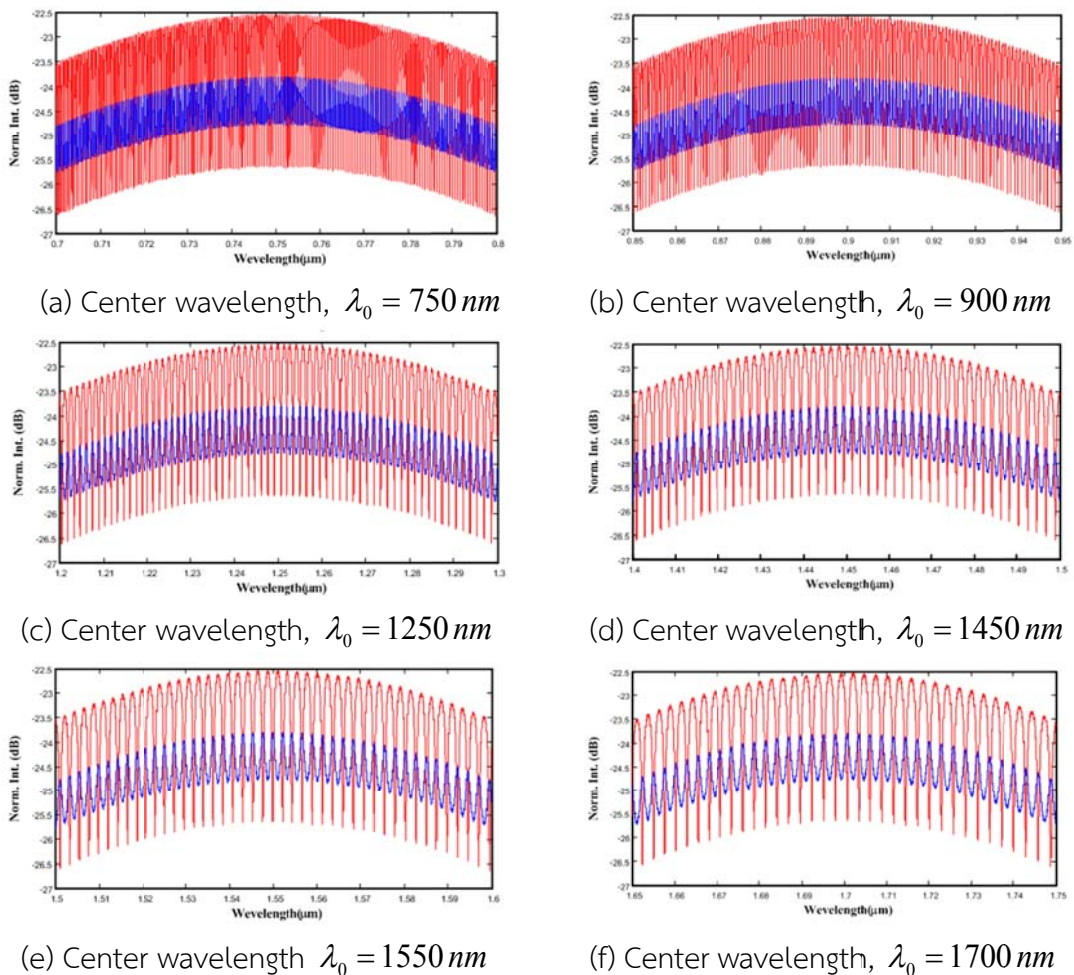


Figure 4.6 The comparison of wavelength effects of RADM

Table 4.5 The effects of input center wavelength variation on output signal

Input Center Wavelength(nm)	Depth of well (dB)	Width of well (nm)	FSR (nm)	Velocity($\mu\text{m/s}$)
750	1.55	0.1	0.6	4.973
850	1.54	0.1	0.7	4.988
900	1.55	0.2	0.8	4.984
1250	1.68	0.3	2.0	4.975
1450	1.66	0.4	2.0	4.973
1500	1.55	0.4	2.0	4.973
1550	1.56	0.4	2.0	4.973
1600	1.55	0.5	3.0	4.973
1700	1.47	1.0	3.0	4.972

The increase of input center wavelength of RADM is directly proportional to the width of well and FSR. The velocity is not quite different. The depth of well is ambiguous.

- **Velocity**

After the suitable parameter specifications of RADM are determined, the parameters (the intensity coupling coefficients, the ring radius size, the input center wavelength, the refractive index of material) are used for velocity approximation. The constrained parameters are the microring waveguide are made from InGaAsP/InP. The intensity coupling coefficient are assigned as the followings: $\kappa_1 = 0.7$, $\kappa_2 = 0.3$, ring radius (R_{ad}) = $20 \mu\text{m}$ and the input signal is Gaussian with center wavelength at $1.550 \mu\text{m}$. Considering the relation of intensity values and kinetic energy within the condition of no thermal effect and other losses, the velocity can be approximated as shown in Figure 4.7.

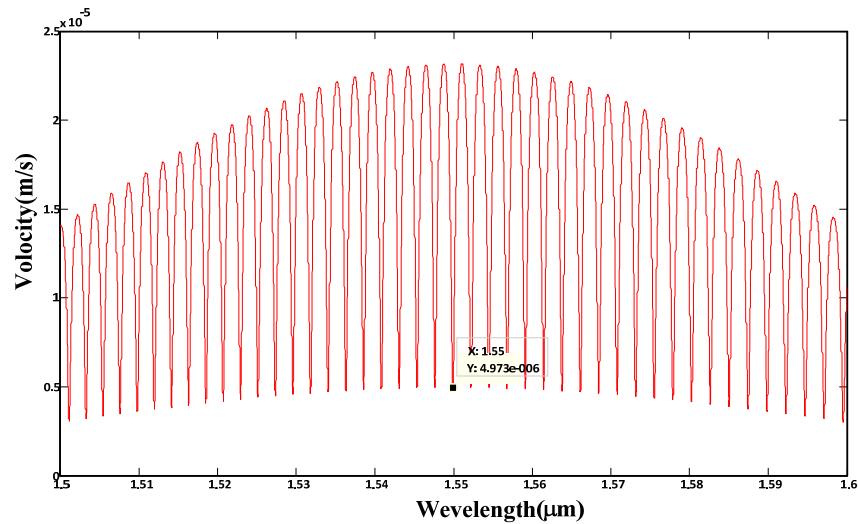


Figure 4.7 The comparison of velocity respect to the wavelength of RADM

4.1.2 Circular Add-Drop Modulator (CADM)

Figure 4.8 shows the physical geometry of CADM [14] with the ring radius of $20\ \mu\text{m}$. The laser light is modelled in the form of Gaussian and fed into the device at the input port to find suitable parameters of CADM for simulation and comparison with the proposed system. The objective of this experiment is find suitable parameters of CADM for particle trapping and manipulation. The investigated parameters are composed of the intensity coupling coefficient (κ), ring radius size (R_{ad}), the material properties (n_0, n_2) and the center wavelength (λ_0) of the input signal of which the lower and upper bounds of each parameter values are shown in the fourth column of Table 4.1.

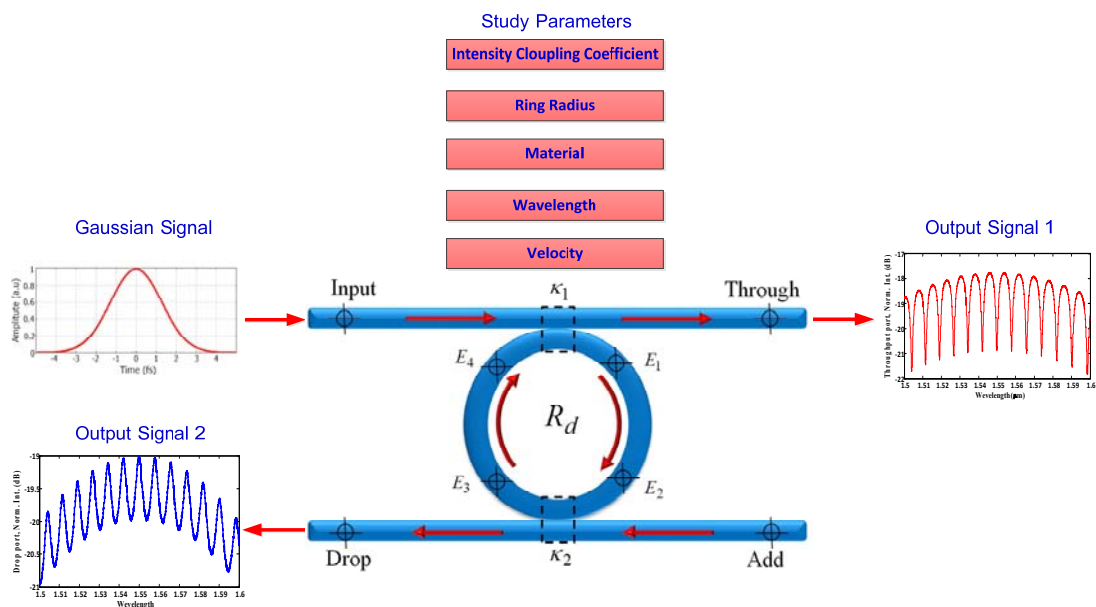
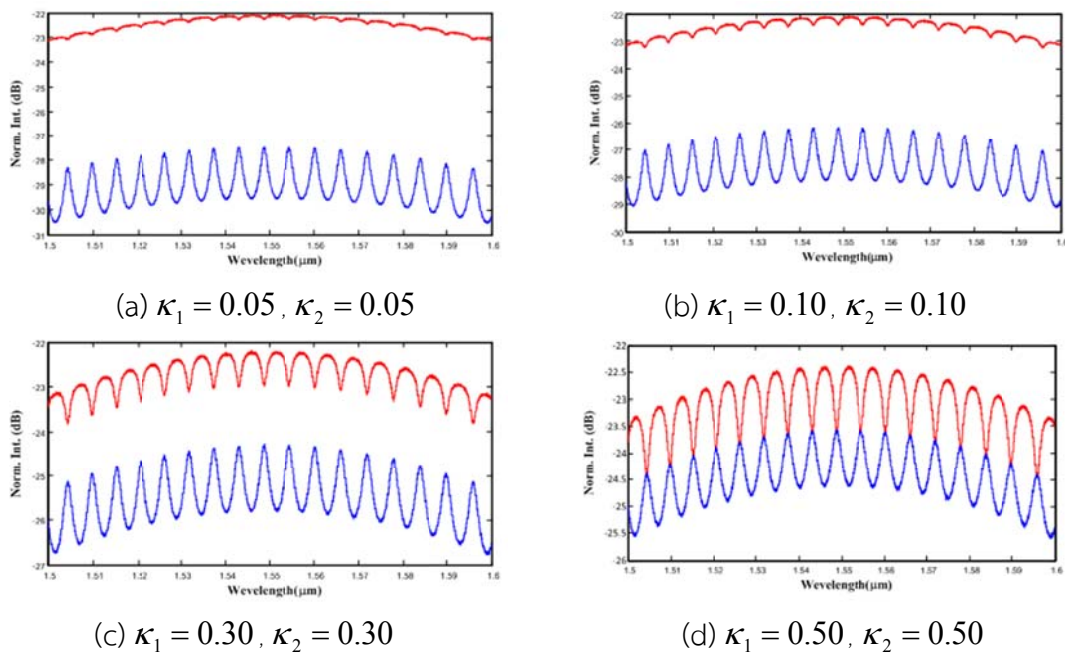


Figure 4.8 The physical geometry of CADM

- Intensity Coupling Coefficient

The purpose of the study is to explore the intensity coupling coefficient (κ) variation which affects output signal properties, so that the other parameters such as material ($n_0(\text{InGaAsP}), n_2(\text{InGaAsP})$), ring radius ($R_{ad}) = 20 \mu\text{m}$, and wavelength ($\lambda_0) = 1550 \text{nm}$ are fixed, while the intensity coupling coefficient is varied. The lower bound of κ is 0 and the upper bound is 1 and the varying interval of the intensity coupling coefficient is 0.05. This section reports the results 2 tests. In the first test, κ_1 is equal to κ_2 and they vary proportionally. In the second test, κ_1 and κ_2 are different and they vary at the inversed proportion. Figure 4.9 shows the simulation results of the intensity coupling coefficient effects under the condition when κ_1 equals to κ_2 , while figure 4.10 shows the simulation results of the intensity coupling coefficient effect under the condition when κ_1 and κ_2 have different values. In Figure 4.9-4.10, the red line represents the output signal at the throughput port and the blue line represents the output signal at the drop port. When comparing the results in Figure 4.9 and 4.10, it is observed that the equal increase of when κ_1 and κ_2 is insignificant; hence, the summary in Table 4.6 considers only the condition when κ values are different.



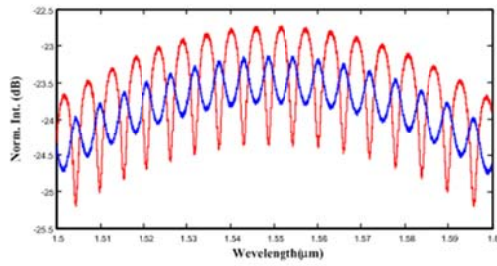
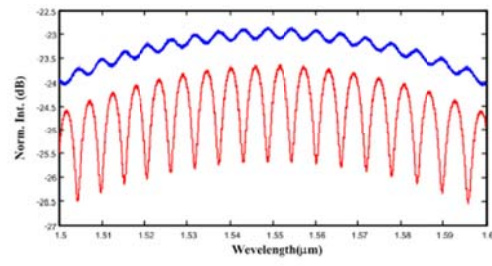
(e) $\kappa_1 = 0.70, \kappa_2 = 0.70$ (f) $\kappa_1 = 0.90, \kappa_2 = 0.90$

Figure 4.9 The comparison of the intensity coupling coefficient variations when κ_1 equal to κ_1 of CADM

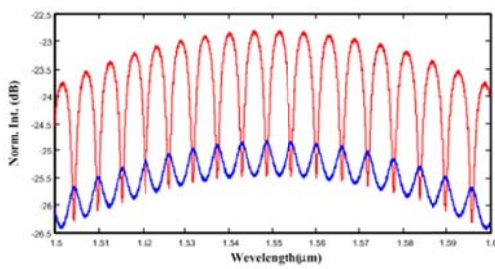
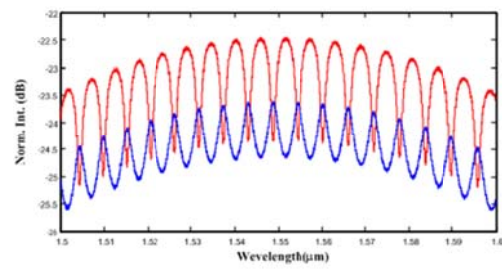
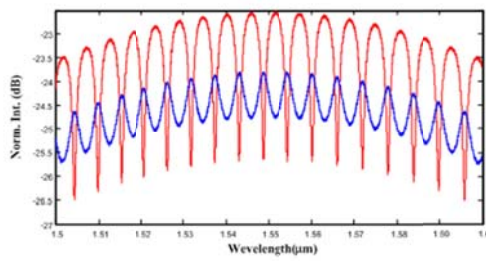
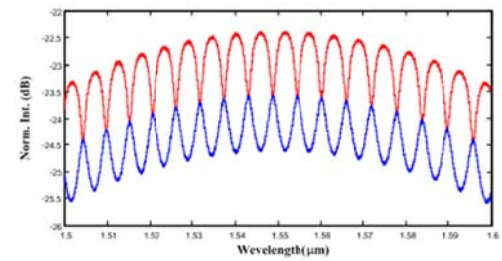
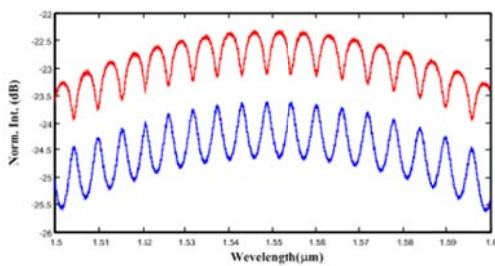
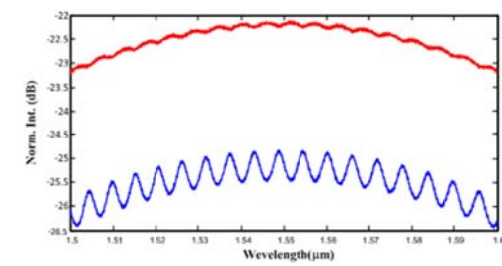
(a) $\kappa_1 = 0.90, \kappa_2 = 0.10$ (b) $\kappa_1 = 0.70, \kappa_2 = 0.30$ (c) $\kappa_1 = 0.60, \kappa_2 = 0.40$ (d) $\kappa_1 = 0.50, \kappa_2 = 0.50$ (e) $\kappa_1 = 0.40, \kappa_2 = 0.60$ (f) $\kappa_1 = 0.10, \kappa_2 = 0.90$

Figure 4.10 The comparison of the intensity coupling coefficient variations when κ_1 and κ_1 are different of CADM

Table 4.6 The effects of the intensity coupling coefficient on optical output signal

Intensity Coupling Coefficient		Depth of well (dB)	Width of well (nm)	FSR (nm)	Velocity ($\mu\text{m/s}$)
κ_1	κ_3				
0.1	0.9	0.06	3	6	27.42
0.2	0.8	0.13	2	6	24.72
0.3	0.7	0.23	2	5	21.53
0.4	0.6	0.39	2	6	17.9
0.5	0.5	0.60	2	5	13.9
0.6	0.4	0.94	1	6	9.58
0.7	0.3	1.56	1	6	4.958
0.8	0.2	7.74	0.1	6	0.012
0.9	0.1	1.32	1	5	5.473

The increase of the intensity coupling coefficient of RADM is directly proportional to the depth of well and the decrease of the width of well and the velocity value. However, for FSR, this increasing is insignificant.

- **Materials**

This study examines the waveguide material effects on the output signal properties; thus, the other parameters such as intensity coupling coefficients, ring radius, wavelength are fixed, while the material for fabricating microring resonator is varied. The fabricated materials properties are given in Table 2.1 and the summarized values in table 4.1 are often used for CADM simulation. The intensity coupling coefficients are assigned as the followings: $\kappa_1 = 0.7$, $\kappa_2 = 0.3$, ring radius (R_{ad}) = $20 \mu\text{m}$, and the center wavelength of Gaussian input signal (λ_0) = 1550 nm . Figure 4.12 shows the simulation results of different materials, and the summary of materials effects on the output properties is shown in Table 4.7.

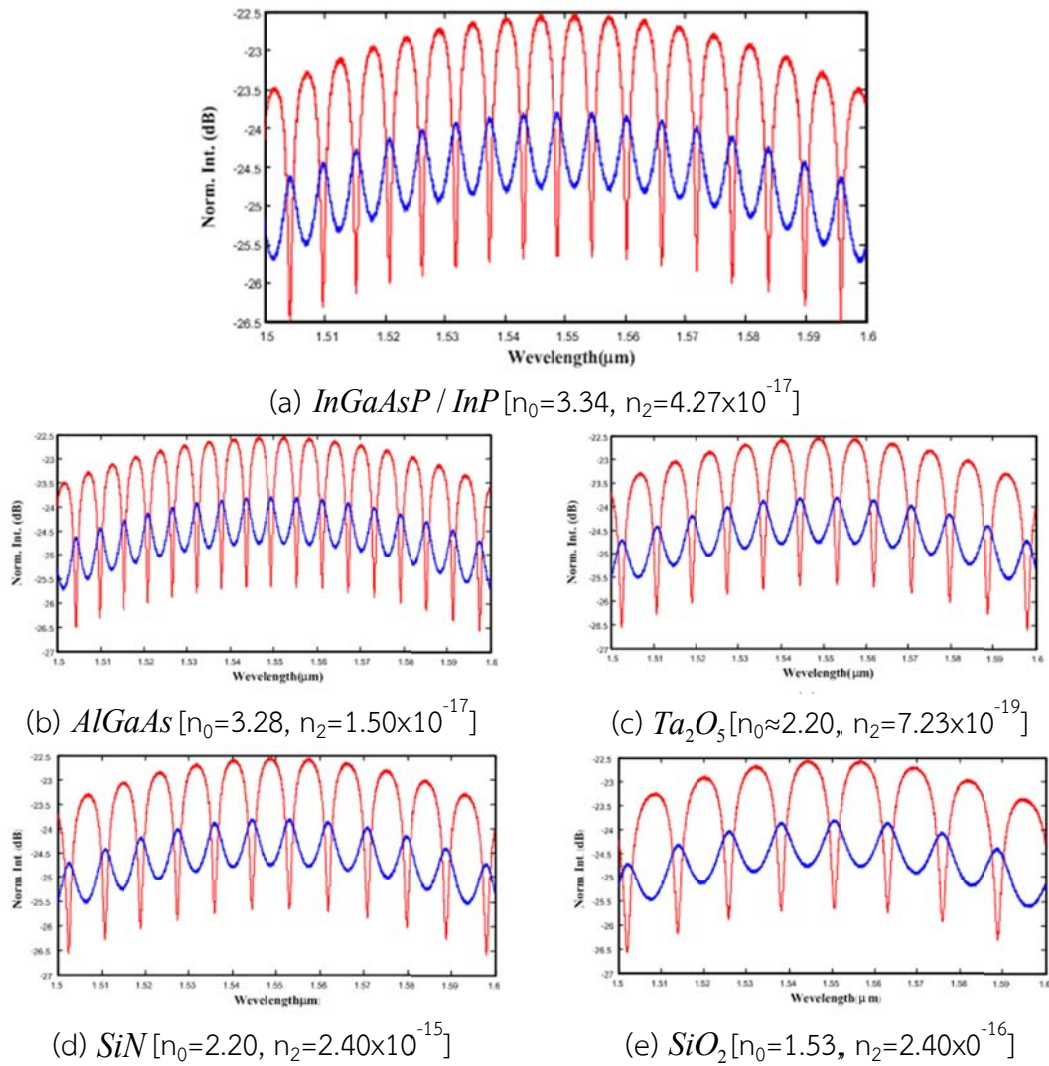


Figure 4.11 The comparison of fabricated material effects of CADM

Table 4.7 The effects of fabricated materials on optical output signal

Fabricated Material	Depth of well (dB)	Width of well (nm)	FSR (nm)	Velocity ($\mu\text{m/s}$)
InGaAsP	1.56	1	6	4.958
AlGaAs	1.55	1	5	4.959
Ta2O5	1.55	2	9	4.929
SiN	1.56	2	9	4.929
SiO2	1.55	3	13	4.929

The increase of refractive index of the materials is proportional to the width of well and FSR. However, the depth of well and velocity are insignificant.

- Ring Radius

The ring radius (R) variation effects on the output signal properties are investigated. The R_{ad} of CADM is varied from 2 to 20 μm while the other parameters such as intensity coupling coefficient are assigned as the followings: $\kappa_1 = 0.7$, $\kappa_2 = 0.3$, material properties $n_0(\text{InGaAsP})$, $n_2(\text{InGaAsP})$, and wavelength (λ_0) = 1550 nm. The fabricated ring radii used in this research are in the range of 1.5 to 200 μm [25-31]. Figure 4.12 shows the simulation results of the ring radius variation and the effects of ring radius size variation can be summarized in Table 4.8.

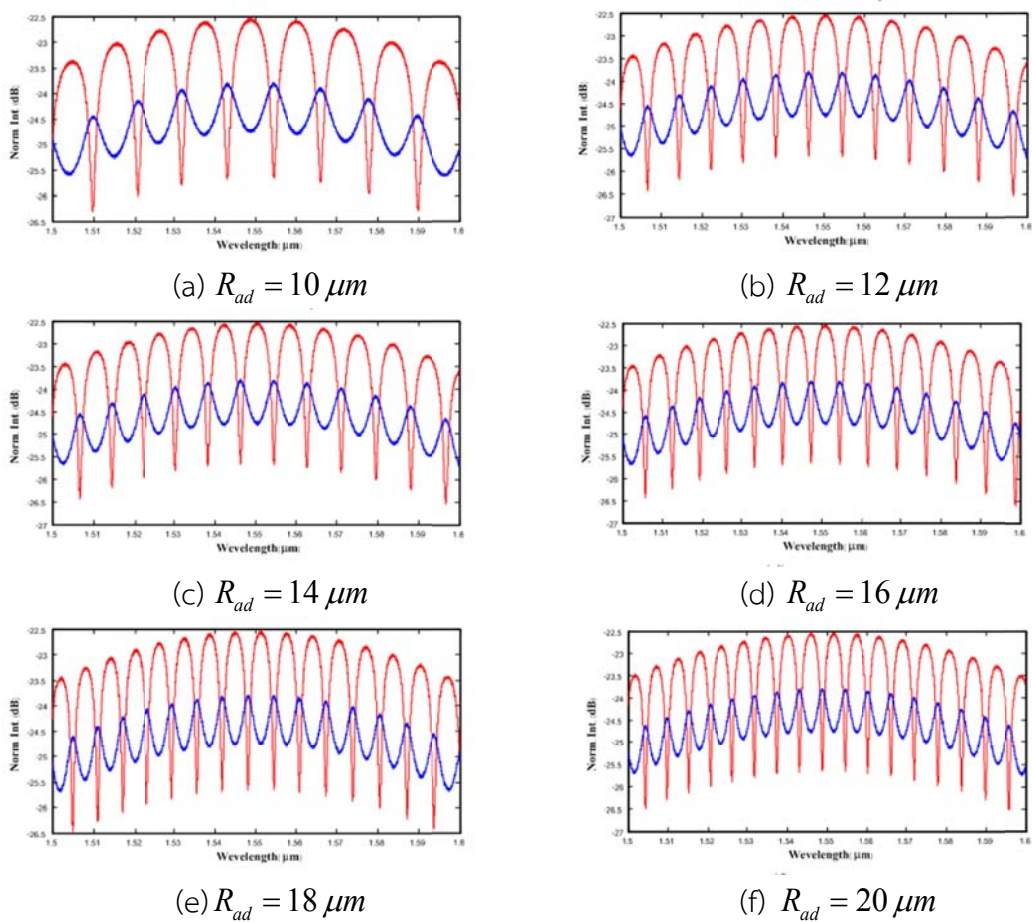


Figure 4.12 The comparison of different add-drop ring radii of CADM

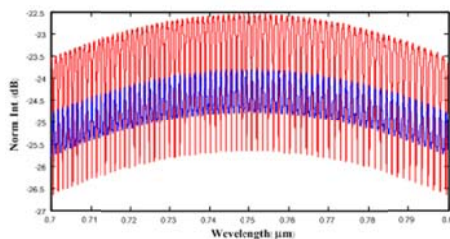
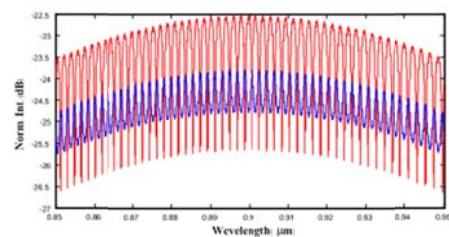
Table 4.8 The effects of ring radius sizes on optical output signal

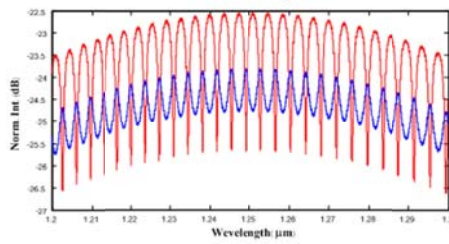
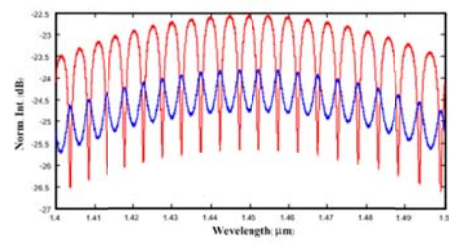
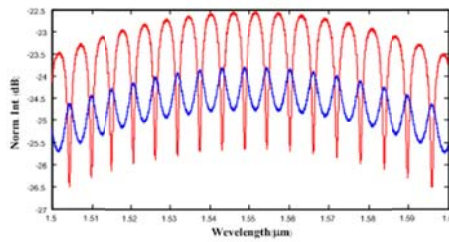
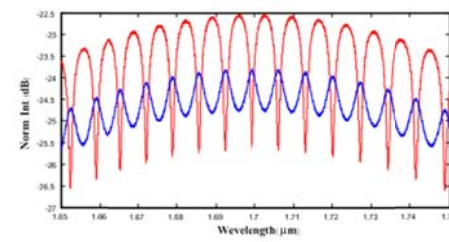
Ring Radius Size (μm)		Depth of well (dB)	Width of well (nm)	FSR (nm)	Velocity ($\mu\text{m/s}$)
R_{ad}	$R_R = R_L$				
4	-	1.66	6	29	4.933
6	-	1.61	3	18	4.933
8	-	1.58	3	15	4.934
10	-	1.57	3	12	4.935
12	-	1.56	1	10	4.935
14	-	1.56	1	9	4.943
16	-	1.56	1	7	4.95
18	-	1.56	1	7	4.955
20	-	1.56	1	6	4.958

The increase of ring radius size is inversely proportional to depth of well, the width of well and FSR. However, the velocity is directly proportional.

● Center Wavelength of Input Signal

The effects of center wavelength variations on the output signal properties are examined. This center wavelengths of input signals are varied from 0.700 to 1.700 μm . The upper (1.700 μm) and lower bound (0.700 μm) of frequency study is mentioned in section 4.1.1. The other parameters are coupled waveguides and the microring waveguide are made from InGaAsP/InP, and the intensity coupling coefficient is assigned as the followings: $\kappa_1 = 0.7$, $\kappa_2 = 0.3$ and ring radius (R_{ad}) = 20 μm . Figure 4.13 shows the results of the center wavelength input signal changes while the summary of the center wavelength of input signal effects on the output properties are shown in Table 4.9.

(a) Center wavelength, $\lambda_0 = 750 \text{ nm}$ (b) Center wavelength, $\lambda_0 = 900 \text{ nm}$

(c) Center wavelength, $\lambda_0 = 1250 \text{ nm}$ (d) Center wavelength, $\lambda_0 = 1450 \text{ nm}$ (e) Center wavelength, $\lambda_0 = 1550 \text{ nm}$ (f) Center wavelength, $\lambda_0 = 1700 \text{ nm}$ **Figure 4.13** The comparison of t wavelength effects of CADM**Table 4.9** The effects of input center wavelength variation on optical output signal

Input Center Wavelength(nm)	Depth of well (dB)	Width of well (nm)	FSR (nm)	Velocity($\mu\text{m}/\text{s}$)
750	1.55	0.2	1.3	4.959
850	1.56	0.3	1.8	4.960
900	1.55	0.4	1.9	4.959
1250	1.56	0.7	4.0	4.959
1450	1.57	1.0	5.0	4.954
1500	1.56	2.0	5.0	4.958
1550	1.56	2.0	6.0	4.958
1600	1.56	1.0	6.0	4.955
1700	1.56	1.0	7.0	4.959

The increase of the input center wavelength affects the width of well and FSR. However, the depth of well and velocity are insignificant.

- **Velocity**

After the suitable parameter specifications of CADM are determined, the parameters (the intensity coupling coefficients, the ring radius size, the input center wavelength, the refractive index of material) are used for velocity

approximation. The constrained parameters are the microring waveguide are made from InGaAsP/InP, intensity coupling coefficients are assigned as the followings: $\kappa_1 = 0.7$, $\kappa_2 = 0.3$, ring radius (R_{ad}) = $20 \mu m$. The input signal is Gaussian with the center wavelength of $1.550 \mu m$. Considering of intensity values and kinetic energy relation within the condition of no thermal effect and other losses, the velocity can be approximated and shown in Figure 4.14.

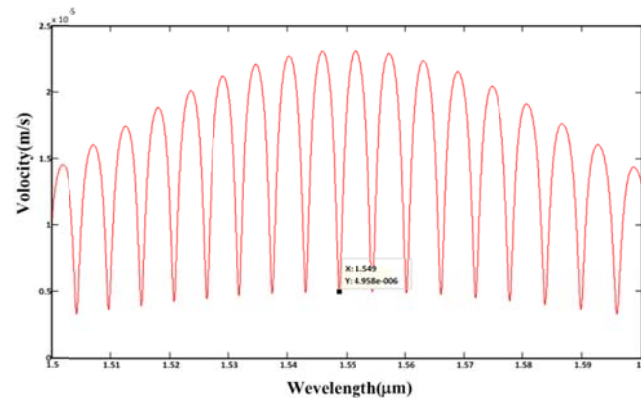


Figure 4.14 The comparison of velocity with respect to the wavelength of CADM

4.1.3 Modified Circular Add-Drop Modulator (MCADM)

Figure 4.15 shows the physical geometry of MCADM [16] that is comprised of three microrings which are the center microring, and the left and right microrings. Although the suitable parameters of MCADM are specified by mathematical transfer function in Chapter 3 (section 3.4 and 3.5), the experiment for validating suitable parameters for MCADM is a necessity. To study the responsible characteristics, the laser light is modelled in the form of Gaussian and fed into the device at the input port to confirm the suitable parameters of MCADM for particle trapping and manipulation as mentioned in section 3.4.3 (Figure 3.5). The investigated parameters are comprised of the intensity coupling coefficient (κ), ring radius sizes (R_{ad}, R_R, R_L), material properties (n_0, n_2) and center wavelength (λ_0) of the input signal of which the lower and upper bound of each parameter values are shown in the fifth column of Table 4.1.

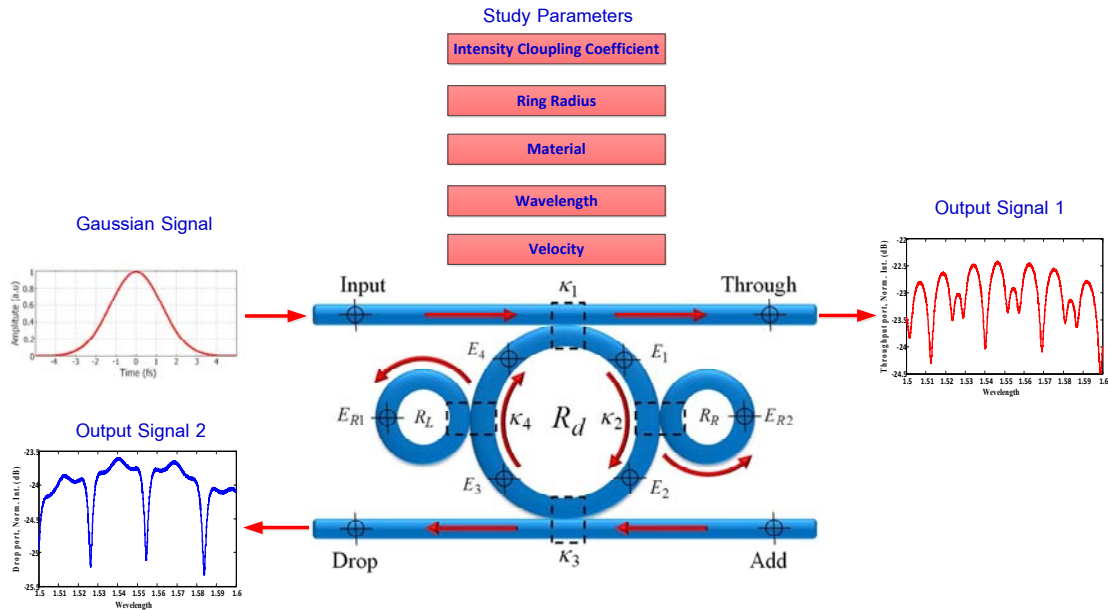


Figure 4.15 The physical geometry of MCADM

● Intensity Coupling Coefficient

In this section, the research studies the effects of the intensity coupling coefficients (κ) variations on output signal properties, and the other parameters such as material properties ($n_0(\text{InGaAsP})$, $n_2(\text{InGaAsP})$), ring radius ($R_{ad} = 20 \mu\text{m}$, $R_R = R_L = 10 \mu\text{m}$) and center wavelength of input signal ($\lambda_0 = 1550 \text{nm}$) are fixed, while the intensity coupling coefficient is varied. To achieve a systematic balance, κ_2 and κ_4 are assigned as 0.35. The lower bound of κ_1, κ_3 is 0 and the upper bound is 1 and the varying interval of the intensity coupling coefficient is 0.05. This section reports the results of 2 tests. In the first test, κ_1 is equal to κ_3 and they vary proportionally. In the second test, κ_1 and κ_3 are different and they vary at the inverted proportion. Figure 4.16 shows the simulation results of the intensity coupling coefficient effects under the condition that κ_1 equals to κ_3 , meanwhile Figure 4.18 shows the simulation results of the intensity coupling coefficient effect under the condition that κ_1, κ_3 have different values. The red line represents the output signal at the throughput port and the blue line represents the output signal at the drop port. When comparing the results in Figures 4.16 and 4.17, it is observed that the equal increase of κ_1, κ_3 is insignificant; hence, the summary in Table 4.10 considers only the condition when the κ values are different.

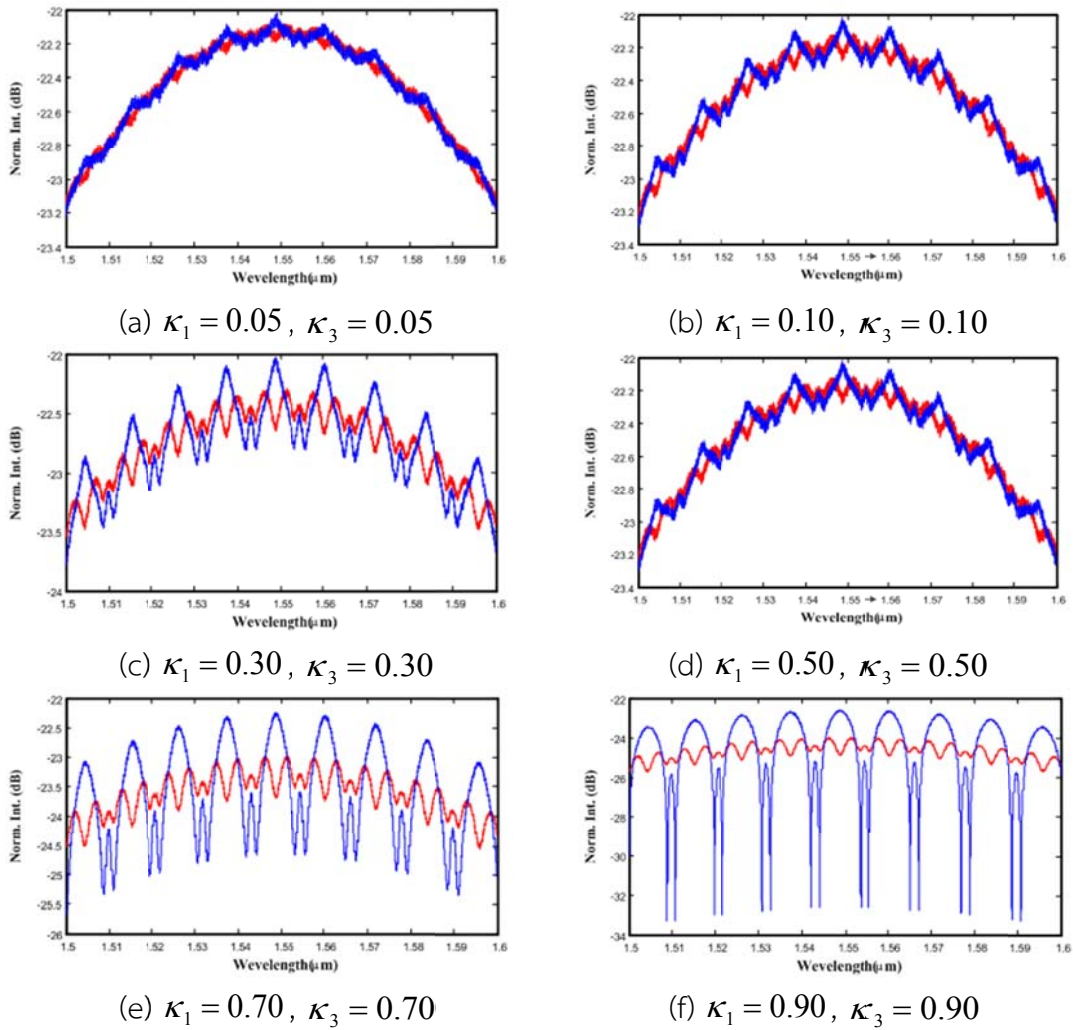
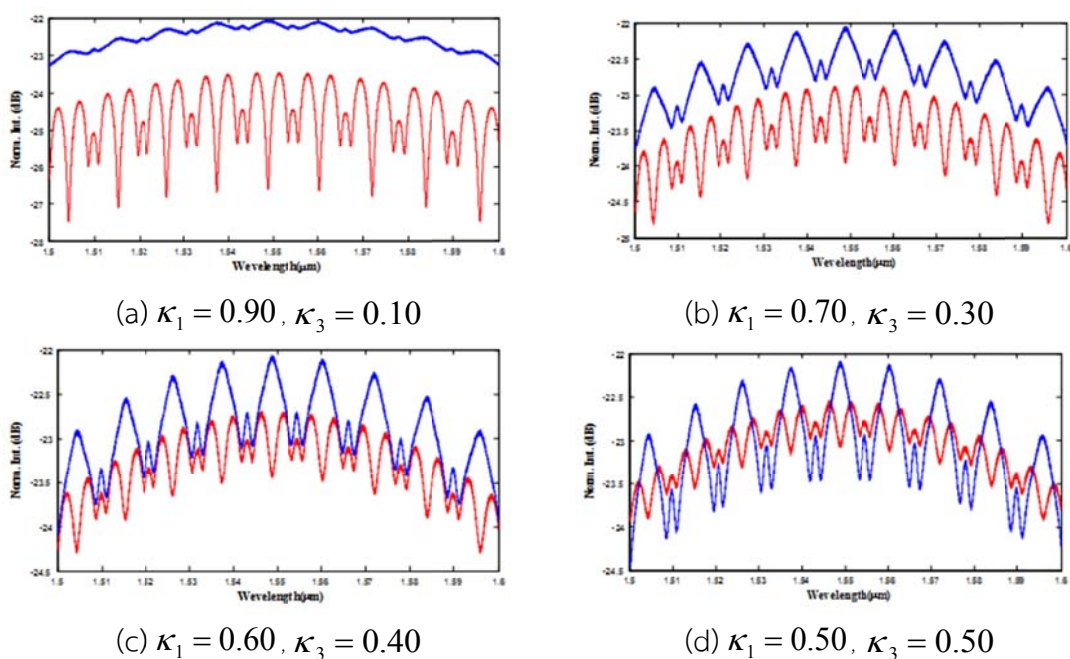


Figure 4.16 The comparison of the intensity coupling coefficient variations when κ_1 equals to κ_3 of MCADM



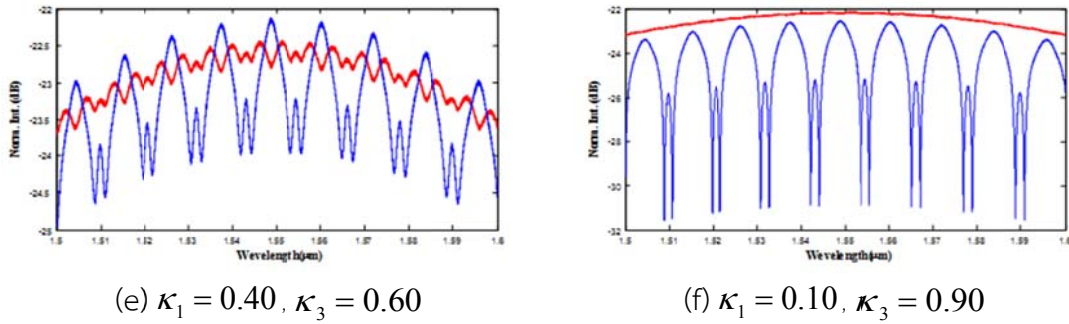


Figure 4.17 The comparison of the intensity coupling coefficient variations when κ_1 and κ_3 are different of MCADM

Table 4.10 The effects of the intensity coupling coefficient on the optical output signal

Intensity Coupling Coefficient		Depth of well (dB)	Width of well (nm)	FSR (nm)	Velocity ($\mu\text{m/s}$)
κ_1	κ_3				
0.1	0.9	0.04	2	12	27.74
0.2	0.8	0.08	2	12	25.69
0.3	0.7	0.11	2	12	23.41
0.4	0.6	0.17	2	11	20.88
0.5	0.5	0.25	2	11	18.11
0.6	0.4	0.38	2	11	15.06
0.7	0.3	0.54	2	11	11.66
0.8	0.2	1.02	2	11	7.79
0.9	0.1	1.58	2	11	3.04

The increase of the intensity coupling coefficient of MCADM results in the increase of the depth of well but the decrease of FSR and velocity. Nevertheless, the width of well is insignificant.

- **Materials**

This research also studies the effects of waveguide materials on the output signal properties; thus, the other parameters such as the intensity coupling coefficients, the ring radius, the wavelength are fixed, while the materials for fabricating microring resonator are varied. The fabricated materials properties in Table 2.1 and 4.1 are used for the simulation. The intensity coupling coefficients

are assigned as the followings: $\kappa_1 = 0.9$, $\kappa_2 = \kappa_4 = 0.35$, $\kappa_3 = 0.1$, ring radii $(R_{ad}) = 20 \mu m$, $(R_R = R_L) = 10 \mu m$ and the input signal is Gaussian with the center wavelength of $\lambda_0 = 1550 nm$. Figure 4.18 shows the simulation results of different materials and the summary of materials effects on the output properties is shown in Table 4.11.

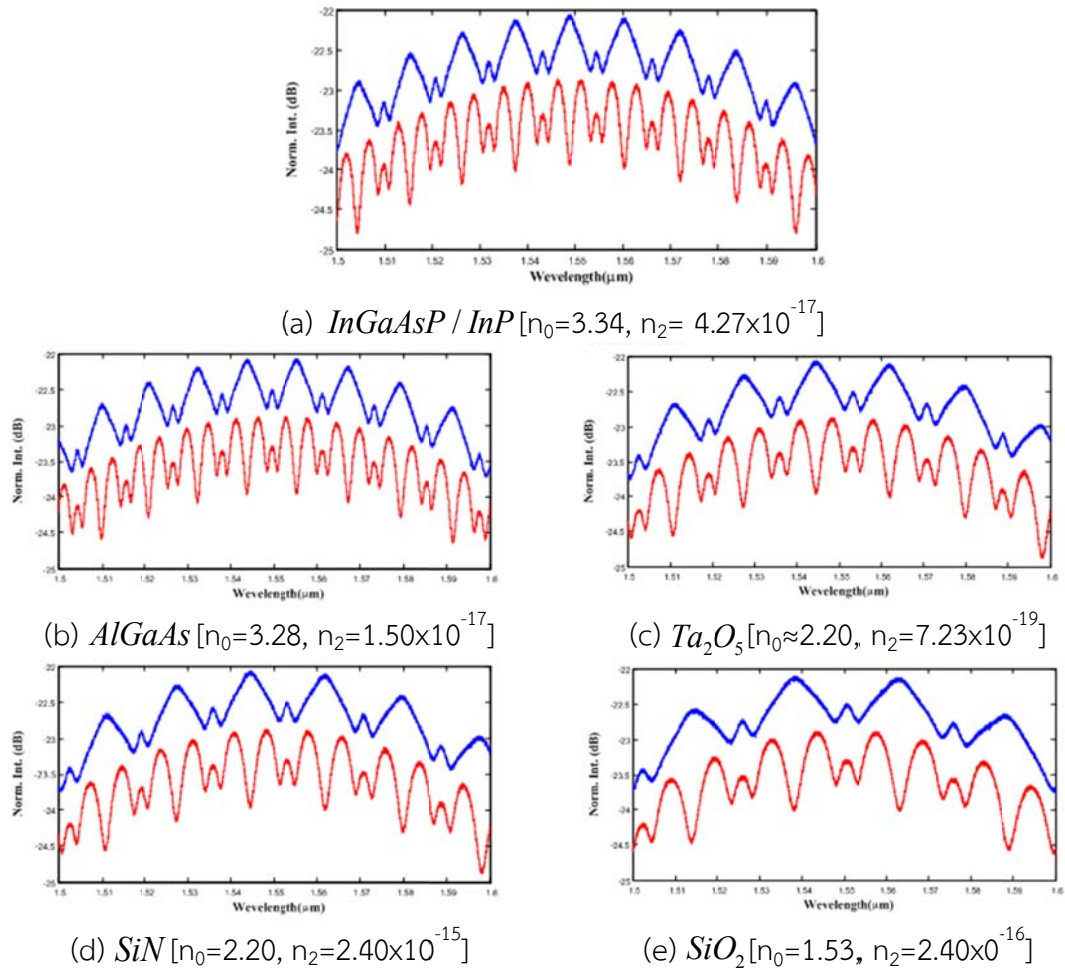


Figure 4.18 The comparison of fabricated material effects of MCADM

Table 4.11 The effects of fabricated materials on optical output signal

Fabricated Material	Depth of well (dB)	Width of well (nm)	FSR (nm)	Velocity($\mu m/s$)
InGaAsP	1.58	2	11	3.043
AlGaAs	1.58	1	11	3.021
Ta ₂ O ₅	1.58	1	18	3.026
SiN	1.58	1	18	3.026
SiO ₂	1.60	2	25	2.960

The increase of refractive index of materials is proportional with FSR and velocity. Nonetheless, the depth of well and the width of well are insignificant.

- Ring Radius

The ring radius (R_{ad}, R_R, R_L) variation effects on the output signal properties are examined. Usually, the fabricated ring radius sizes are in the range of 1.5 to 200 μm . Therefore, this research chooses the central ring radius varying from 2 to 20 μm . The left and right (R_L, R_R) microring are varied from 1 to 10 μm , and the other parameters such as intensity coupling coefficient are assigned as the followings: $\kappa_1 = 0.9$, $\kappa_2 = \kappa_4 = 0.35$, $\kappa_3 = 0.1$, the material properties ($n_0(\text{InGaAsP})$, $n_2(\text{InGaAsP})$), the wavelength (λ_0) = 1550 nm. Figure 4.19 shows the simulation results of the ring radius variation while the effects of ring radius size variation can be summarized in Table 4.12.

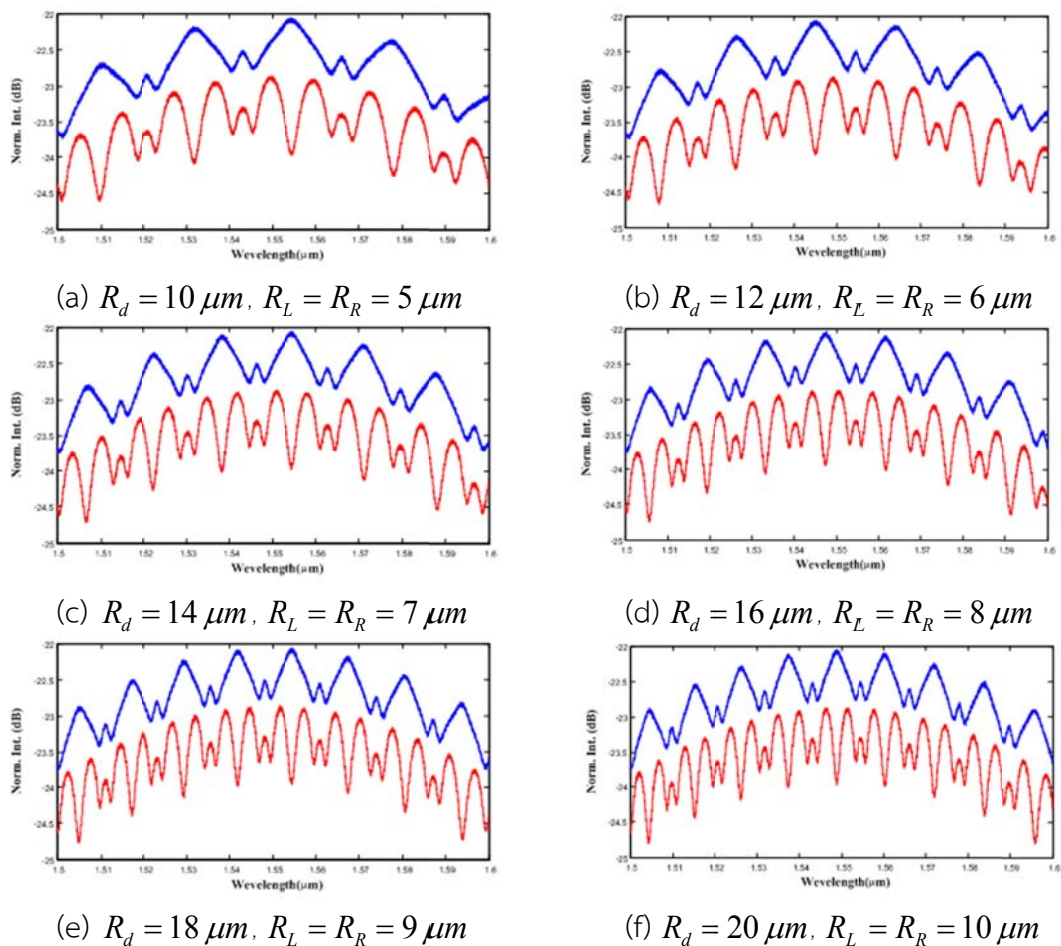


Figure 4.19 The comparison of different micro ring radii of MCADM

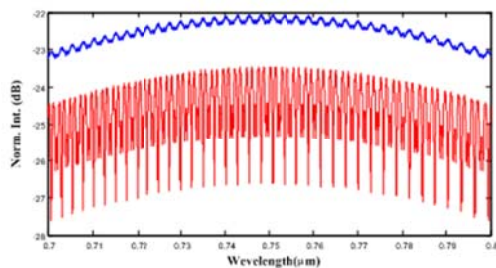
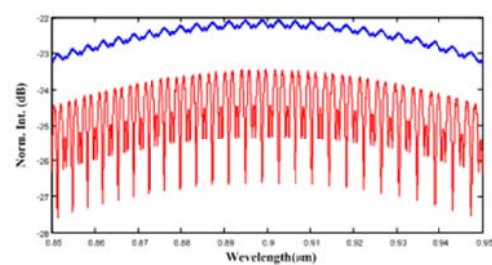
Table 4.12 The effects of ring radius size variations on optical output signal

Ring Radius Size (μm)		Depth of well (dB)	Width of well (nm)	FSR (nm)	Velocity ($\mu\text{m/s}$)
R_{ad}	$R_R = R_L$				
4	2	1.68	6	58	2.716
6	3	1.59	5	37	3.029
8	4	1.60	3	29	2.984
10	5	1.58	3	22	3.030
12	6	1.59	2	19	3.027
14	7	1.59	1	16	3.031
16	8	1.58	1	15	3.039
18	9	1.59	1	12	3.032
20	10	1.58	1	11	3.043

The increase of ring radius size is inversely proportional to the width of well and FSR. However, velocity is directly proportional while depth is insignificant.

- Center Wavelength of Input Signal

This research has studied the effects of center wavelength variation on the output signal properties. The center wavelength input signals are varied from 0.700 to 1.700 μm . The coupled waveguides and the microring waveguide are made from InGaAsP/InP. The intensity coupling coefficient is assigned as the followings: $\kappa_1 = 0.9$, $\kappa_2 = \kappa_4 = 0.35$, $\kappa_3 = 0.1$ and the microring radius are $R_{ad} = 20 \mu\text{m}$, $R_R = R_L = 10 \mu\text{m}$. Figure 4.20 shows the results of the center wavelength input signal changes and the summary of center wavelength input signal effects on the output properties is shown in Table 4.13.

(a) Center wavelength, $\lambda_0 = 750 \text{ nm}$ (b) Center wavelength, $\lambda_0 = 900 \text{ nm}$

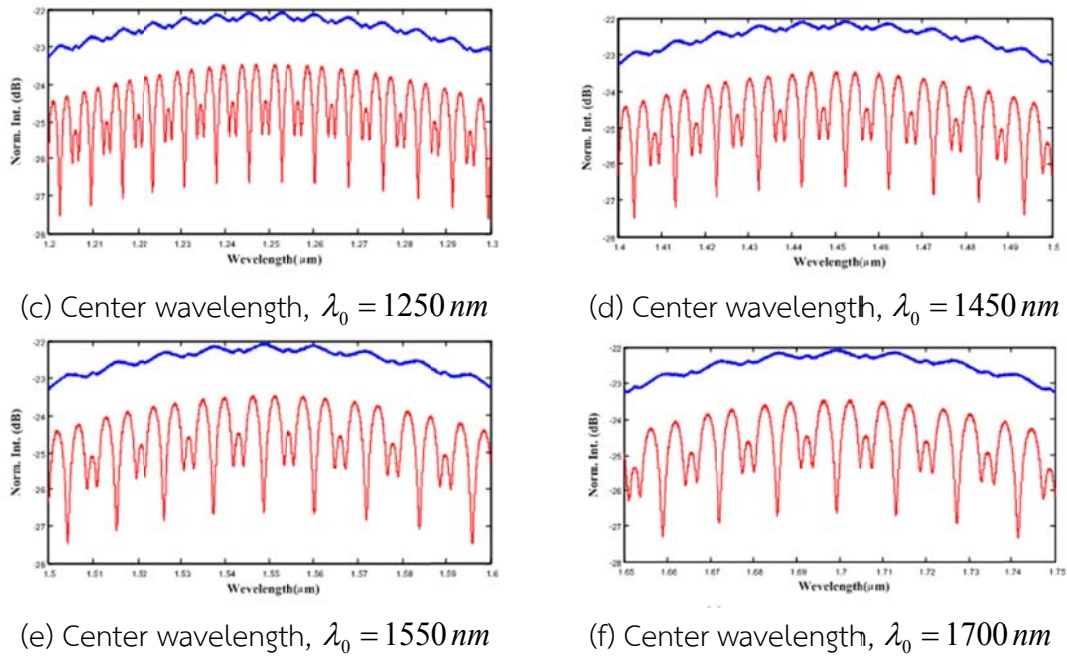


Figure 4.20 The comparison of wavelength effects of MCADM

Table 4.13 The effects of the input center wavelength variations on optical output signal

Input Center Wavelength(nm)	Depth of well (dB)	Width of well (nm)	FSR (nm)	Velocity ($\mu\text{m/s}$)
750	1.58	0.3	2.7	3.044
850	1.58	0.4	3.5	3.135
900	1.58	0.5	3.9	3.041
1250	1.58	1	8	3.039
1450	1.58	1	10	3.041
1500	1.58	1	10	3.020
1550	1.58	2	11	3.043
1600	1.58	2	12	3.034
1700	1.59	2	14	3.112

The increase of the input center wavelength is directly proportional to the width of well and FSR. Nonetheless, the depth of well is insignificant while velocity is ambiguous.

- Velocity

After the suitable parameter specifications of MCADM are determined, the parameters (the intensity coupling coefficients, the ring radius size, the refractive

index of material, and the input center wavelength) are used for velocity approximation. Considering the constrained parameters, microring waveguide is made from InGaAsP/InP. The intensity coupling coefficients are assigned as the followings: $\kappa_1 = 0.9$, $\kappa_2 = \kappa_4 = 0.35$, $\kappa_3 = 0.1$, the ring radius ($R_{ad} = 20 \mu m$, $R_R = R_L = 10 \mu m$). The input signal is Gaussian with the center wavelength (λ_0) at $1.550 \mu m$. Based on the relation of intensity values and kinetic energy within the condition of no thermal effect and other losses, the velocity can be approximated and shown in Figure 4.21.

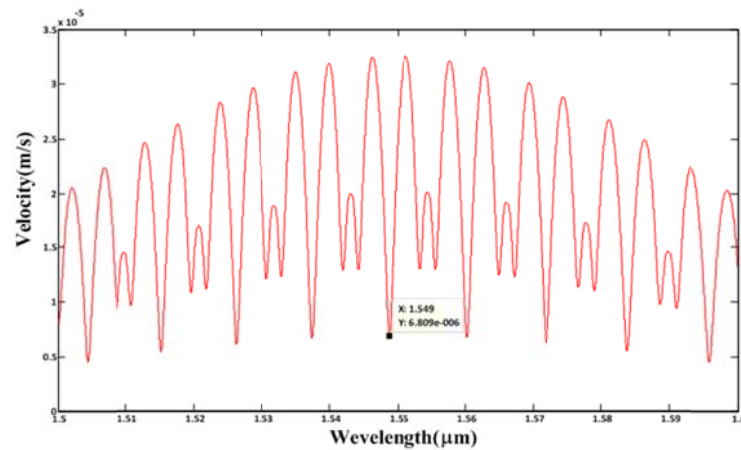


Figure 4.21 The comparison of velocity with respect to the wavelength of MCADM

4.1.4 The Suitable Parameters Specification for 3 Modulators

From the primary suitable parameter specification results in section 1.1.1 - 1.1.3, the suitable parameters for each modulator can be summarized and shown in Table 4.14. The first column demonstrates the types of modulator and the second presents the intensity coupling coefficient, the third represents the suitable material selected. The fourth shows the microring radius size consistent with the finding of the previous study conducted by Hong Cai and Andrew W. Poon [15] and the final column illustrates the most commonly used center wavelength of input signal for optical communication system.

Table 4.14 The suitable parameters of 3 modulators

Modulator Type	Intensity Coupling Coefficient	Material	Ring Radius Size (μm)	Center Wavelength (nm)
RADM	$\kappa_1 = 0.7, \kappa_2 = 0.3$	<i>InGaAsP</i>	$R_{ad} = 20$	$\lambda_0 = 1550$
CADM	$\kappa_1 = 0.7, \kappa_2 = 0.3$	<i>InGaAsP</i>	$R_{ad} = 20$	$\lambda_0 = 1550$
MCADM	$\kappa_1 = 0.9, \kappa_2 = 0.35$ $\kappa_3 = 0.1, \kappa_4 = 0.35$	<i>InGaAsP</i>	$R_{ad} = 20$ $R_R = R_L = 10$	$\lambda_0 = 1550$

4.2 Experimental Results of the Proposed System

As explained in section 3.3.4, the physical geometry of system in Figure 4.22 is simulated based on the suitable parameters of MCADM. Furthermore, the objective of this system is to compare its efficiency with 2 modulator devices (RADM and CADM). The best parameters for RADM and CADM are prepared in Table 4.14. The input signals of simulation test are Gaussian and Dark Soliton, which are fed into the input and add port respectively. The four investigated parameters are the intensity coupling coefficient (κ), the ring radius size (R_{ad}, R_R, R_L), the material properties (n_0, n_2) and the center wavelength (λ_0) of the input signal. From the suitable parameters of mathematical transfer function analysis in Table 3.5 and primary suitable parameter specification results in Table 4.14, the suitable parameters of MCADM can be concluded in Table 4.15.

Table 4.15 The parameter simulation of MCADM

No.	Parameter	Symbol	Value
I.	Gaussian beam peak power (a.u)	E_{i1}	1
II.	Dark Soliton peak power (a.u)	E_{i2}	1, 35 fs
III.	The waveguide coupling loss coefficient (db/mm)	α	5×10^{-5}
IV.	The intensity coupling loss coefficient	γ	0.01
V.	The effective core area of MCADM (μm^2)	A_{eff}	1.44
VI.	Linear refractive index of InGaAsP	n_0	3.34
VII.	Nonlinear refractive index of InGaAsP (cm^2/W)	n_2	4.27×10^{-17}
VIII.	Center wavelength of input signal (nm)	λ_0	1550
IX.	The center microring radius (μm)	R_{ad}	20
X.	The right microring radius (μm)	R_R	10
XI.	The left microring radius (μm)	R_L	10
XII.	The intensity coupling coefficient	κ_1	0.9
		κ_2	0.35
		κ_3	0.1
		κ_4	0.35

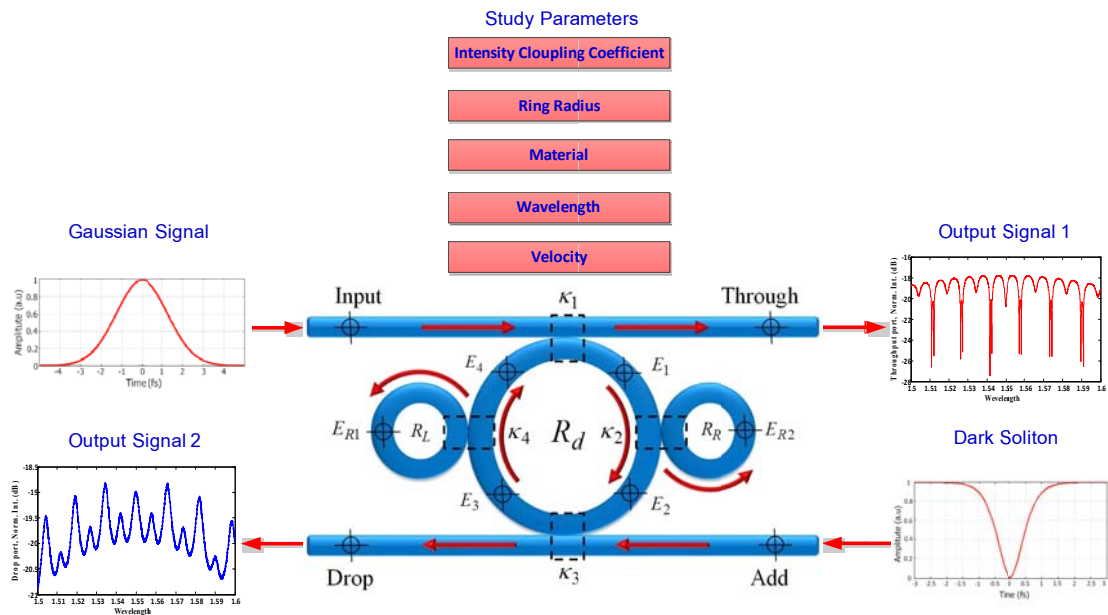
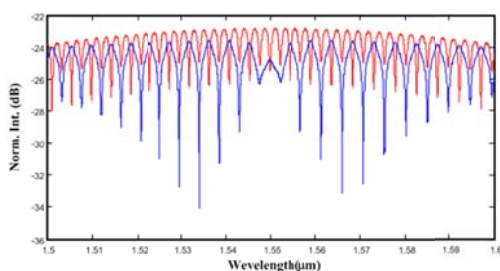


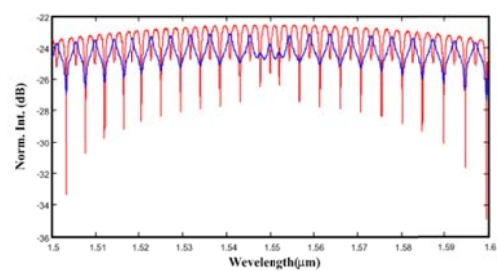
Figure 4.22 The physical geometry of the proposed system

4.2.1 Intensity Coupling Coefficient

The aim of this investigation is to study the intensity coupling coefficient (κ) variation effects on the output signal properties of 3 modulator devices based on the suitable parameters of each device and the other parameters are set constant. The other parameters are considered when fabricating microring modulator and material used is InGaAsP. The input center wavelength (λ_0) is 1550 nm, the ring radius (R_{ad}) parameter of RADM, CADM and center microring radius of MCADM is 20 μm , and the left and right microring radius (R_L, R_R) of MCADM is 10 μm . The experimental results will be presented according to the types of modulator started by RADM, CADM and MCADM as shown in Figure 4.23-4.26.



(a) $\kappa_1 = 0.90, \kappa_2 = 0.10$



(b) $\kappa_1 = 0.70, \kappa_2 = 0.30$

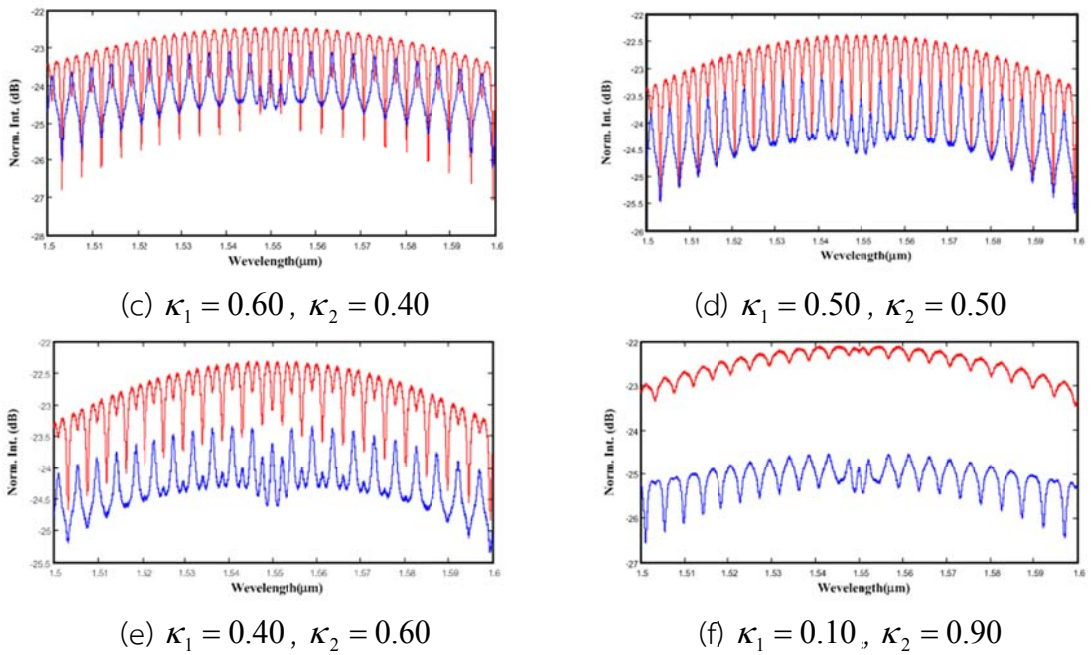


Figure 4.23 The comparison of the intensity coupling coefficient effects of RADM

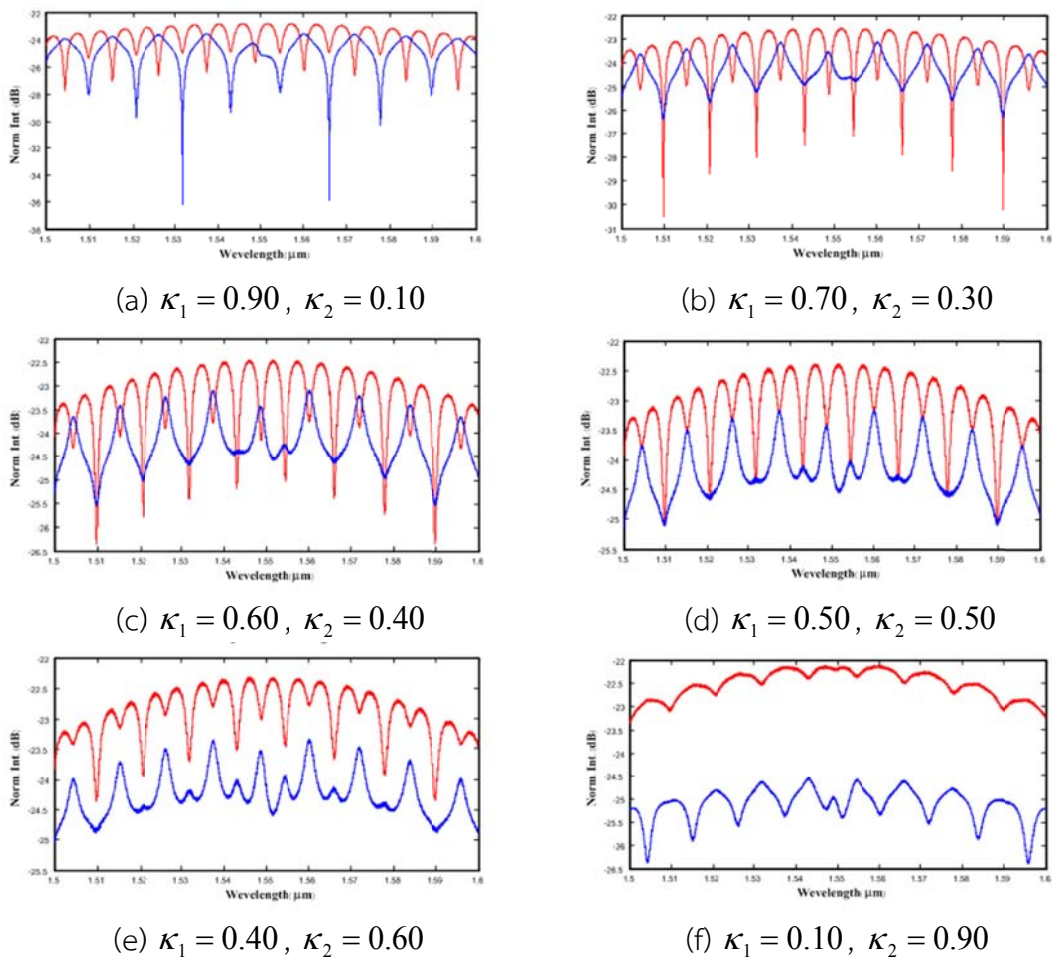


Figure 4.24 The comparison of the intensity coupling coefficient effects of CADM

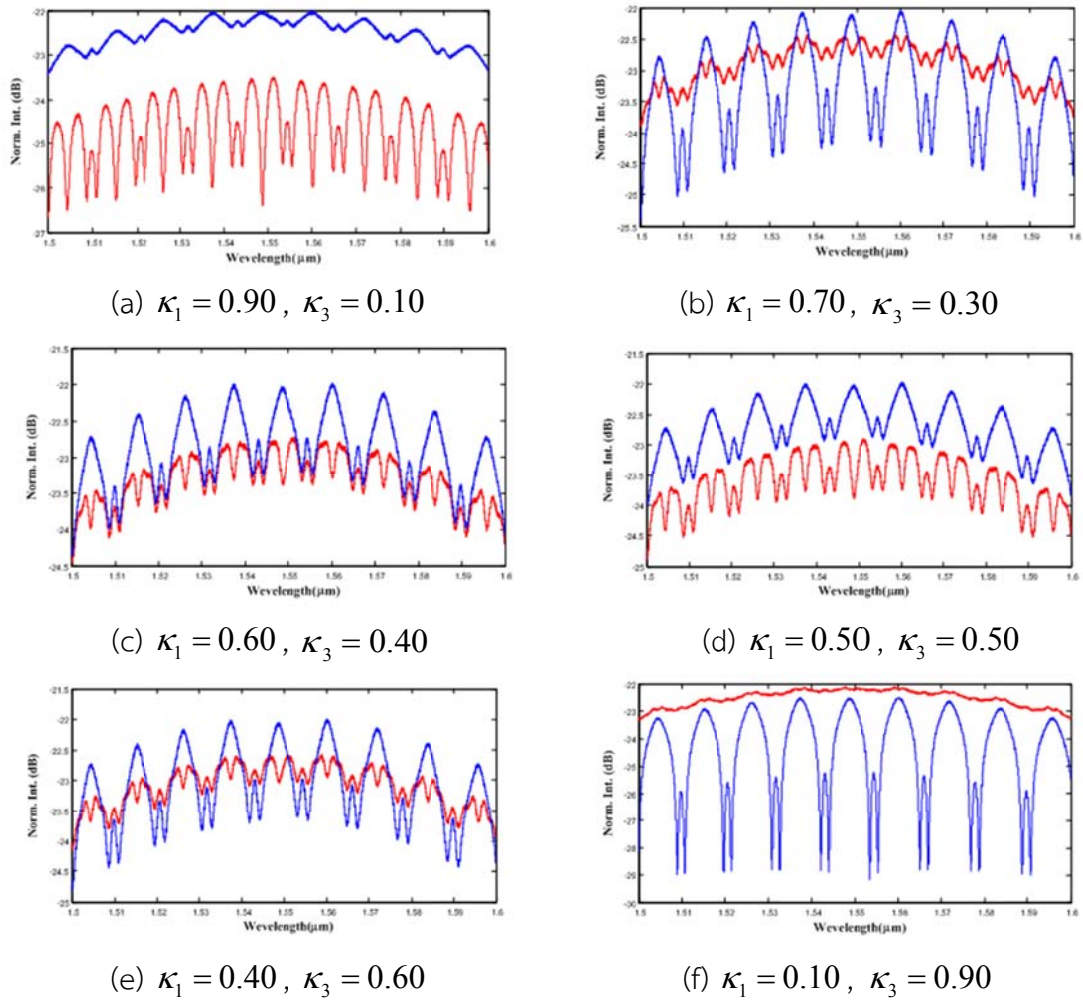


Figure 4.25 The comparison of the intensity coupling coefficient effects of MCADM

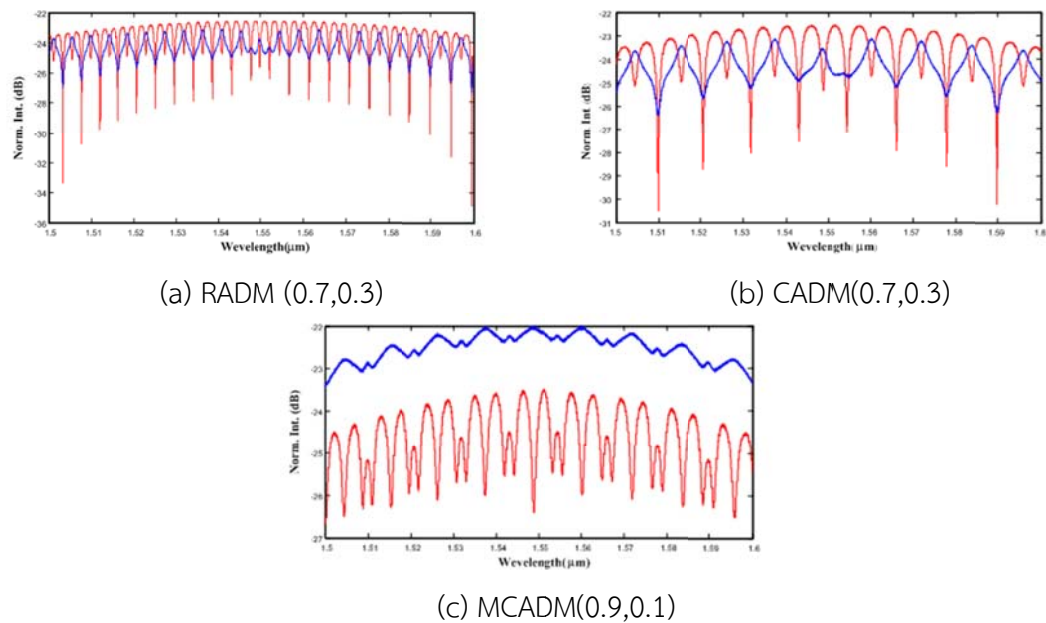


Figure 4.26 The comparison of the intensity coupling coefficient effects of 3 modulators

4.2.2 Materials

This section presents the waveguide material effects on 3 modulators output signal properties. The other parameters such as intensity coupling coefficients, ring radius, wavelength are fixed, while the materials for fabricating microring resonator is varied. The fabricated material properties in Table 2.1 and 4.1 are often used for the simulation. The intensity coupling coefficient of RADM and CADM are $\kappa_1 = 0.7$, $\kappa_2 = 0.3$ and MCADM are assigned as $\kappa_1 = 0.9$, $\kappa_2 = \kappa_4 = 0.35$ and $\kappa_3 = 0.1$. The microring radius of RADM and CADM are $R_{ad} = 20 \mu m$ and MCADM are $R_{ad} = 20 \mu m, R_R = R_L = 10 \mu m$ and input signals are Gaussian and Dark Soliton with center wavelength of $\lambda_0 = 1550 nm$. Figure 4.27-4.30 shows the simulation results of different materials and the summary of material effects on the 3 modulator output properties.

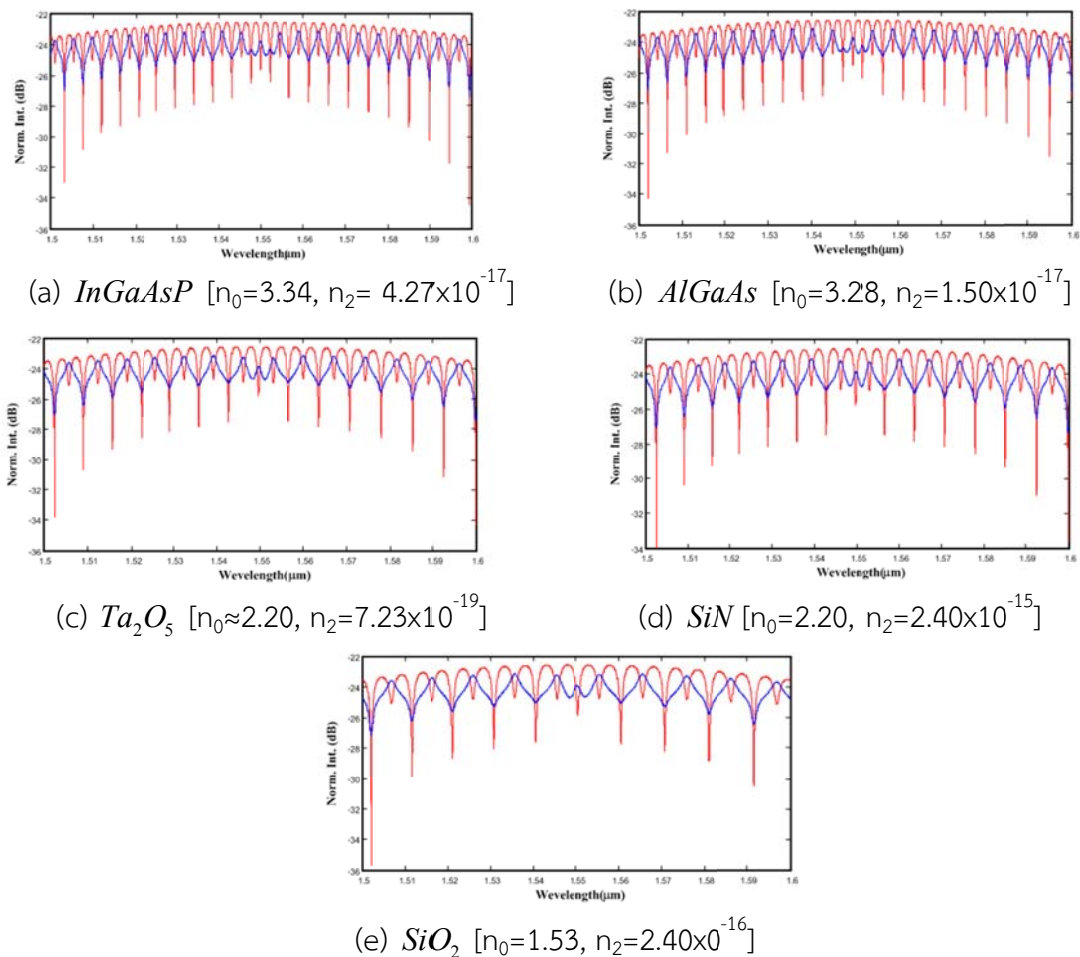


Figure 4.27 The comparison of the fabricated materials effects of RADM

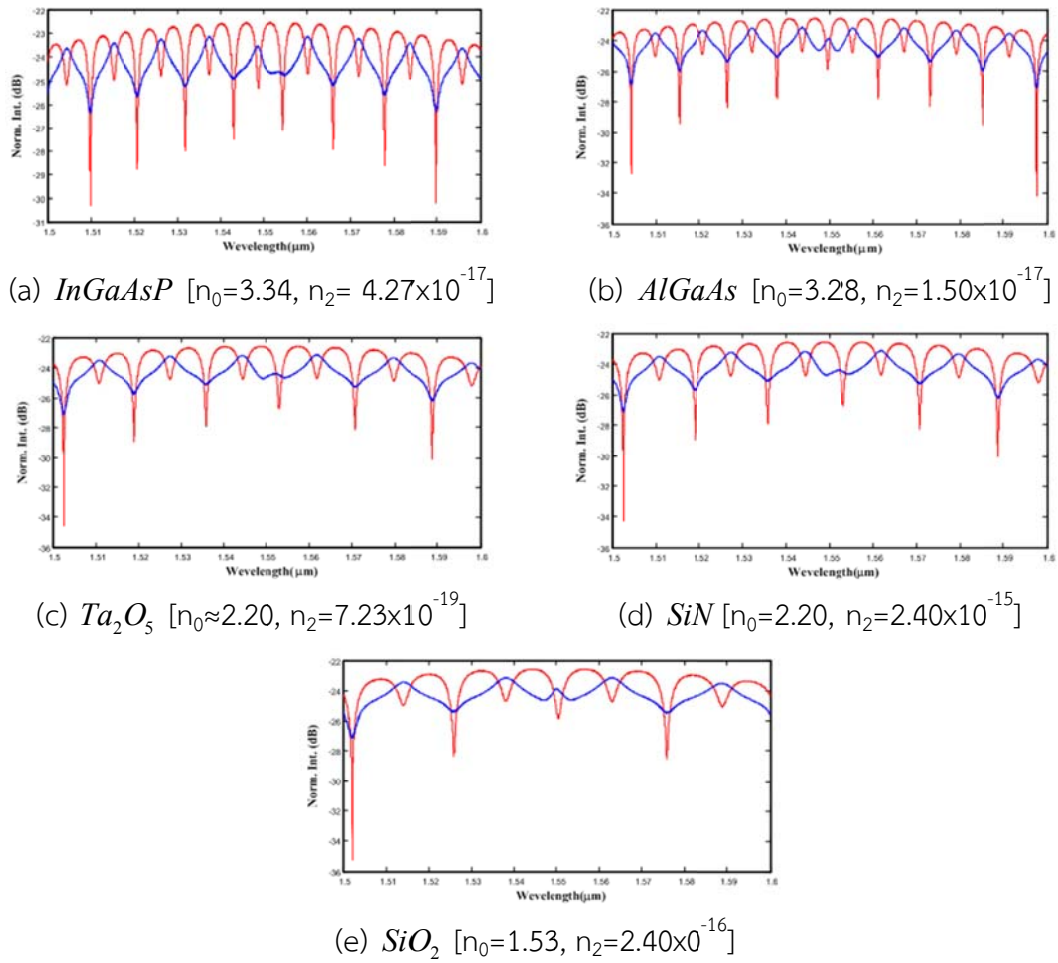
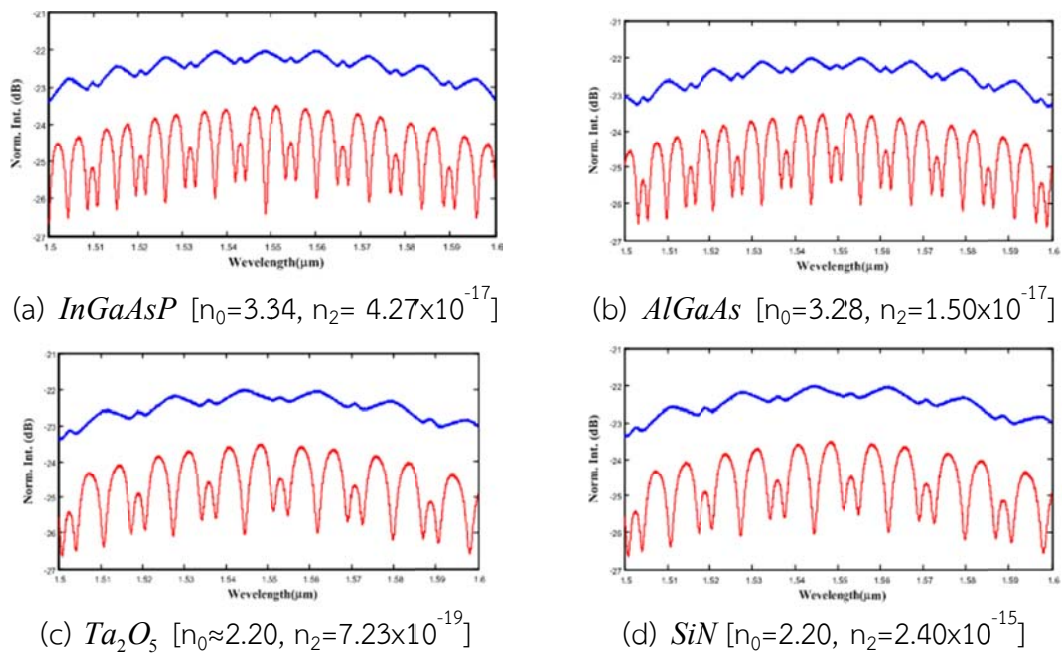
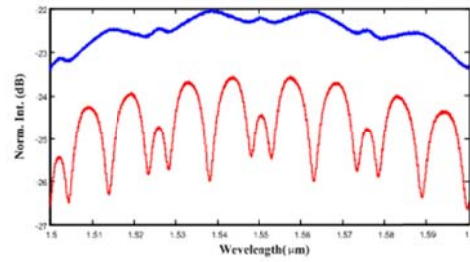


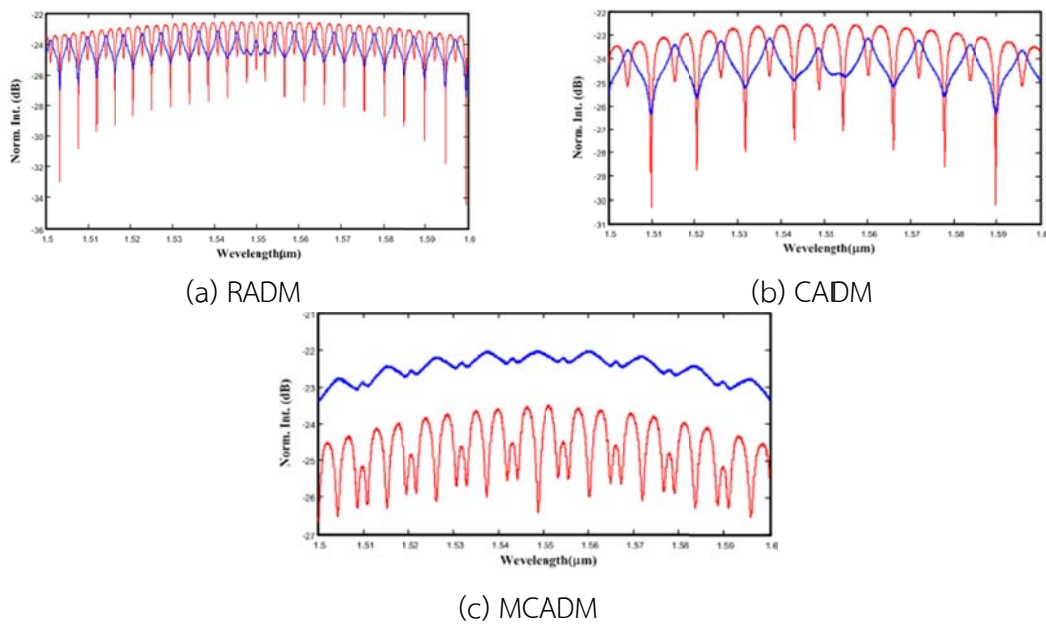
Figure 4.28 The comparison of the fabricated materials effects of RADM





(e) SiO_2 [$n_0=1.53$, $n_2=2.40 \times 10^{-16}$]

Figure 4.29 The comparison of the fabricated materials effects of RADM



(a) RADM

(b) CADM

(c) MCADM

Figure 4.30 The comparison of the fabricated materials effects of 3 modulators

4.2.3 Ring Radius Size

The objective of the investigation is to study the ring radius (R_{ad} , R_R , R_L) variation effects on output signal properties of 3 modulator devices. Therefore, this experiment chooses the ring radius of RADM, CADM and center ring radius of MCADM varying from 2 to 20 μm . The left and right (R_L , R_R) microring of MCADM are varied from 1 to 10 μm , the other parameters such as intensity coupling coefficient of RADM and CADM are $\kappa_1 = 0.7$, $\kappa_2 = 0.3$ and MCADM are assigned as $\kappa_1 = 0.9$, $\kappa_2 = \kappa_4 = 0.35$ and $\kappa_3 = 0.1$, the refractive index of material ($n_0(\text{InGaAsP})$, $n_2(\text{InGaAsP})$), two input signals wavelength ($\lambda_0 = 1550 \text{ nm}$) are fixed. Figure 4.31-4.34 shows the simulation results of ring radius variation.

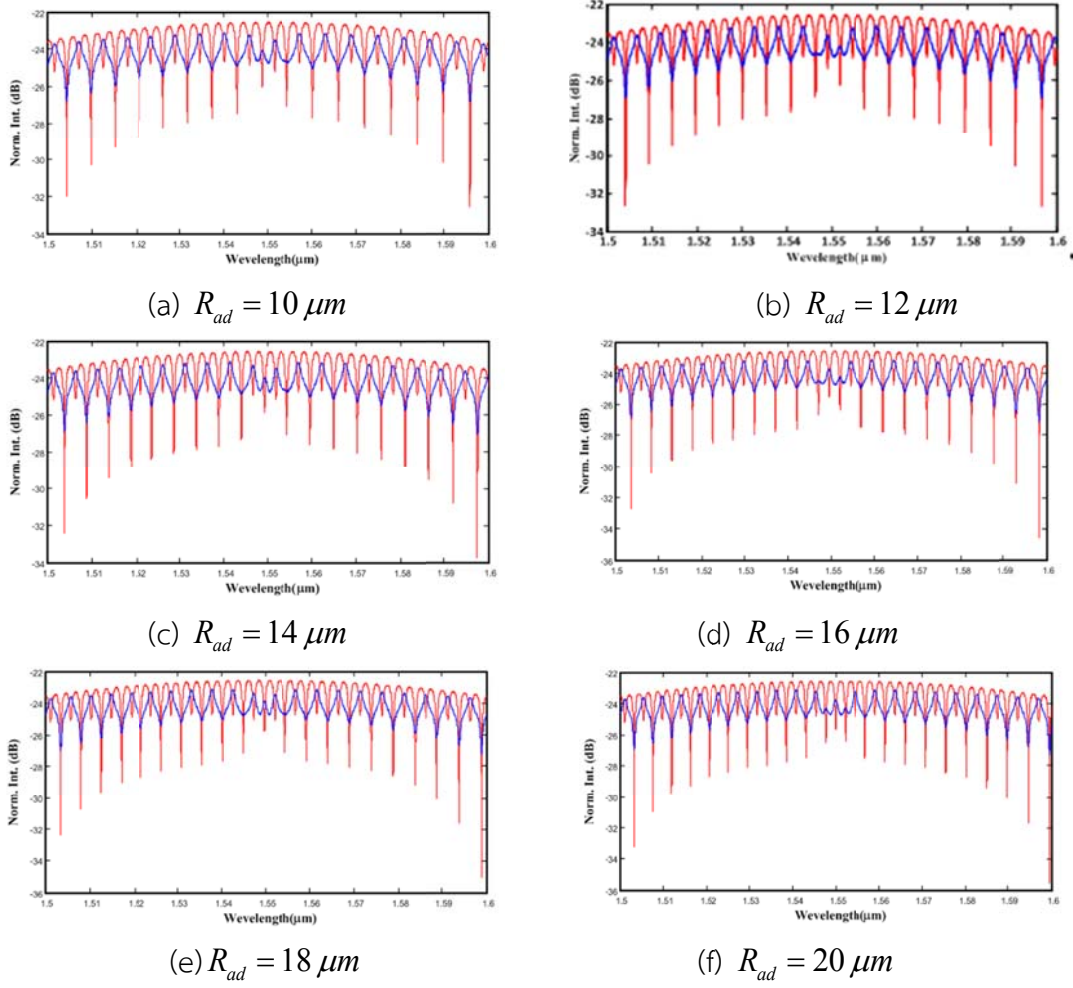
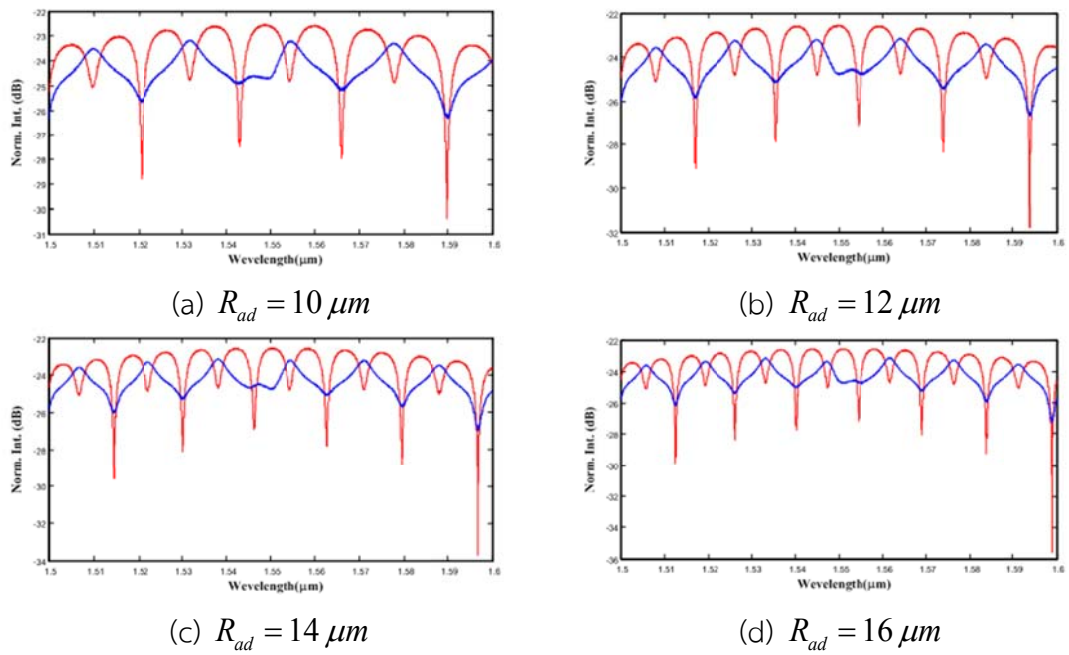
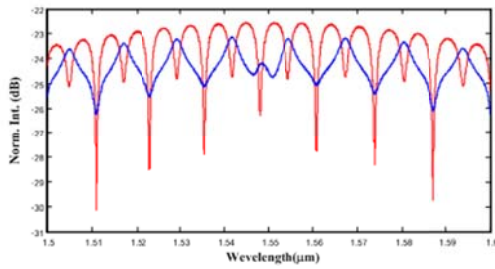
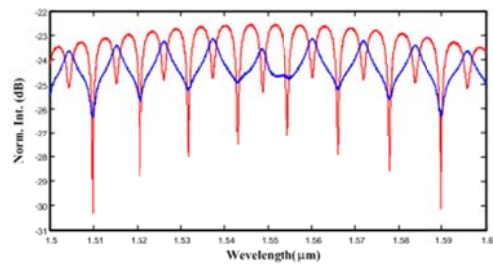


Figure 4.31 The comparison of ring radius effects of RADM



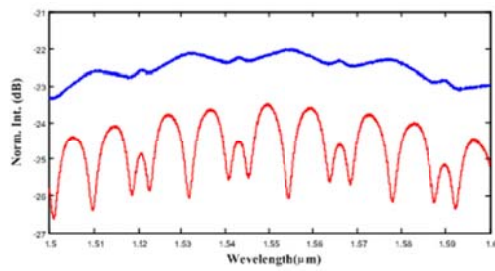


(e) $R_{ad} = 18 \mu m$

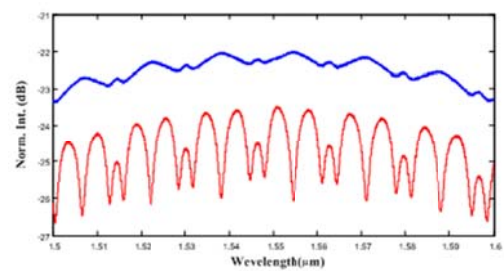


(f) $R_{ad} = 20 \mu m$

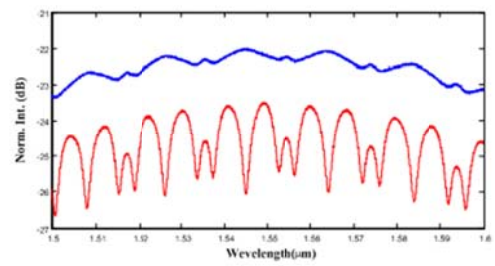
Figure 4.32 The comparison of the ring radius effects of CADM



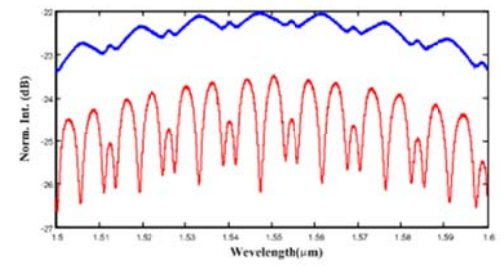
(a) $R_d = 10 \mu m, R_L = R_R = 5 \mu m$



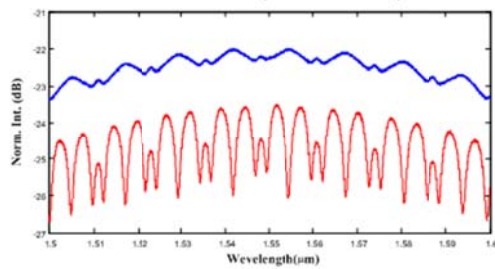
(b) $R_d = 12 \mu m, R_L = R_R = 6 \mu m$



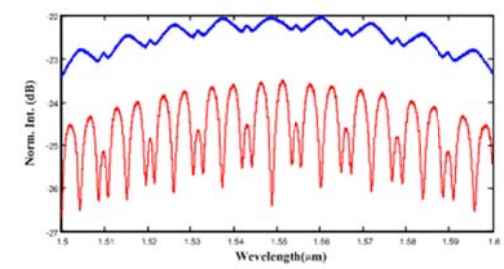
(c) $R_d = 14 \mu m, R_L = R_R = 7 \mu m$



(d) $R_d = 16 \mu m, R_L = R_R = 8 \mu m$

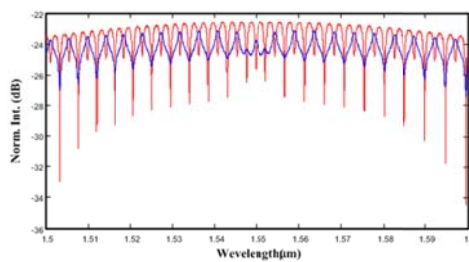


(e) $R_d = 18 \mu m, R_L = R_R = 9 \mu m$

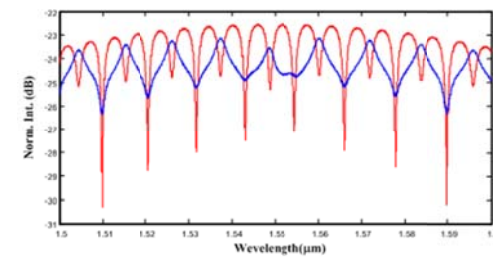


(f) $R_d = 20 \mu m, R_L = R_R = 10 \mu m$

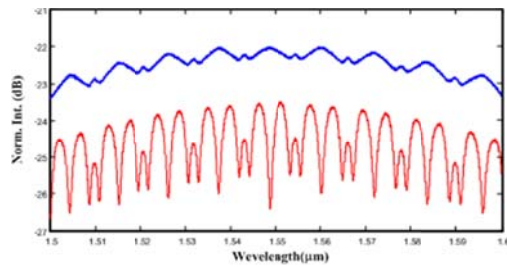
Figure 4.33 The comparison of the ring radius effects of MCADM



(a) RADM



(b) CADM

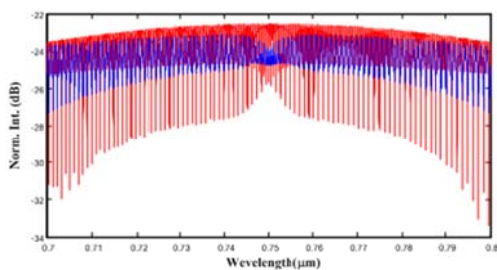
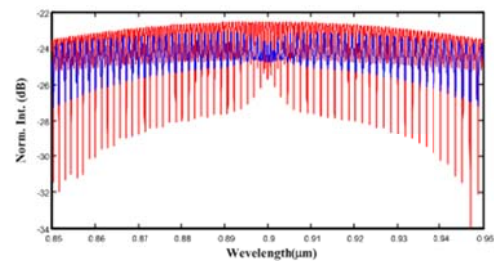
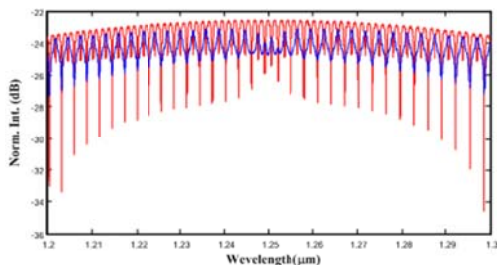
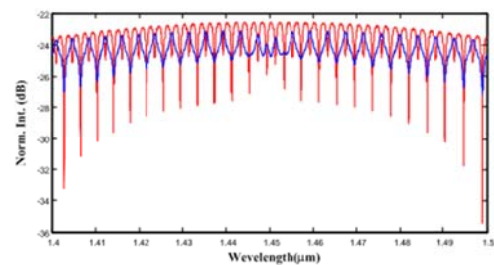


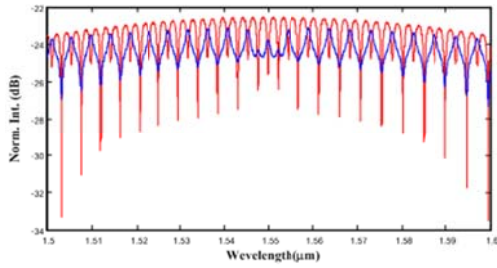
(c) MCADM

Figure 4.34 The comparison of the ring radius effects of 3 modulators

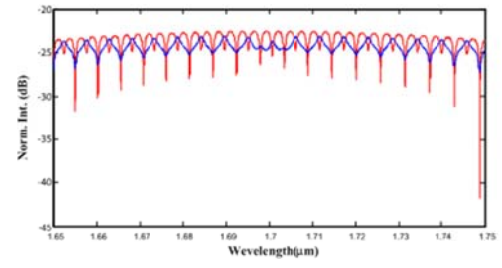
4.2.4 Center Wavelength of Input Signal

The objective of the experiment is to study the effect of center wavelength variation on the output signal properties of 3 modulator devices. The center wavelengths of input signals are varied from 0.700 to 1.700 μm . The coupled waveguides and the microring waveguide are made from InGaAsP/InP, intensity coupling coefficients of RADM and CADM are $\kappa_1 = 0.7$, $\kappa_2 = 0.3$ and MCADM are assigned to $\kappa_1 = 0.9$, $\kappa_2 = \kappa_4 = 0.35$ and $\kappa_3 = 0.1$. The microring radii of RADM and CADM are $R_{ad} = 20 \mu\text{m}$ and MCADM are $R_{ad} = 20 \mu\text{m}$, $R_R = R_L = 10 \mu\text{m}$. Figure 4.35-4.38 shows the results of the center wavelength input signal changes and the summary of the center wavelength of input signal effects on the output properties is shown in Table 4.16.

(a) Center wavelength, $\lambda_0 = 750 \text{ nm}$ (b) Center wavelength, $\lambda_0 = 900 \text{ nm}$ (c) Center wavelength, $\lambda_0 = 1250 \text{ nm}$ (d) Center wavelength $\lambda_0 = 1450 \text{ nm}$

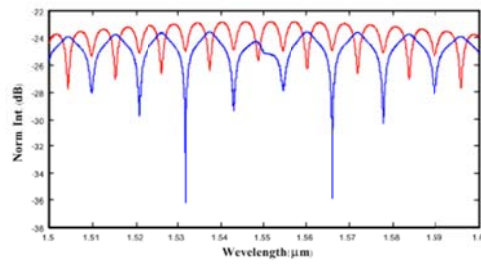


(e) Center wavelength $\lambda_0 = 1550 \text{ nm}$

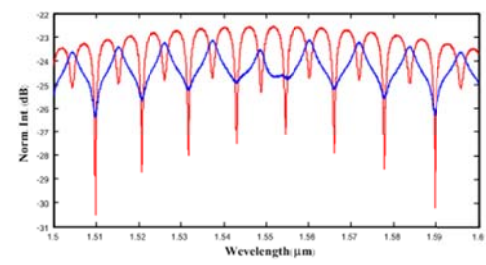


(f) Center wavelength $\lambda_0 = 1700 \text{ nm}$

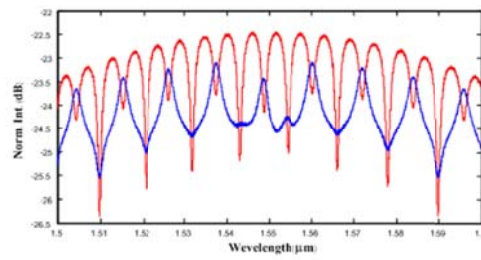
Figure 4.35 The comparison of the center wavelength of input signal effects of RADM



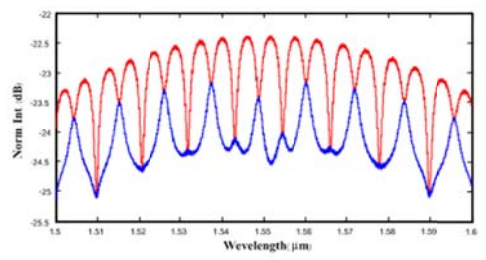
(a) $\kappa_1 = 0.90, \kappa_2 = 0.10$



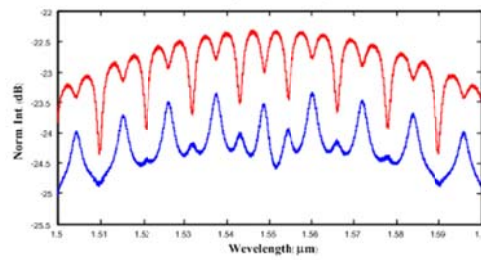
(b) $\kappa_1 = 0.70, \kappa_2 = 0.30$



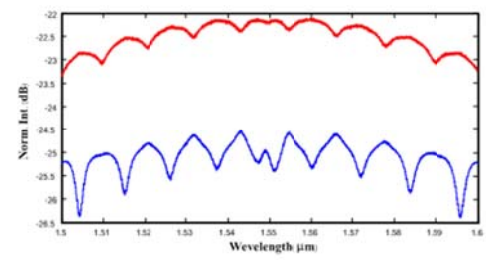
(c) $\kappa_1 = 0.60, \kappa_2 = 0.40$



(d) $\kappa_1 = 0.50, \kappa_2 = 0.50$

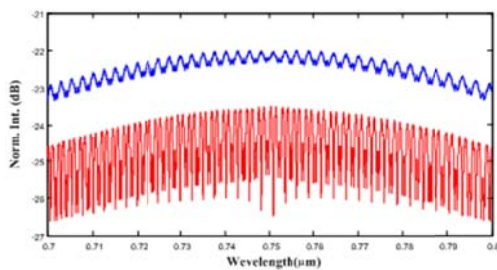


(e) $\kappa_1 = 0.40, \kappa_2 = 0.60$

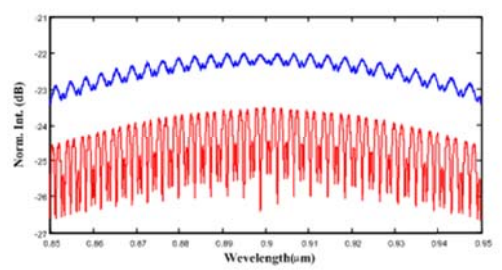


(f) $\kappa_1 = 0.10, \kappa_2 = 0.90$

Figure 4.36 The comparison of the center wavelength of input signal effects of CADM



(a) Center wavelength, $\lambda_0 = 750 \text{ nm}$



(b) Center wavelength, $\lambda_0 = 900 \text{ nm}$

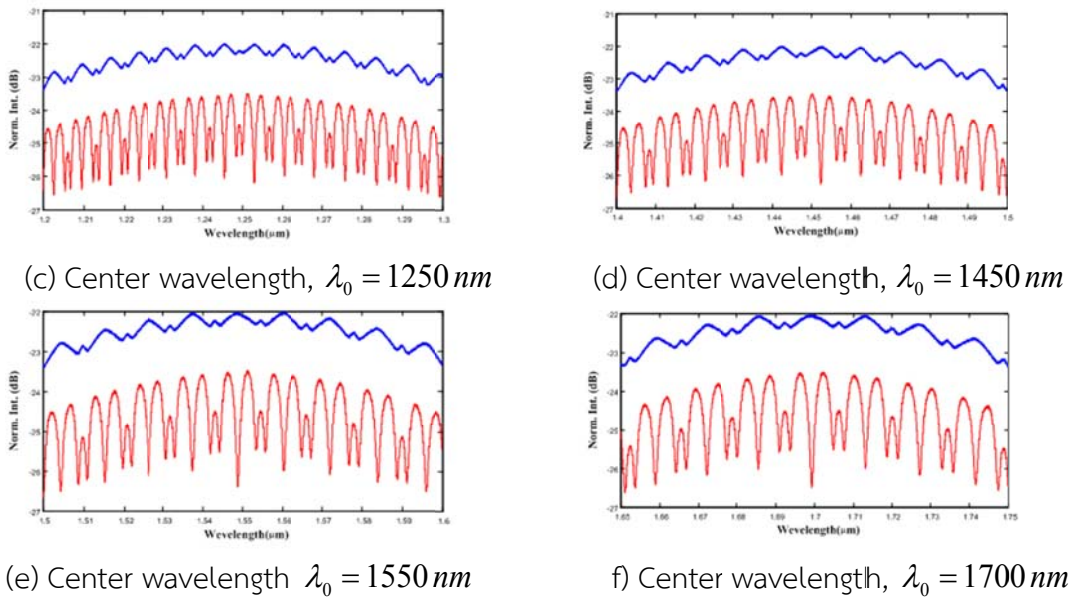


Figure 4.37 The comparison of the center wavelength of input signal effects of MCADM

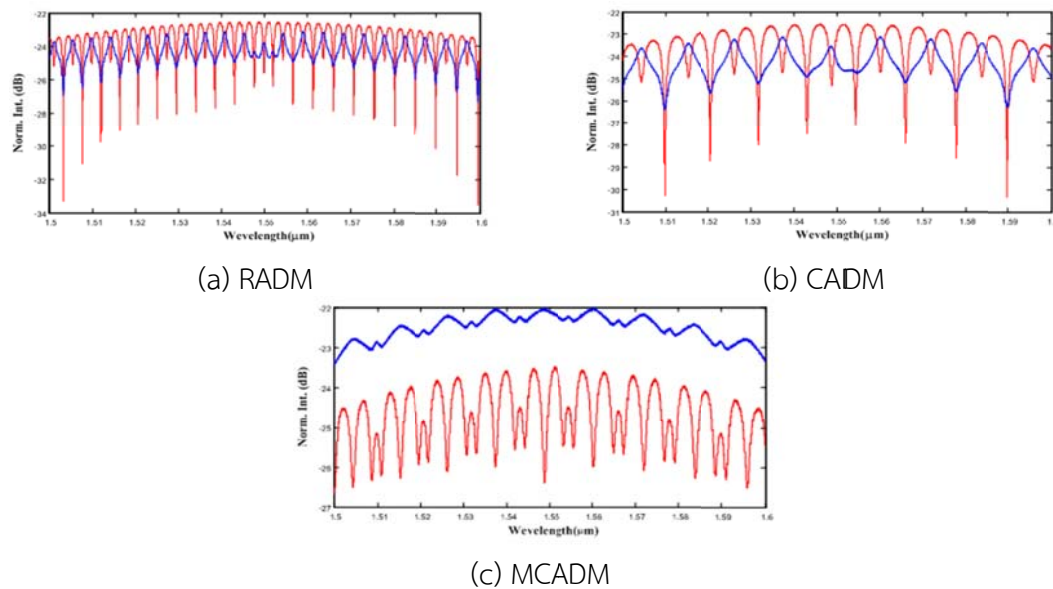


Figure 4.38 The comparison of the center wavelength of input signal effects of 3 modulators

Table 4.16 The comparison of the center wavelength of input signal effects of 3 modulator devices

Feature	RADM	CADM	MCADM
Depth of well (dB)	1.530	1.390	2.880
Width of well (nm)	0.400	1.000	2.000
Free spectral range (nm)	2.000	6.000	16.000
Velocity ($\mu\text{m/s}$)	5.039	5.877	8.975

4.2.5 Velocity

After the all parameter simulations of 3 modulator devices are finished, the suitable parameters are used for velocity approximation and comparison. The constrained parameters are microring waveguide which are made from InGaAsP/InP, intensity coupling coefficients of RADM and CADM are $\kappa_1 = 0.7$, $\kappa_2 = 0.3$ and MCADM are assigned as $\kappa_1 = 0.9$, $\kappa_2 = \kappa_4 = 0.35$ and $\kappa_3 = 0.1$. The microring radius of RADM and CADM are $R_{ad} = 20 \mu m$ and MCADM are $R_{ad} = 20 \mu m, R_R = R_L = 10 \mu m$ and the input signal is Gaussian with the center wavelength (λ_0) of $1.550 \mu m$. Considering the relation of intensity values and kinetic energy within the condition of no thermal effect and other losses, the velocity can be approximated and shown in Figure 4.39.

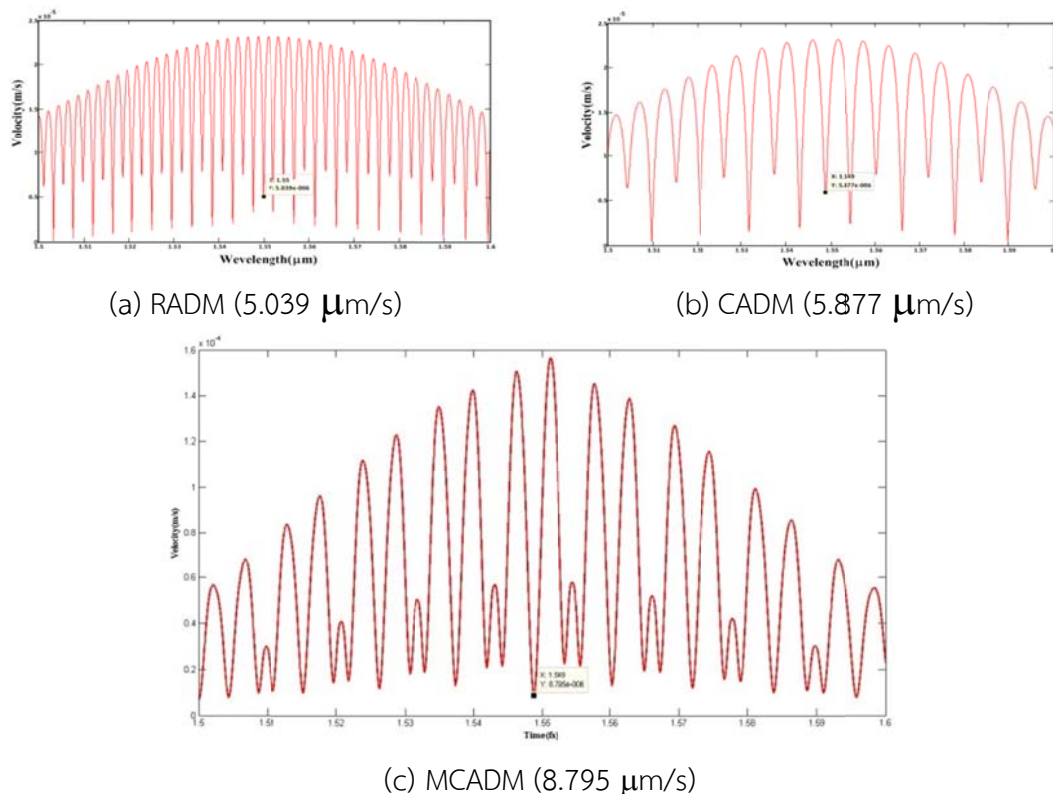


Figure 4.39 The velocity comparison between 3 modulators

4.3 The Performance Comparison of 3 Modulators

4.3.1 Performance Comparison of Primary Suitable Parameters Specification

This presents the performance comparison of the primary suitable parameter specifications for 3 modulators. The parameter is compared in terms of the depth of well, the width of well, the FSR and the velocity. The parameter specifications are shown in Table 4.17.

- Intensity coupling coefficient variation

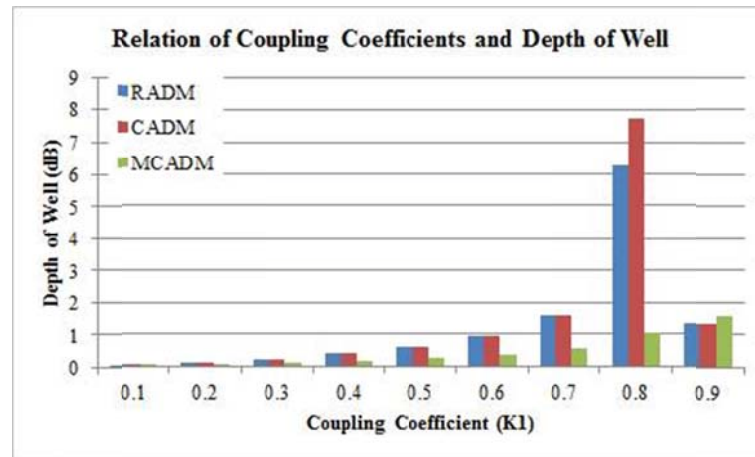


Figure 4.40 The intensity coupling coefficients effects on depth of well

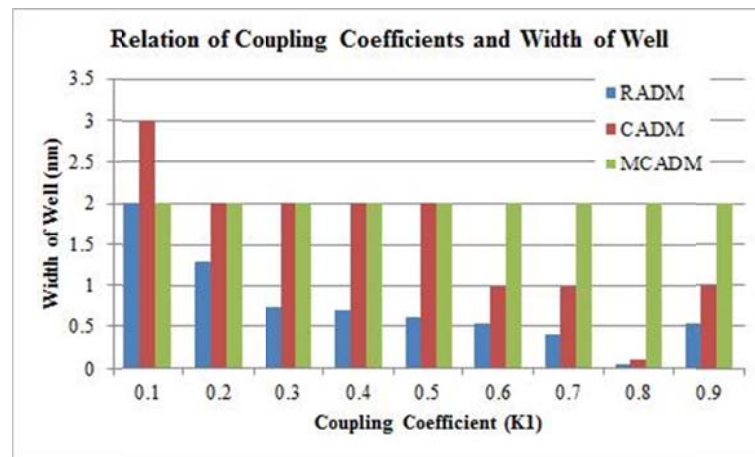


Figure 4.41 The intensity coupling coefficients effects on width of well

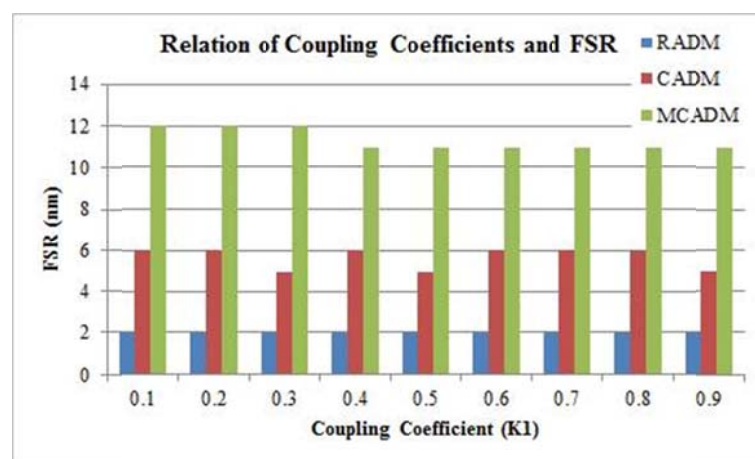


Figure 4.42 The intensity coupling coefficients effects on FSR

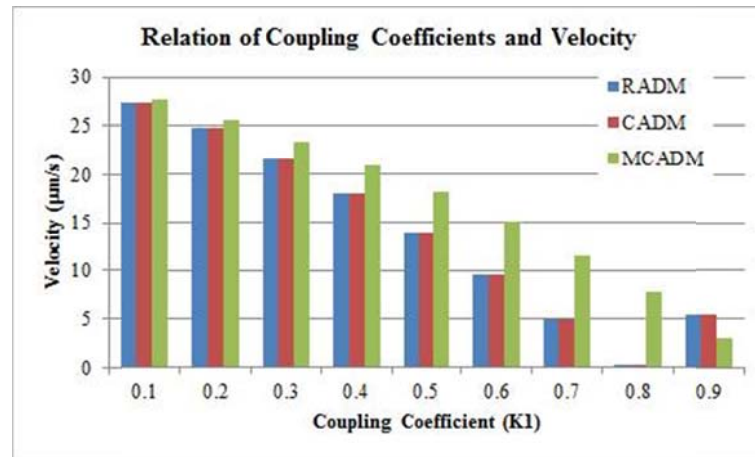


Figure 4.43 The intensity coupling coefficients effects on velocity

Discussion of Figure 4.40-4.43: The increase of the intensity coupling coefficient is direct proportional to the increase of depth of well or the magnitude of gradient force. RADM and CADM, width of well decrease except at the intensity coefficient of 0.9. However, MCADM width of well is constant. The increase of the intensity coupling coefficient is insignificant for FSR value. When the increase of the intensity coupling coefficient value is compared with velocity it is found that its effects results in the decrease of velocity.

- Material variations

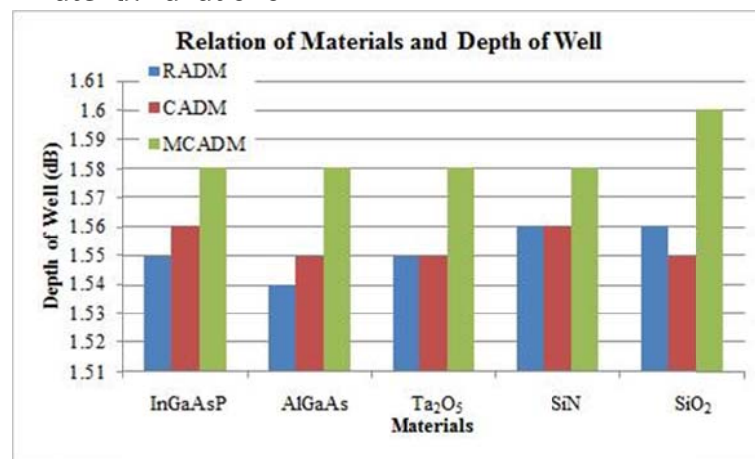


Figure 4.44 The fabricated material effects on depth of well

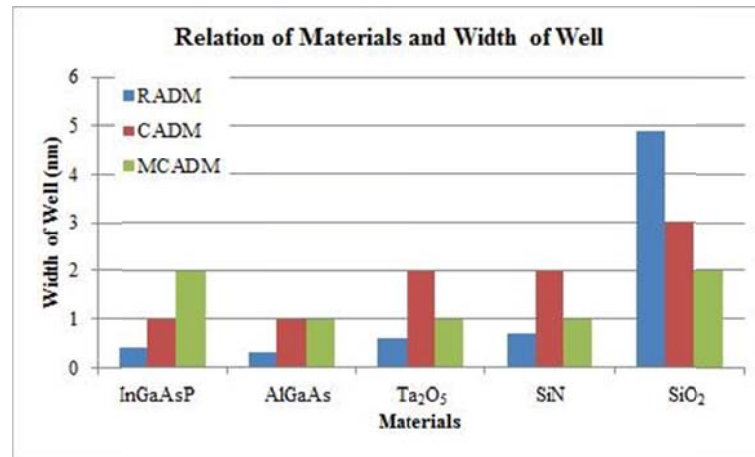


Figure 4.45 The fabricated material effects on width of well

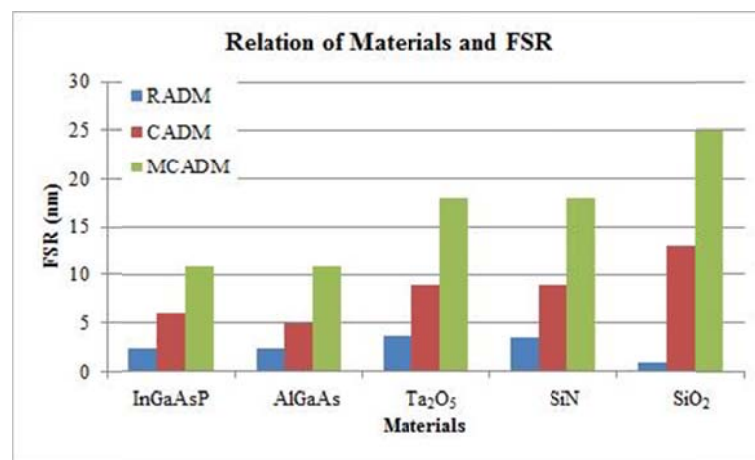


Figure 4.46 The fabricated material effects on FSR

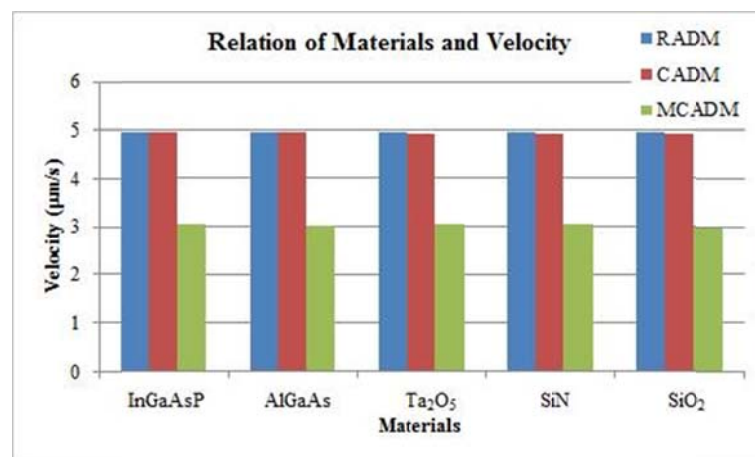


Figure 4.47 The fabricated material effects on velocity

Discussion of Figure 4.44-4.47: The increase of the refractive index of the material is direct proportional to the increase of FSR of three modulator devices. RADM and CADM width of well of is increased while MCADM is ambiguous. Depth

of well is significant when of fabricated material properties are varied. The increase of refractive index is insignificant for the velocity.

- Ring Radius Sizes variations

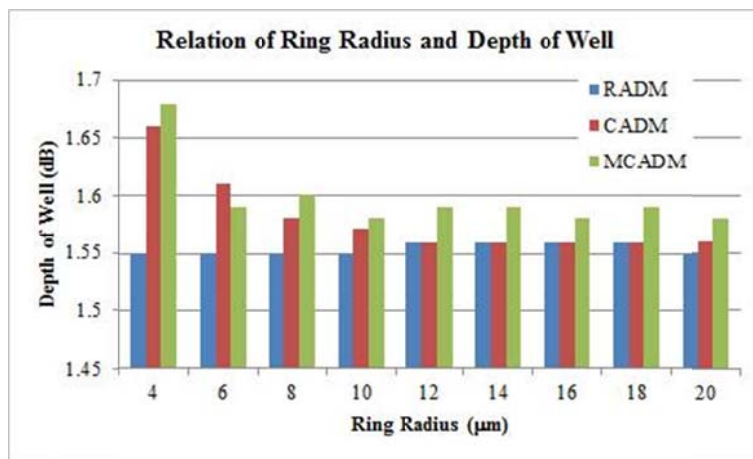


Figure 4.48 The ring radius sizes effects on depth of well

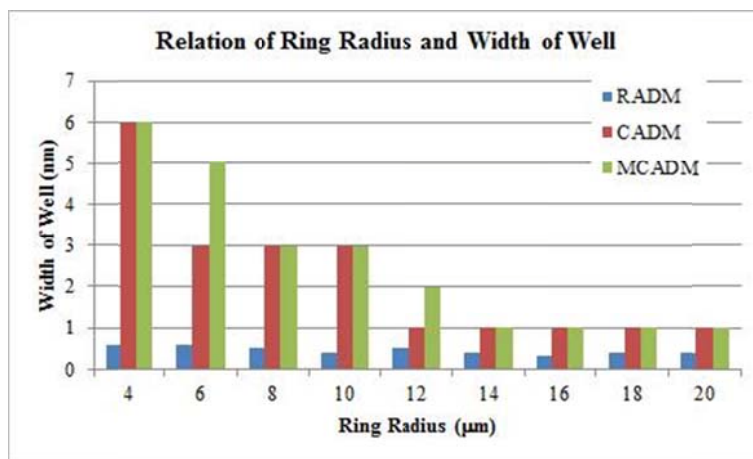


Figure 4.49 The ring radius sizes effects on width of well

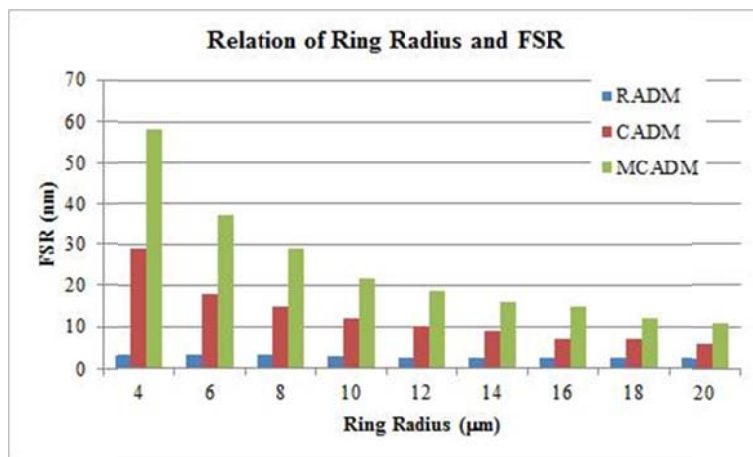


Figure 4.50 The ring radius sizes effects on FSR

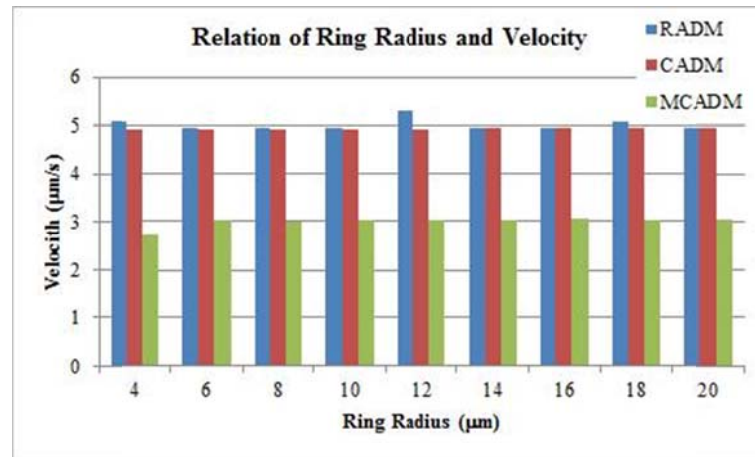


Figure 4.51 The ring radius sizes effects on velocity

Discussion of Figure 4.48-4.51: The increase of center ring radius size of CADM, CADM and MCADM is proportional to the decrease of the depth of well, the width of well and FSR value of three modulator devices. For the MCADM, the increase ratio of left and right ring radius size is determined by Equation (3.4). The change of width of well and depth of well depends upon the additive and subtractive interference within microring. The increase of ring size of 3 modulators does not affect velocity.

- Center wavelength of input signal variations

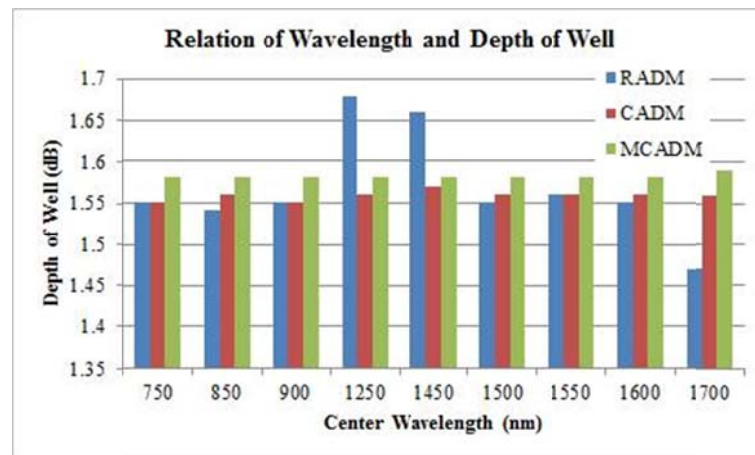


Figure 4.52 The center wavelength of input signal effects on depth of well

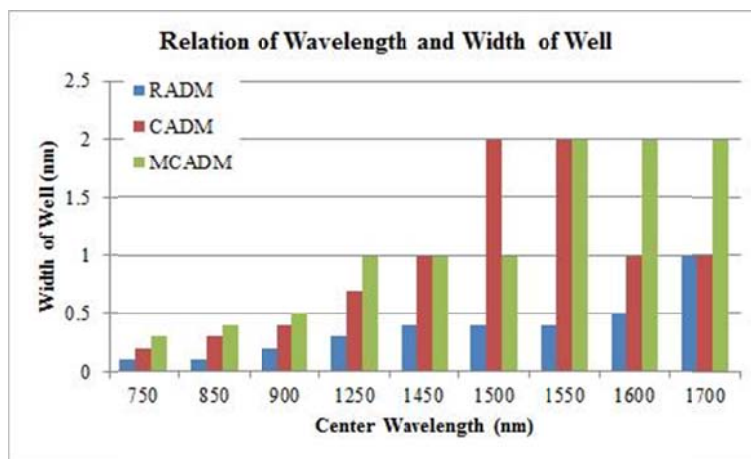


Figure 4.53 The center wavelength of input signal effects on width of well

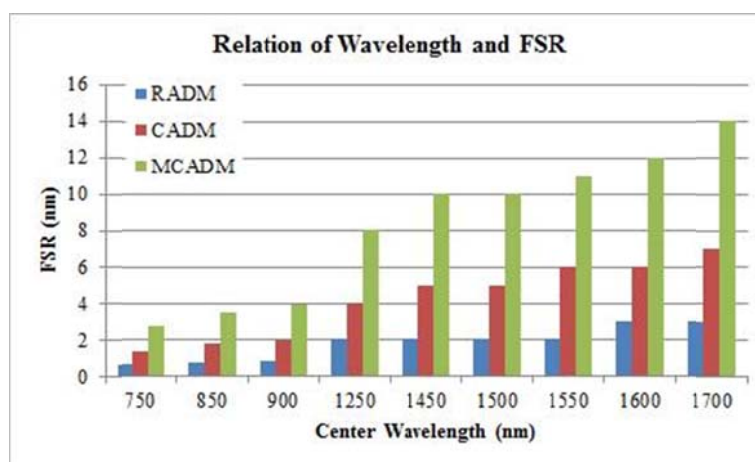


Figure 4.54 The center wavelength of input signal effects on FSR

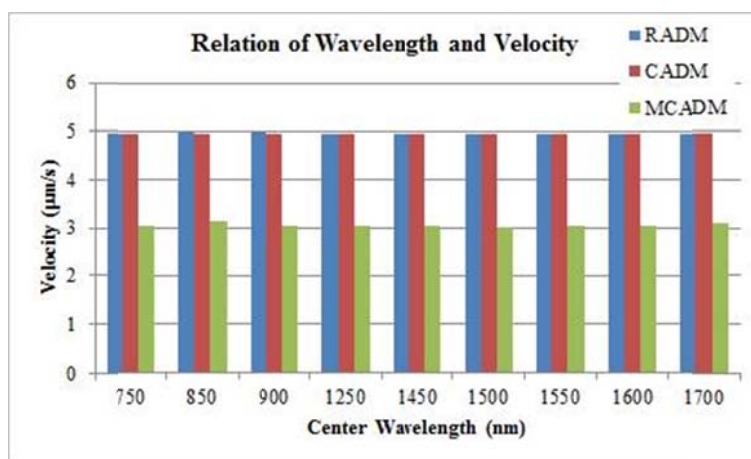


Figure 4.55 The center wavelength of input signal effects on velocity

Discussion of Figure 4.52-4.55: The increase of center wavelength of the input signal is insignificant to depth of well. However, width of well and FSR are direct proportional while velocity does not change.

4.3.2 Discussion of Effected Parameters

From mathematical analysis in section 3.3 and the experimental results in section 4.2, the study parameters is concluded as the followings:

- The variation of the intensity coupling coefficient

The experimental results confirm that the variation of κ_1 and κ_3 is affected by depth of well (magnitude of gradient force) and velocity increases following the increased value of κ_1 and κ_3 while width of well and FSR are insignificant.

- The variation of fabricated material property

The depth of well increases direct proportionally to the increase of refractive index of material value while FSR and velocity decrease or is proportional to the increase of refractive index value corresponding to mathematical transfer function analysis results in section 3.3.3. For width of well, the parameter variation is not significant.

- The variation of microring radius sizes

The increase of ring radius size is directly proportional to the increase of depth of well and velocity, while width of well and FSR and width of well are proportional to the increase of ring radius which is consistent with the mathematical analysis in section 3.3.2.

- The variation of input center wavelength signal

Width of well and FSR are direct proportional to the change of center wavelength of the input signal. The increase of center wavelength has a direct effect on the increase of width of well and FSR, while depth of well and velocity are insignificant.

Table 4.17 The comparison of primary suitable parameter specifications

Feature	Type of Modulator		
	RADM	CADM	MCADM
Peak Power (a.u)	1	1	1
Center Ring Radius (μm)	20	20	20
Left Ring Radius (μm)	-	-	10
Right Ring Radius (μm)	-	-	10
Center Wavelength (μm)	1.55	1.55	1.55
Depth of Well (dB)	1.24	1.30	1.56

Table 4.17 (Cont.)

Feature	Type of Modulator		
	RADM	CADM	MCADM
Width of Well (nm)	1	2	2
Net Force (N)	$\approx 18.40 \times 10^{-12}$	$\approx 18.40 \times 10^{-12}$	$\approx 18.48 \times 10^{-12}$
Velocity ($\mu\text{m/s}$)	4.973	4.958	6.809
Capacity	17	17	28

4.3.3 Performance Comparison of Proposed and the Other System

From the constraint of problem is 2 nm of polystyrene and trapped with velocity 8 $\mu\text{m/s}$. Therefore, 3 modulator systems are simulated and compared in the same environment. The intensity coupling coefficient, material, ring radius size and center wavelength of input signals are fixed. The properties of tweezer signal are compared in the Figure 4.56 and the performances of 3 modulators are compared in Table 4.18. Figure 4.56 indicates that the optical tweezer properties of the proposed system are superior to the other modulation techniques.

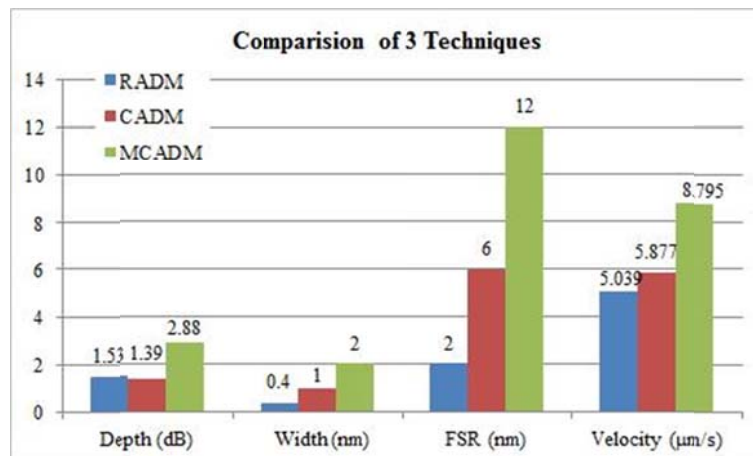


Figure 4.56 The compared parameters variations of 3 modulators

Table 4.18 The comparison of three modulators performance

Feature	Type of Modulator		
	RADM	CADM	MCADM
Peak Power (a.u)	1	1	1
Center Ring Radius (μm)	20	20	20
Left Ring Radius (μm)	-	-	10
Right Ring Radius (μm)	-	-	10
Center Wavelength (μm)	1.55	1.55	1.55
Depth of Well (dB)	1.53	1.39	2.88
Width of Well (nm)	0.4	1	2
FSR(nm)	2	6	12
Net Force (N)	$\approx 18.40 \times 10^{-12}$	$\approx 18.40 \times 10^{-12}$	$\approx 18.51 \times 10^{-12}$
Velocity ($\mu\text{m}/\text{s}$)	5.039	5.877	8.975
Capacity	17	17	28

4.4 Opti FDTD Simulation Results

After the output results have been tested and analyzed using Matlab, the output results are tested by Opti-FDTD. Three microring devices are modeled under the constraint of suitable parameters, and the Gaussian input is fed into each system to evaluate them. In addition, the output results of two commercial programs are evaluated utilizing Pearson product-moment correlation coefficient or "Pearson's correlation coefficient", commonly called "the correlation coefficient (r)". It is obtained by dividing the covariance of the two variables by the product of their standard deviations [58].

$$r = \frac{\sum(x_i - \bar{x})(y_i - \bar{y})}{\sqrt{\sum(x_i - \bar{x})^2 \sum(y_i - \bar{y})^2}} \quad (4.1)$$

4.4.1 Racetrack Add-Drop Modulator Simulation

Figures 4.57-4.58 and 4.60 show the model and output results of RADM, while the Figure 4.59 shows the comparison of Matlab simulation results. The correlation coefficient between Matlab and Opti-FDTD results is 0.910.

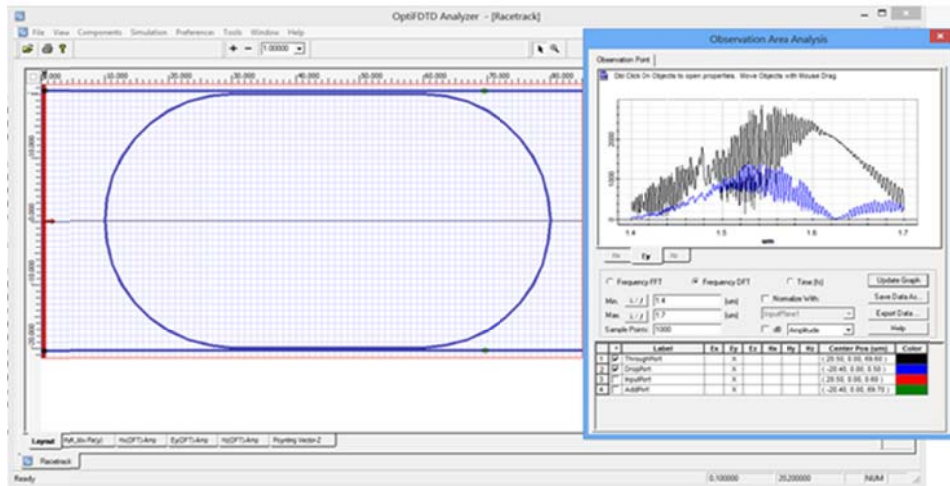


Figure 4.57 The Racetrack Add-Drop Modulator model

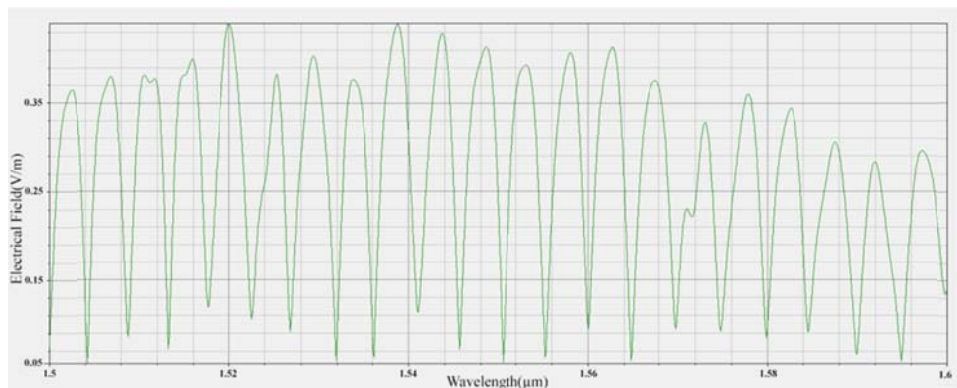


Figure 4.58 The output of electrical field at throughput port

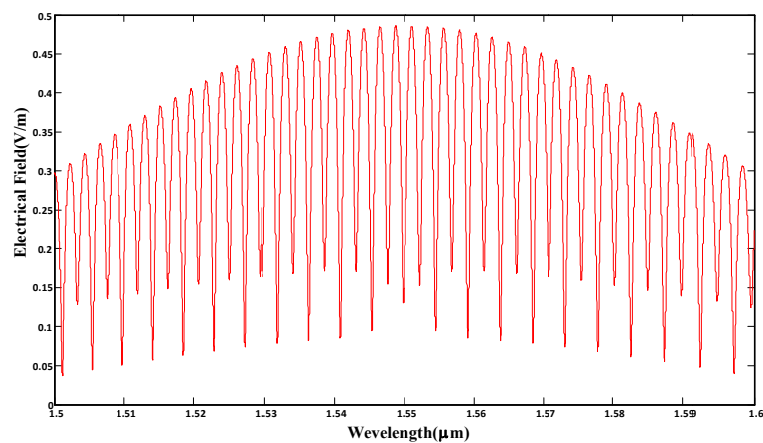


Figure 4.59 The output of electrical field at throughput port using Matlab

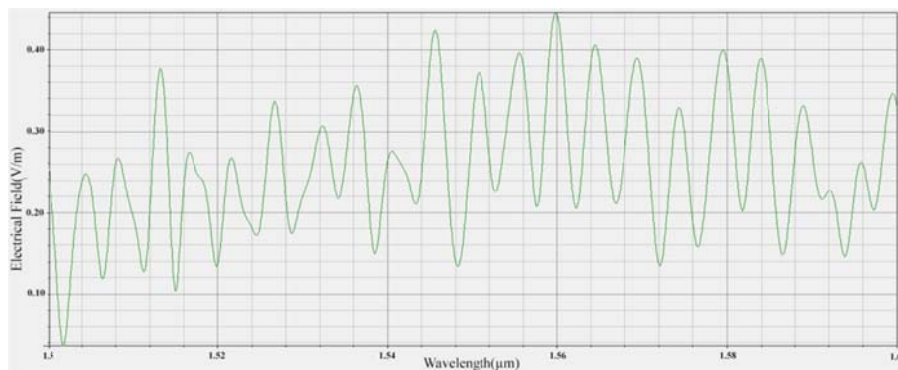


Figure 4.60 The output of electrical field at drop port

When comparing the electrical field from Opti-FDTD in Figure 4.58 and Matlab in Figure 4.59, it is found that the electrical field of Opti FDTD at the throughput port is different from Matlab. Due to power loss in long distance, it is possible that RADM could occur because of the long coupling distance of $30\ \mu\text{m}$. The physical of output signal shapes are similar. However, the amplitude changes are different.

4.4.2 Circular Add-Drop Modulator Simulation

Figures 4.61-4.62 and 4.64 show the model and output results of CADM, while figure 4.63 shows the output of electrical field at the throughput port compared with the output signal of Opti-FDTD in Figure 4.62. The correlation coefficient between Matlab and Opti-FDTD results is 0.803.

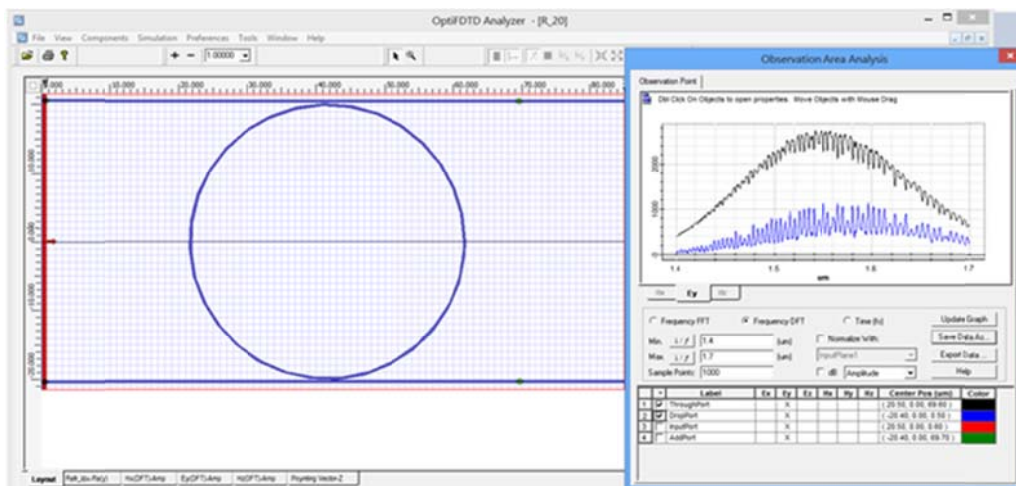


Figure 4.61 The Circular Add-Drop Modulator model

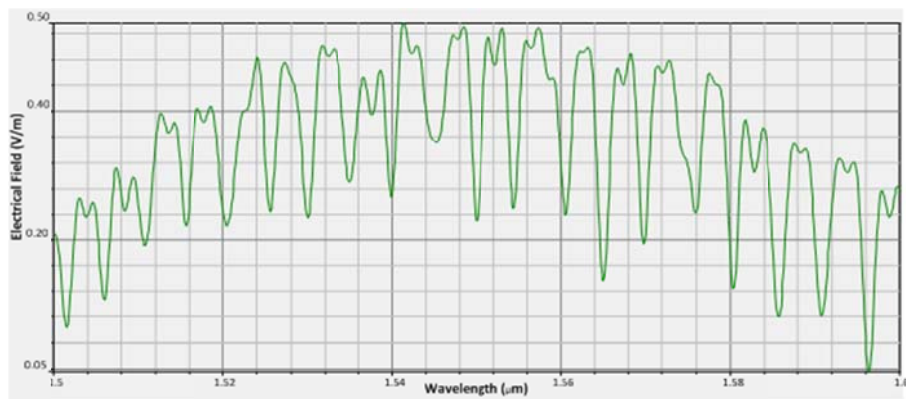


Figure 4.62 The output of electrical field at throughput port

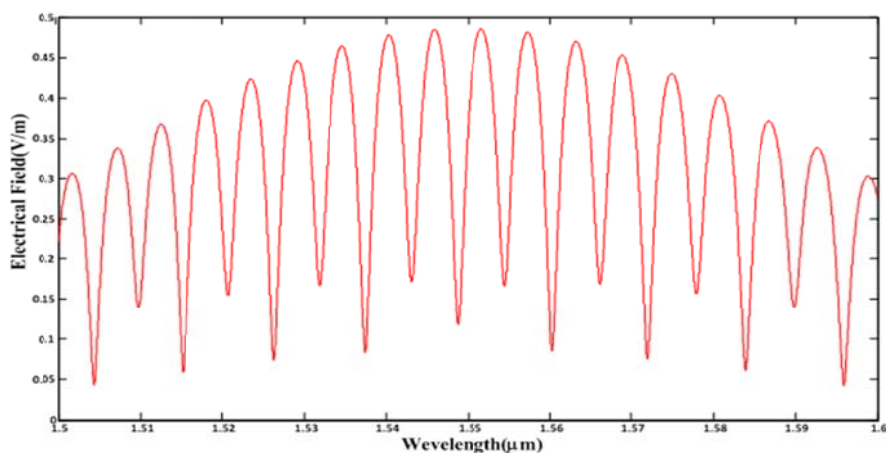


Figure 4.63 The output of electrical field at throughput port from Matlab

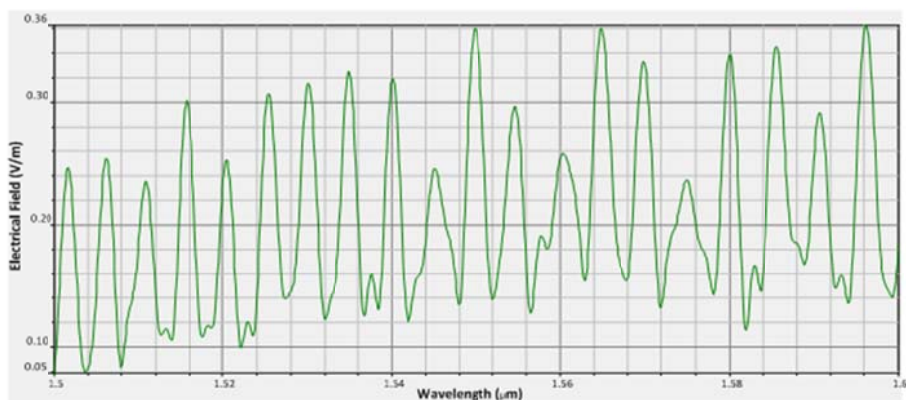


Figure 4.64 The output of electrical field at drop port

When comparing the electrical fields from Opti-FDTD and Matlab in Figures 4.62 and 4.63, it is found that the Opti-FDTD results can confirm the possibility of Matlab results. When considering the physical of output signal shape, it is found that the Opti FDTD results produce the same shape. However, distortions occur at the peak of output signal which originates from loss and noise.

4.4.3 Modified Circular Add-Drop Modulation Simulation

Figures 4.65-4.66 and 4.68 show the model and output results of MCADM results, while the Figure 4.67 shows the Matlab simulation results for comparison. The correlation coefficient between Matlab and Opti FDTD results is 0.832.

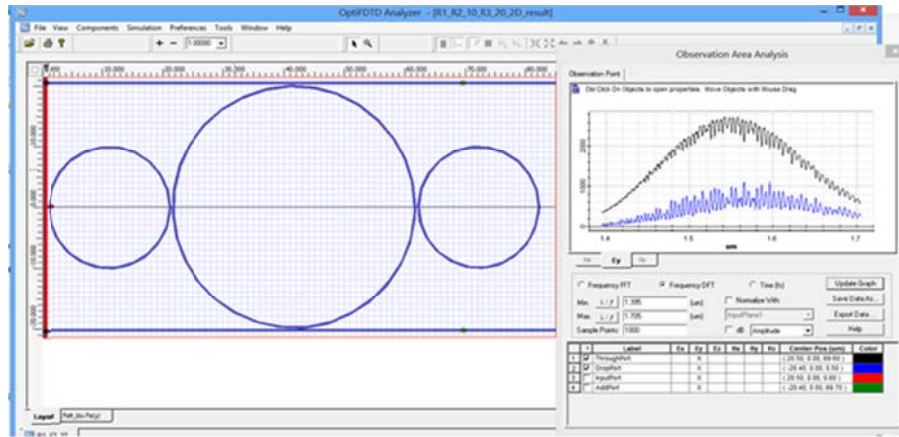


Figure 4.65 The Modified Circular Add-Drop Modulator model

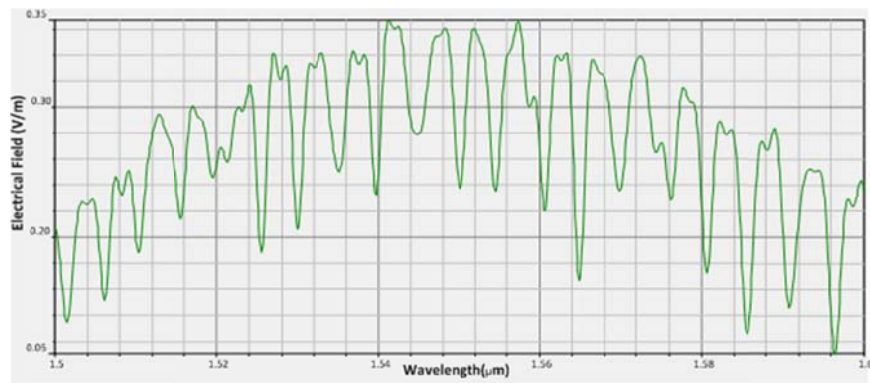


Figure 4.66 The output of electrical field at throughput port

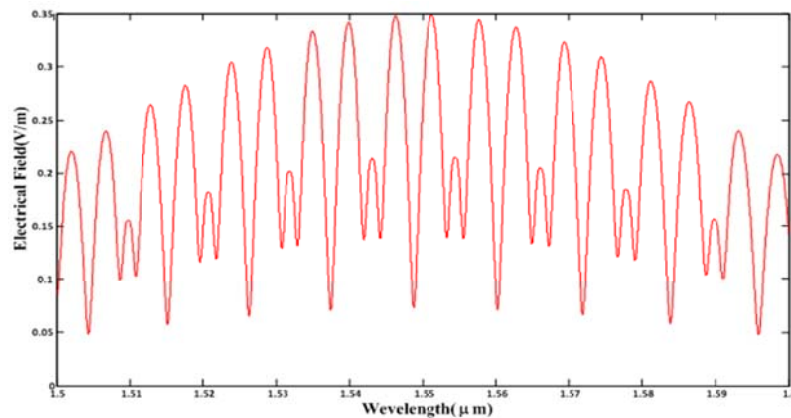


Figure 4.67 The output of electrical field at throughput port from Matlab

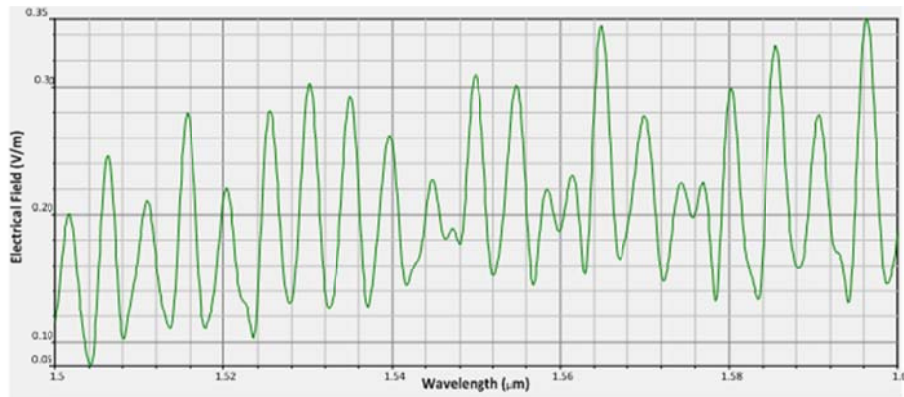


Figure 4.68 The output of electrical field at drop port

In case of Modified Circular Add-Drop Modulator, when comparing the electrical field from Opti-FDTD and Matlab in Figures 4.66 and 4.67, it is found that the Opti FDTD result can confirm the possibility of Matlab results. When considering the physical of output field shape, it is found that the Opti-FDTD result produce the same shape. However, distortions occur at the peaks of output field which originate from loss and noise. When comparing the results between CADM and MCADM, it is found that the peaks of the electrical field of MCADM is disturbed less than CADM.

4.5 Summary of the Published Works [61, 62] and Thire Contribution to This Thesis

The first published research [61] proposes the optical tweezer and generator using MCADM for nano-biological molecules such as tangle protein (tau tangles and β -amyloid plaques). Tangle protein and molecular motor can transport and connect to the required destination over bus network and it can be used for Alzheimer' s disease diagnosis. The basis of the tweezer generator device is based on MCADM and applied in this thesis. In addition, the force theory concerning tweezer properties is based on the same theoretical concept. The second published research [62] proposes a possible application which uses the proposed optical tweezer utilizing MCADM for the drug delivery network. Moreover, this research presents the reliability and stability of the drug delivery network in terms of insertion loss (IL) and crosstalk effects (FC). Normally, the ratio of the intensity coupling coefficient must be greater than the add port for high gradient force trapping. The parameters of the two previous studies are consistent. The intensity coupling coefficient has effects on the depth of well (gradient force). Therefore, the intensity coupling coefficient (κ_1) between the input and the throughput port is 0.5, the intensity coupling coefficients between center add-drop or center microring, and left or right microring (κ_2, κ_4) are 0.35. The intensity coupling coefficient (κ_3) between add and drop ports is 0.1, and

the size of center ring radius (R_{ad}) is equal to 20 μm . The left and right ring radii (R_R or R_L) are varied and the material used is InGaAsP. Finally, the input center wavelength (λ_0) is varied in the optical transmission window. The waveguide fabricated from InGaAsP for core and cladding is InP. The third publication [63] is the extended work from the previous publication [62] which uses the same parameters. However, the left and right ring radius (R_R or R_L) is fixed at 5 μm . The study compares bus, star and ring networks based on crosstalk and signal to noise ratio.

4.6 Summary

The characteristics of the trapping tools for an optical Racetrack Add-Drop Ring Resonator, optical Circular Add-Drop Modulator and optical Modified Circular Add-Drop Modulator are proposed and confirmed in this thesis. The Gaussian and Dark Soliton are input into the ring resonator devices. Five parameters consisting of intensity coupling coefficient, materials, ring radius, wavelength and velocity are examined for the proper trapping and manipulation characteristics. The parameters affecting the width of well are ring radius size and input center wavelength. The lower bound and upper bound of ring radii used in this thesis are in the range of 4-20 μm for center microring radius and 2-10 μm for left and right microring radius. The parameters affecting velocity are the intensity coupling coefficient ranging from 0-1, the refractive index depending on material type and ring radius size. In the next chapter, the conclusion and future work are proposed.

Chapter 5

Conclusion and Future Work

In this chapter, the best parameters from simulation results of an Optical Racetrack Add-Drop Modulator, Optical Circular Add-Drop Modulator and Optical Modified Add-Drop Modulator are chosen for determining trapping tool characteristics. The Gaussian and Dark Soliton signals are input into ring resonators. The output signals, the depth of well, the width of well, the trapping tool capacity and the velocity are compared. The chapter is divided into two sections. The first section proposes the optimized parameters for the proposed microring modulators and conclusion. The second section provides recommendations for future research.

5.1 Conclusion

This thesis proposes the design of tweezer and generators using Modified Circular Add-Drop Modulator. There are 6 steps in the design of tweezer generators. First, the explicit constrained problem such as the size of the particle, center wavelength of input signals and required velocity of particle trapping is given. The second step deals with the mathematical transfer function of the device which is used to explain the characteristics or properties of tweezer signal. The third step concern the analytical study of mathematical transfer function affecting the desirable tweezer properties output. Based on the primary knowledge of analytical study of mathematical transfer function, all parameters affecting optical tweezer properties are tested and chosen as suitable parameters for the desirable output in the fourth step. The next step is using those suitable parameters for designing a device and the final step is to simulate or fabricate a device to confirm the optical tweezer properties. Based on the constrained problem stated in Chapter 3, 2 nm polystyrene particle is trapped and manipulated with $\approx 8 \mu\text{m/s}$ velocity. The center wavelength of input signal for particle trapping is 1550 nm. The force theory supports and describes the originated net force in Rayleigh regime ($X \ll 1$). After that, the mathematical transfer functions for explaining the tweezer signal is analyzed and tested. The results are used as a guideline of choosing proper device parameters. At that time, the primary suitable parameter specification is simulated and tested for variation upon nonlinear properties of MCADM device. Then suitable parameters are chosen based on the constrained problem and design. The intensity coupling coefficient (κ_1) between the input and the throughput ports is 0.9, the intensity coupling coefficient between the center add-drop or center microring and the left or the right microring (κ_2, κ_4) are 0.35, the intensity coupling coefficient (κ_3) between

add and drop ports is 0.1, the size of center ring radius (R_c or R_d) is assigned by radius of 20 μm , the left and right ring radii (R_R or R_L) are 10 μm , the material suitable for our requirement is InGaAsP. Finally, the input center wavelength (λ_0) is 1550 nm. The waveguide fabricated from InGaAsP for core and cladding is InP. The width and height of the waveguide are 0.7 μm and the length of bus waveguide from input port to the MCADM ring is 5 μm . Afterward, the simulation of the proposed design is conducted and the results are confirmed. The experimental results show that the optical tweezer signal is generated by MCADM with the 2 nm width of well, 2.88 dB depth of well, and 18.51 pN of the net force. The carrying capacity is 28 and velocity is 8.795 $\mu\text{m/s}$. The proposed design of tweezer and generators using MCADM can be applied for targeted drug delivery system and cancerous therapeutic uses.

5.2 Future Work

Since the OptiFDTD program used in this study does not have Bright and Dark Soliton input modules, the results can be validated only the Gaussian input signal for three modulators. For future research, the author will determine the methodology to confirm the results of the modulation signal obtained from Gaussian and Dark Soliton within the modulators. In addition, the microparticles or molecular trapping processes for transportation and manipulation is an attractive investigation.

REFERENCES

- [1] A. Ashkin and J. M. Dziedzic, "Optical trapping and manipulation of viruses and bacteria," *Science*, Vol. 235, No. 4795, pp. 1517-1520, 1987.
- [2] E. Qu, H. Guo, C. Xu, C.Liu, Z. Li, B. Cheng, and D. Zhang, "Method used to measure interaction of proteins with dual-beam optical tweezers," *Journal of Biomedical Optics*, Vol. 11, No. 6, 2016.
- [3] N. P. Praetorius, and T.K. Mandal, "Engineered nanoparticles in cancer therapy," *Recent Patents on Drug Delivery & Formulation*, Vol. 2007, No. 1, pp. 37-51, 2007.
- [4] M. Raoof, and S. A. Curley, "Non-Invasive Radiofrequency-Induced Targeted Hyperthermia for the Treatment of Hepatocellular Carcinoma," *International Journal of Hepatology*, Vol. 2011, 2011.
- [5] S. M. Block, D. F. Blair, and H. C. Berg, "Compliance of Bacterial Flagella Measured with Optical Tweezers," *Nature*, Vol. 338, No. 6215, pp. 514-518, 1989.
- [6] J. T. Finer, R. M. Simmons, and J. A. Spudich, "Single myosin molecule mechanics: piconewton forces and nanometre steps," *Nature*, Vol. 368, No. 6467, pp. 113-119, 1994.
- [7] M. D. Wang, H. Yin, R. Landick, J. Gelles, and S. M. Block, "Stretching DNA with optical tweezers," *Biophysical Journal*, Vol. 72, No. 3, pp. 1335-1346, 1997.
- [8] I. Titushkin, and M. Cho, "Distinct Membrane Mechanical Properties of Human Mesenchymal Stem Cells Determined Using Laser Optical Tweezers," *Biophysical Journal*, Vol. 90, No. 7, pp. 2582-2591, 2006.
- [9] H. Liang, W. H. Wright, S. Cheng, W. He, and M. W. Berns, "Micromanipulation of Chromosomes in PTK2 Cells Using Laser Microsurgery (Optical Scalpel) in Combination with Laser-Induced Optical Force (Optical Tweezers)," *Experimental Cell Research*, Vol. 204, No. 1, pp. 110-120, 1993.
- [10] D. G. Grier, "A revolution in optical manipulation," *Nature*, Vol. 424, No. 6950, pp. 810-816, 2013.
- [11] A. Clement-sengewald, K. Schütze, A. Ashkin, G. A. Palma, G. Kerlen, and G. Brem, "Fertilization of bovine oocytes induced solely with combined laser microbeam and optical tweezers," *Journal of Assisted Reproduction and Genetics*, Vol. 13, No. 3, pp. 259-265, 1996.
- [12] H. Zhang, and K.-K. Liu, "Optical tweezers for single cells," *Journal of the Royal Society Interface*, Vol. 2008, No. 5, pp. 671-690, 2008.
- [13] S. Lin, E. Schonbrun, and K. Crozier, "Optical Manipulation with Planar Silicon Microring Resonators," *Nano Lett.*, Vol.10, No.7, pp. 2408-2411, 2010.

- [14] D. G. Rabus, 2002, "Realization of Optical Filters using Ring Resonators with integrated Semiconductor Optical Amplifiers in GaInAsP/InP." D. Eng. dissertation, Technischen Universitat Berlin, Germany.
- [15] H. Cai, and A. W. Poon, "Optical manipulation and transport of microparticles on silicon nitride microring-resonator-based add-drop devices," *Optics Letters*, Vol. 35, No. 17, pp. 2855-2857, Sept. 2010.
- [16] N. Suwanpayak, M. A. Jalil, C. Teeka, J. Ali, and P. P. Yupapin, "Optical vortices generated by a PANDA ring resonator for drug trapping and delivery applications," *Biomed. Opt. Express*, Vol 2, No. 1, pp. 159–168, Jan. 2011.
- [17] K. Svoboda and S. M. Block, "Biological applications of optical forces," *Annual Review of Biophysics and Biomolecular Structure*, Vol. 23, No. 1, pp. 247-285, 1994.
- [18] A. J. Michaels and C. Lau, "Performance of Percent Gaussian Orthogonal Signaling Waveforms," *Military Communications Conference (MILCOM), 2014 IEEE* , Vol -, No. -, pp. 338-343, 2014.
- [19] Montes c., Picozzi a., and Haelternam M., "Optical Solitons: Theoretical Challenges and industrial Perspectives-Lecture 16,Les Houches Workshop", v. e. Zakharow and S. wabnits ods., *EDP Springer*, 283-292, 1999.
- [20] A. Hasegawa and F. Tappert, "Transmission of stationary nonlinear optical pulses in dispersive dielectric fibers. I. Anomalous dispersion," *Appl. Phys. Lett*, Vol. 23, No. 142, 1973.
- [21] L. F. Mollenauer, R. H. Stolen, and J. P. Gordon, "Experimental observation of picosecond pulse narrowing and solitons in optical fibers," *Phys. Rev. Lett*, Vol. 45, No. 13, pp. 1095 1980.
- [22] L. F. Mollenauer, R. H. Stolen, and J. P. Gordon, "Experimental observation of picosecond pulse narrowing and solitons in optical fibers," *Phys. Rev. Lett*, Vol. 45, No. 13, pp. 1095 1980.
- [23] N. Kikuchi, K. Sekine, and S. Sasaki, "Analysis of XPM effect on WDM transmission performance," *Electronics Letters.*, Vol. 33, No. 8, pp. 653–654, 1997.
- [24] G. P. Agrawal, 2001, *Nonlinear Fiber Optics Third Edition*, San Diego: Academic Press.
- [25] K. Amarnath, 2006, "Active Microring and Microdisk Optical Resonators on Indium Phosphide." Ph.D.dissertation, University of Maryland.
- [26] C. Asplund, 2003, "Epitaxy of GaAs-based long-wavelength vertical cavity lasers." Ph.D.dissertation, Royal Institute of Technology, Kista, Sweden.
- [27] S. Imscher, 2003, "Design, Fabrication and Analysis of InP-InGaAsP Traveling-Wave Electro-Absorption Modulators." Ph.D.dissertation, Royal Institute of Technology, Kista, Sweden.

- [28] K. Dolgaleva, W. Chau Ng, L. Qian, and J. S. Aitchison, "Compact highly-nonlinear AlGaAs waveguides for efficient wavelength conversion," *Optics Express*, Vol. 19, No. 13, pp. 12440 – 12455, 2011.
- [29] C. Y. Tai, J. S. Wilkinson, N. M. B. Perney, M. C. Netti, F. Cattaneo, C. E. Finlayson, and J. J. Baumberg, "Determination of nonlinear refractive index in a Ta₂O₅ rib waveguide using self-phase modulation," *Optics Express*, Vol. 12, No. 21, pp. 5110– 5116, 2004.
- [30] K. Ikeda, R. E. Saperstein, N. Alic and Y. Fainman, "Thermal and Kerr nonlinear properties of plasma-deposited silicon nitride/ silicon dioxide waveguides," *Optics Express*, Vol. 16, No. 17, pp. 12987-12994, 2008.
- [31] S. C. Mao, S. H. Tao, Y. L. Xu, X. W. Sun, M. B. Yu, G. Q. Lo, and D. L. Kwong, "Low propagation loss SiN optical waveguide prepared by optimal low-hydrogen module," *Optics Express*, Vol. 16, No. 25, pp. 20809-20816, 2008.
- [32] G. Li, T. Maruyama, and K. Iiyama, "Low-propagation-loss Ta₂O₅ optical waveguides on silica substrate," *Japanese Journal of Applied Physics* 53, 04EG12, 2014.
- [33] V. Van, T. A. Ibrahim, P. P. Absil, F.G.Johnson, R. Grover, and P.-T. Ho, "Optical signal processing using nonlinear semi-conductor microring resonators," *Journal of Selected Topics in Quantum Electronics*, Vol. 8, No. 3, pp. 705-713, 2002.
- [34] Z. Bian, B. Liu, and A. Shakouri, "InP-Based Passive Ring-Resonator-Coupled Lasers," *IEEE Journal of Quantum Electronics*, Vol. 39, No. 7, pp. 859-865, 2003.
- [35] T. Barwicz, M. A. Popović , P. T. Rakich, M. R. Watts, H. A. Haus, E. P. Ippen, and Henry I. Smith, "Microring-resonator-based add-drop filters in SiN: fabrication and analysis," *Optics Express*, Vol. 12, No. 7, pp. 1437-1442, 2004.
- [36] Y. Kokuban, "Vertically Coupled Microring Resonator Filter for Integrated Add/Drop Node," *IEICE Transactions on Electronics*, Vol. E88-C, No. 5, pp. 1458-1464, 2005.
- [37] T. Barwicz, M. A. Popović , P. T. Rakich, M. R. Watts, H. A. Haus, E. P. Ippen, and Henry I. Smith, "Fabrication of Add-Drop Filters Based on Frequency-Matched Microring Resonators," *Journal of Lightwave Technology*, Vol. 24, No. 5, pp. 2207-2214, 2006.
- [38] A. Yalçın, K. C. Popat, J. C. Aldridge, T. A. Desai, J. Hryniewicz, N. Chbouki, B. E. Little, O. King, V. Van, S. Chu, D. Gill, M. Anthes-Washburn, and B. B. Goldberg, "Optical sensing of biomolecules using microring resonators," *IEEE Journal of Quantum Electronics*, Vol. 12, No. 1, pp. 148-155, 2006.
- [39] Q. Xu, D. Fattal, and R. G. Beausoleil, "Silicon microring resonators with 1.5 μm radius," *Optics Express*, Vol. 16, No. 6, pp. 4309-4315, 2008.

- [40] X. Xi, L. Yun-Tao, Y. Yu-De, Y. Jin-Zhong, "Silicon-Based Asymmetric Add-Drop Microring Resonators with Ultra-Large Through-Port Extinctions," *Chinese Physics Letters*, Vol.27, No. 5, pp. 054208, 2010.
- [41] W. Bogaerts, P. D. Heyn, T. V. Vaerenbergh, K. D. Vos, S. K. Selvaraja, T. Claes, P. Dumon, P. Bienstman, D. V. Thourhout, and R. Baets, "SOI Microring fabrication," *Laser Photonics Review*, Vol. 6, No. 1, pp. 47-73, 2012.
- [42] P. Rabiei, J. Ma, S. Khan, J. Chiles, and S. Fathpour, "Submicron optical waveguides and microring resonators fabricated by selective oxidation of tantalum," *Optics Express*, Vol. 21, No. 6, pp. 6967-6972, 2013.
- [43] N. Suwanpayak, M. A. Jalil, M. S. Aziz, J. Ali and P. P. Yupapin, "Molecular buffer using a PANDA ring resonator for drug delivery use," *International Journal of Nanomedicine*, Vol. 2011, No. 6, pp. 575-580, 2011.
- [44] S. Punthawanunta, S. Songmuanga, S. Mitathab, P.P. Yupapin, "Dynamic Optical Tweezers Generation using a PANDA Ring Resonator," *Procedia Engineering*, Vol. 8, pp. 467-473, 2010.
- [45] M. Tasakorn, C. Teeka, R. Jomtarak, P. P. Yupapin, "Multitweezer Generation Control with a Nanoring Resonator System," *Fiber Optics and Optical Communication*, Vol. 49, No. 7, pp. 075002, 2010.
- [46] A. Nikoukar, I. S. Amiri and J. Ali, "Generation of Nanometer Optical Tweezers Used for Optical Communication Networks," *International Journal of Innovative Research in Computer and Communication Engineering*, Vol. 1, No. 1, pp. 77-85.
- [47] N. Thammawongsa, S. Tunsiri, M. A. Jalil, J. Ali and P. P. Yupapin, "6. Storing and Harvesting Atom/Molecule On-Chip: Challenges and Application," *Biosensors & Bioelectronics*, Vol. 3, No.5, 2012.
- [48] S. Glomglomea, I. Srithanachaib, C. Teekac, S. Mitathaa, S. Niemcharoenb and P. P. Yupapin, "Optical Spin Generated by a Soliton Pulse in an Add-Drop Filter for Optoelectric and Spintronic Use," *Optics & Laser Technology*, Vol. 44, No. 5, 1294-1297, 2012.
- [49] T. Saktioto, D. Irawan, N. Thammawongsa and P. P. Yupapin, "Drug Delivery System Model using Optical Tweezer Spin Control," *Biosensors & Bioelectronics*, Vol. 5, No.3, 2014.
- [50] M. Endo, "Numerical simulation of an optical resonator for generation of a doughnut-like laser beam," *Optics Express*, Vol. 12, No. 9, pp. 1959-1965, 2004.
- [51] P. P. Yupapin, K. Kulsirirat and W. Techithdeera, "Optical capsule and tweezer array for molecular motor use," *IEEE Transactions on Nanobioscience*, Vol. 12, No. 3, pp. 222-227, 2013.

- [52] N. Thammawongsa, F.D. Zainol, S. Mitatha, J. Ali and P. P.Yupapin, "Nanorobot Controlled by Optical Tweezer Spin for Microsurgical Use," IEEE Transactions on Nanotechnology, Vol. 12, No. 1, pp. 29-34, 2012.
- [53] P. P. Yupapin and B. Vanishkorn, "Mathematical simulation of light pulse propagating within a microring resonator system and applications," Applied Mathematical Modelling, Vol. 35, No. 4, pp. 1729-1738, 2011.
- [54] N. Suwanpayak, M. A. Jalil, C. Teeka, J. Ali and P. P. Yupapin, "Optical vortices generated by a PANDA ring resonator for drug trapping and delivery applications," Biomedical Optics Express, Vol. 2, No. 1, pp. 159-168, 2011.
- [55] M. A. Jalila, B. Piyatamrong, S. Mitathab, J. Alia, P. P. Yupapin, "Molecular transporter generation for quantum-molecular transmission via an optical transmission line," Nano Communication Networks, Vol. 1, No. 2, pp. 96-101, 2010.
- [56] N. Pornsuwancharoena, M. Tasakornb, S. Julajaturasiraratha, K. Chaiyawonga and P.P. Yupapin, "Multi-variable quantum tweezers generation using photon entanglement," Nano Communication Networks, Vol. 1, No. 2, pp. 131-137, 2010.
- [57] P. Youplao, S. Mitatha and P. P. Yupapin, "Novel Multi Optical Trapping Tool Generation within Add/Drop Filter System Controlled by Light," Procedia Engineering, Vol. 8, No. -, pp. 237-242, 2011.
- [58] N. Suwanpayaka and P. P. Yupapina, "Drug Trapping and Delivery Using a PANDA Ring resonator," Procedia Engineering, Vol. 8, No. -, pp. 252-260, 2011.
- [59] Y. Kokuban, "Vertically Coupled Microring Resonator Filter for Integrated Add/Drop Node", IEICE Transactions on Electronics, Vol. E88-C, No. 3, pp.349-362, 2005.
- [60] J. Zhang, J. Yu, J. Tang, M. Xie, F. Li, F. Huang and Z. Chen, "The correlation coefficient method for alignment of polarization maintaining fiber," International Conference on Numerical Simulation of Optoelectronic Devices (NUSOD), Vol. -, No. -, pp. 53-54, 2013.
- [61] S. Mitatha, N. Moongfangklang, M. A. Jalil, N. Suwanpayak, T. Saktioto, J. Ali, and P. P. Yupapin, "Proposal for Alzheimer's diagnosis using molecular bus network," International Journal of Nanomedicine, Vol. 2011, No. 6, pp. 1209-1216, 2011.
- [62] S. Mitatha, N. Moongfangklang, M. A. Jalil, N. Suwanpayak, J. Ali, and P. P. Yupapin, "Multi-access drug delivery network and stability," International Journal of Nanomedicine, Vol. 2011, No. 6, pp. 1757-1764, 2011.
- [63] N. Moongfangklang, M. A. Jalil, K. Innate, S. Mitatha, J. Ali, and P. P. Yupapin, "Molecular network topology and reliability for multipurpose diagnosis," , Int J Nanomedicine, Vol. 6, 2011, pp. 2385-2392, ISI Impact factor 2011 (4.976).

APPENDIX
LIST OF PUBLICATIONS

1. S. Mitatha, N. Moongfangklang, M. A. Jalil, N. Suwanpayak, T. Saktioto, J. Ali, and PP Yupapin, "Proposal for Alzheimer's diagnosis using molecular buffer and bus network," *Int J Nanomedicine*, Vol. 6, 2011, pp. 1209–1216, ISI Impact factor 2011 (4.976).
2. S. Mitatha, N. Moongfangklang, M. A. Jalil, N. Suwanpayak, J. Ali, and P. P. Yupapin, "Multi-access drug delivery network and stability," *Int J Nanomedicine*, Vol. 6, 2011, pp. 1757–1764, ISI Impact factor 2011 (4.976).
3. N. Moongfangklang, M. A. Jalil, K Innate, S. Mitatha, J. Ali, and P. P. Yupapin, "Molecular network topology and reliability for multipurpose diagnosis," , " *Int J Nanomedicine*, Vol. 6, 2011, pp. 2385–2392, ISI Impact factor 2011 (4.976).
4. N. Thammawongsa, N. Moongfangklang, S. Mitatha, and P. P. Yupapin, "Novel nano-antenna system design using photonic spin in a panda ring resonator," *Progress In Electromagnetics Research Letters*, Vol. 31, pp. 75-87, ISI Impact factor 2012 (NA).

BIOGRAPHY

Name: Mr. Narongchai Moongfangklang
Date of Birth: 25 September 1974
Born: Nakhon ratchasima, Thailand
Current Address: 19 Moo 2 Phayao University, Tambon Maeka, Amphur Muang, Phayao, Thailand, 56000.
Email: nanfa_blue@yahoo.com, narongchai.mo@up.ac.th
Education:

- Bachelor's degree in telecommunication engineering, Suranaree University of Technology, Nakhon ratchasima, Thailand, in 1998.
- Master's degree in computer engineering, King Mongkut's Institute of Technology Ladkrabang, Thailand, in 2004.

Skilled Works:

- Data Communication
- Genetic Algorithm
- Nonlinear Optics
- Optical Tweezers, Optical Trapping and Manipulation